

THIN FILM MATERIALS THROUGH THE INTERFACIAL ASSEMBLY OF
INORGANIC NETWORKS

By

JEFFREY THOMAS CULP

A DISSERTATION PRESENTED TO THE GRADUATE SCHOOL
OF THE UNIVERSITY OF FLORIDA IN PARTIAL FULFILLMENT
OF THE REQUIREMENTS FOR THE DEGREE OF
DOCTOR OF PHILOSOPHY

UNIVERSITY OF FLORIDA

2002

For Garrett

ACKNOWLEDGMENTS

It has been said that no man is an island unto himself, and nowhere is this truer than in the scientific community. Experiments are proposed, results are discussed, conclusions are debated, and out of skepticism, truths are extracted and new ideas are born. Indeed, the life's blood of science is collaboration and I have benefited greatly from the countless discussions with fellow colleagues throughout the course of this work. First and foremost, I would like to thank Professor Mark Meisel and Ju-Hyun Park in the Physics Department at the University of Florida for performing all of the magnetics measurements presented in this dissertation. Equally as beneficial were the many discussions the data provoked. I thank you both for your hard work, your knowledge that you shared with me, and above all for providing a working relationship that was just as rewarding personally as it was professionally.

The data collected at the Advanced Photon Source (APS) were essential to the work described in this dissertation and I would like to acknowledge all those who assisted in the experiments. I would like to thank Professor Randy Duran for getting the University of Florida involved in the Materials Research Collaborative Access Team (MRCAT) at the APS and for our fruitful discussions. The beamline support staff at the MRCAT were a valuable asset and I would like to especially thank Nadia Leyorovska, Holger Tostmann, and William Lavender for their assistance. I also thank Professor Pulak Dutta and his group at Northwestern University for their aid in getting our Langmuir diffraction experiments off the drawing board. To my fellow researchers from

the Duran group at UF, I want to say thanks for making the long hours and hard work bearable with your assistance and your wit. Lastly, I want to thank Guyanga Weerasekera and Dr. Mark Davidson who were my left and right hands at the beamline. I do not know how I could have done it without them.

My day-to-day research was made all the more enjoyable by my friends and co-workers in the Talham group. I would especially like to thank Gail for taking me under her wing in my first year and assisting me with the metal phosphonate project. I really enjoyed our golf outings as well and hope we can hit the links again sometime. Thanks go to Missy for her professional guidance and personal friendship. She was always there when my reactions failed, my personal life met a crisis, or when I just needed a trip to the Salty Dog to regroup. May our paths cross again. I thank Isa for all of her help with the AFM, SEM, and BAM experiments. To all the rest, past and present, I am lucky to have had the experience of working with such a professional group and value the personal relationships I made with all of them.

I want to also thank my neighbors in the Boncella group for their advice, their chemicals, and all the laughs we shared. I graciously acknowledge Professor Katherine Williams and Mr. Russell Pierce for their assistance with the AA experiments. Thanks are also due to Professor Eric Lambers at MAIC for his help with the XPS experiments and Karren Kelley at the Electron Microscopy Core Laboratory for her assistance with the SEM experiments. The work performed by everyone in the glass, electronic, and machine shops, the stockroom, and those in the chemistry department staff is also gratefully acknowledged.

The professional influences of my fellow co-workers are interwoven throughout the pages of this dissertation, but perhaps less obvious are the influences of those who have touched me personally, and in doing so, provided the friendship, guidance and inspiration which lead me to where I am today. A special thank you is given to my dear friend Tina Rakes for always being there when I needed her. I thank her for all the times she watched my son when I needed to work, for listening when I needed to talk, for caring, and most of all for being a friend. Her presence will be missed. Thanks also go to my friend Marcia Winter for cheering me up when I was down and for giving me a place to stay while in transition. I may not have made it through this without you. I also want to thank my old buddies Jason Doyle and Kirk Thrasher who were always just a phone call away. True friends indeed stand the test of time.

I also want to express my deepest love and sincerest thanks to my parents for always being there. None of this would have been possible without their selfless devotion, their sacrifices, and their unending support. They taught me the value of hard work and wove the moral fabric of my soul. I am truly lucky to have such wonderful parents. I also say thanks to my brothers Chad and Luke and my sisters Cyndi and Jodi for always being there for me. They are not only my family; they are my friends.

Though the course of this work, I have been influenced by many people either personally or professionally. My advisor, Daniel R. Talham, is one of those rare individuals who has influenced me in both ways. Professionally, Dr. Talham has provided me with exceptional guidance with my research and provided an excellent environment in which to learn. He has given me the direction necessary to achieve the goal at hand, while at the same time the necessary freedom to develop my own ideas,

pursue my own course, and to learn by my own mistakes. I would also like to thank Dan personally for the tremendous support he gave me through a most difficult time in my life. If not for his understanding, his patience, and his inspiration my goals would have fallen out of reach.

The long hours and mental devotion required for a project of this magnitude are perhaps felt most by those closest to you. For her sacrifices, I give Stacy my deepest thanks. The pressures on our relationship were more than anyone could be expected to bear, and I apologize for not telling her often enough how much she was appreciated. Her sacrifices did not go unnoticed. I also want to thank my son Garrett. He is my life, my love, and my inspiration. Through it all, he has been patient beyond his years and I am very proud of him. I can only hope that one day he will look back on this with understanding. Until then, we have a lot of catching up to do.

TABLE OF CONTENTS

	Page
ACKNOWLEDGMENTS	iii
ABSTRACT	x
 CHAPTERS	
1 SUPERMOLECULAR CHEMISTRY AT INTERFACES.....	1
Supermolecular Chemistry.....	1
Assembling Inorganic Networks at Interfaces	4
Thin Film Characterization Techniques	7
Conventional Methods	7
Characterization of Thin Films Using Synchrotron X-ray Radiation	13
Grazing Incidence X-ray Diffraction (GIXD).....	20
X-ray Absorption Fine Structure (XAFS).....	24
2 MIXED-METAL MN-CO PHENYLPHOSPHONATES	
STRUCTURE AND MAGNETIC PROPERTIES	34
Introduction	34
Experimental Section	36
Results and Discussion	38
Sample Preparations.....	38
Magnetic Properties of $Mn(O_3PC_6H_5)_2 \cdot H_2O$ and $Co(O_3PC_6H_5)_2 \cdot H_2O$	42
Search for Spin Glass or Precursor Phases.....	49
Negative Magnetization in the Cobalt-Rich Samples.....	52
Conclusion.....	53
3 STRUCTURE CHARACTERIZATION OF METAL PHOSPHONATE	
LANGMUIR-BLODGETT FILMS BY GRAZING INCIDENT X-RAY	
DIFFRACTION	54
Introduction	54
Experimental Section.....	55
Results and Discussion	56
Manganese Octadecylphosphonate Film.....	56
Azobenzene Derivatized Manganese Phosphonate Film	58
Lanthanum Octadecylphosphonate Film.....	60
Conclusions	63

4	FORMATION OF AN EXTENDED TWO-DIMENSIONAL COORDINATE COVALENT SQUARE GRID NETWORK AT THE AIR WATER INTERFACE	64
	Introduction	64
	Experimental Section	68
	Results	72
	Langmuir Monolayers and LB Film Transfer	72
	Spectroscopic Analyses	75
	XAFS Analysis	77
	X-ray Diffraction and GIXD	79
	Magnetic Properties	80
	Discussion	82
	Choice of System and Monolayer Behavior	82
	Structure of the Network	84
	Magnetism	85
	Mechanism and Structure Directing Elements	87
	Conclusions	88
5	INTERFACIAL ASSEMBLY OF CYANIDE-BRIDGED FE-CO AND FE-MN SQUARE GRID NETWORKS	89
	Introduction	89
	Experimental Section	91
	Results and Discussion	93
	Langmuir Monolayers	93
	Infrared Spectroscopy	94
	Grazing Incidence X-ray Diffraction	96
	Magnetism	97
	Conclusions	100
6	FERROMAGNETISM AND SPIN-GLASS BEHAVIOR IN LANGMUIR-BLODGETT FILMS CONTAINING A TWO- DIMENSIONAL IRON-NICKEL CYANIDE SQUARE GRID NETWORK	101
	Introduction	101
	Experimental	103
	Results	105
	Film Structure	105
	DC Magnetometry	106
	AC Magnetometry	111
	Discussion	115
	Magnetic Anisotropy	115
	Spin Glass Behavior	117
	Conclusions	119
7	SEQUENTIAL ASSEMBLY OF HOMOGENEOUS MAGNETIC PRUSSIAN BLUE FILMS ON TEMPLATED SURFACES	121
	Introduction	121

Experimental	124
Results and Discussion	127
Film Deposition	127
Magnetism	133
Conclusions	137
 8 INVESTIGATIONS INTO THE INTERFACIAL ASSEMBLY OF LINEAR CHAIN AND 2D HEXAGONAL NETWORKS	138
Introduction	138
Experimental	141
Results and Discussion	144
Brewster Angle Microscopy	144
Infrared Spectroscopy	146
Grazing Incidence X-ray Diffraction	149
Magnetism	152
Structures of the Networks	153
Conclusions	156
 LIST OF REFERENCES	158
 BIOGRAPHICAL SKETCH	167

Abstract of Dissertation Presented to the Graduate School
of the University of Florida in Partial Fulfillment of the
Requirements for the Degree of Doctor of Philosophy

THIN FILM MATERIALS THROUGH THE INTERFACIAL ASSEMBLY OF
INORGANIC NETWORKS

By

Jeffrey Thomas Culp

December, 2002

Chair: Daniel R. Talham

Department: Chemistry

Mixed metal phenylphosphonates of composition $\text{Mn}_x\text{Co}_{1-x}(\text{O}_3\text{PC}_6\text{H}_5)_2\text{H}_2\text{O}$ were prepared with $0 < x < 1$. The mixed metal solid solutions are homogeneous and isostructural with the single metal parent compounds. The magnetic phase diagram, down to 2 K, was constructed over the entire composition range. No evidence of spin glass behavior was observed for any concentration at any temperature.

A series of Mn^{2+} and La^{3+} organophosphonate Langmuir-Blodgett films have been structurally characterized by grazing incidence X-ray diffraction using synchrotron radiation. The organophosphonate amphiphiles include both straight alkyl chain and azobenzene groups in the organic tails. The metal oxygen networks within the films are found to be isostructural to related organic/inorganic layered solids.

Reaction of a Langmuir monolayer of an amphiphilic pentacyanoferrate ($3+$) complex with Ni^{2+} , Co^{2+} , and Mn^{2+} ions from the subphase results in the formation of two-dimensional cyanide-bridged network at the air-water interface. The networks can

be transferred to various supports to form monolayer or multilayer lamellar films by the Langmuir-Blodgett (LB) technique. The magnetic properties of these films were investigated as monolayer, bilayer, and multilayer assemblies. The materials possess interesting physical properties such as magnetic anisotropy, magnetic ordering, and spin-glass behavior.

Thin homogenous magnetic films comprised of various Prussian blue analogues have been prepared through the sequential absorption of the appropriate metal ions and hexacyano complexes onto hydrophobic surfaces that were first templated with a Fe-CN-Ni two-dimensional grid network deposited as a Langmuir-Blodgett monolayer. The films show exceptional surface coverage and magnetic behaviors similar to their solid-state analogues with ordering temperature ranging from 5 K to 210 K.

The preparation of low dimensional inorganic networks through the reactions of Langmuir monolayers containing low symmetry amphiphilic metal complexes with aqueous metal cyanides was investigated. The reaction of an amphiphilic iron(III)terpyridine complex with aqueous $\text{Ag}(\text{CN})_2^-$ resulted in the formation of AgCN crystallites at the air-water interface as shown by grazing incidence X-ray diffraction. The reaction of an amphiphilic nickel(II)cyclam complex with aqueous $\text{Ni}(\text{CN})_4^{2-}$ or $\text{Cr}(\text{CN})_6^{3-}$ yielded cyanide-bridged products as evidenced by infrared spectroscopy; however, the structures of the products remain uncertain due to a lack of X-ray diffraction from the materials.

CHAPTER 1 SUPRMOLECULAR CHEMISTRY AT INTERFACES

Supramolecular Chemistry

The intricate complexity of biological systems can humble even the most able of synthetic chemists. Their vast array of structural diversity, from the molecular to the macroscopic level, is both aesthetically pleasing in its symmetry and awe-inspiring in its functional efficiency. Countless eons of trial and error have perfected synthetic processes wherein simple chemical building blocks self-assemble with lock and key precision into complex superstructures such as proteins, enzymes, DNA, and cell membranes. Each of these subsystems then works in tandem in intricate processes to create something so incredibly complex as life. Chemists have long looked to these natural systems for inspiration, hoping to break down and understand the underlying mechanisms of this process called self-assembly, with the hope of one day mastering this same level of synthetic control, where by simply providing the appropriate building blocks, complex structures with specifically tailored physical properties could be achieved. This synthetic paradigm of creating complex chemical systems from relatively simple building blocks has been termed supramolecular chemistry.¹ As a general term, the process includes synthetic techniques such as self-assembly, crystal engineering, and nanoscale chemistry. While having its roots in natural systems, many of the goals in this area of chemistry are focused on developing novel materials with molecular recognition, catalytic, magnetic, electrical, and nonlinear optical properties for use in separations and

nanoscale device applications. As such, it could be said that biological systems provide the inspiration and functional materials provide the motivation.^{2,3}

Supramolecular chemistry as a synthetic approach takes advantage of weak to moderate bonding interactions between complementary molecular components to create a structure that is greater than the sum of its parts. The inter-molecular forces that have traditionally been employed are Van der Waals in nature and include pi-pi stacking, hydrogen bonding, and host-guest interactions.^{1,2} These weaker forces allow for an annealing of the final structure to a thermodynamic rather than kinetic product. To expand the potential applications of supermolecular chemistry, many research groups have investigated transition metal coordination geometries as architectural driving forces.⁴⁻¹³ The coordinate covalent bond has several properties that fit well with the supermolecular synthetic approach. The bond strength is intermediate between the relatively weak Van der Waals interactions and stronger covalent bonds and thereby offers a compromise. The bonding can now be more robust, but labile enough to allow for the self-annealing process that is so advantageous to self-assembled systems. Also, coordination complexes have well characterized, and often predictable, geometries and bonding angles that can aid in predicting *a priori* the structural motif of the final assembly. Supramolecular chemistry can, therefore, be reduced in complexity to a system in which individual linear and angular components combine into one, two, or three-dimensional arrays.^{14,15} Aside from their unique bonding and geometrical properties, transition metals also inherently possess useful physical and chemical properties such as variable oxidation states which can lead to charge transfer

phenomena, colored materials ranging throughout the visible spectrum, cooperative magnetic behavior, and catalytic abilities.

Due to the many advantages offered by transition metal complexes, numerous researchers have developed synthetic strategies incorporating metal ions into various supermolecular arrays. These strategies often involve various combinations of blocking ligands, bridging ligands, and complex geometries. Some of the results to date include "zero-dimensional" clusters,¹⁶⁻²⁵ polygons and polyhedra,^{14,15,26-29} one-dimensional chains and ladders,³⁰⁻³⁵ two-dimensional sheets,³⁶⁻⁴⁴ and three-dimensional networks,^{13,45-47} many of which possess interesting chemical and physical properties.

One area of potential application for supermolecular assemblies is in the area of nanoscale devices. The electronics industry, in particular, is on a continuous quest for smaller, faster components, and less-expensive fabrication methods. The last few decades have seen a dramatic decrease in component sizes and increases in computer speeds, but the trend may be approaching a limit. It is generally agreed that optical diffraction and the opacity of lens materials or photomask supports will likely make current photolithographic methods ineffective for fabricating features below 100 nm.⁴⁸ To truly break into the nanoscale regime, a new "bottom up" approach may be beneficial. One can envision a process where individual molecular building blocks can be assembled into nanoscale conductors or switches. It is by this method that the synthetic chemist may find application in supermolecular assembly processes.

In addition to electronic devices, high-density magnetic storage media are also attractive endeavors for supermolecular chemists. Molecular magnets offer advantages such as size homogeneity, solubility, transparency, relatively benign synthetic conditions,

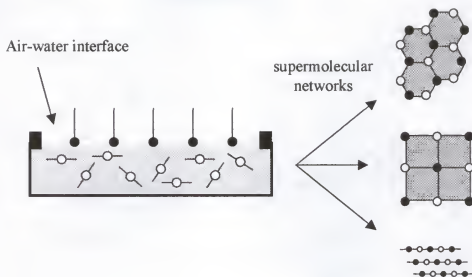
and the potential for multifunctional materials.⁴⁹⁻⁵⁶ To date, magnetic clusters with significant reversal fields have been realized; however, molecular magnets with practically useful blocking temperatures remain elusive.¹⁶⁻²⁵

The application of self-assembly methods to the fabrication of nanoscale devices is still in its infancy, and the level of control and complexity needed for such sophisticated materials has yet to be realized. However, one can argue based on the results reported to date that the potential exists. What is needed now is a better understanding of the self-assembly process and what tools the chemist can use to direct the architectures of the final materials. In addition, since many of the aforementioned applications of supermolecular systems will require the positioning, servicing, and interfacing of these systems at surfaces,⁵⁷⁻⁶⁵ we have undertaken an investigation into the structure directing ability of an interface in the assembly process and what conditions would allow for the positioning of coordinate-covalent networks at a surface.

Assembling Inorganic Networks at Interfaces

From the numerous interfaces available for study, we chose the air-water interface as our medium in which to work. The choice was obvious for several reasons. The air-water interface is readily available and inexpensive; aqueous monolayers systems (otherwise known as Langmuir monolayers) have been well studied by our group and countless others over the past century; many experimental techniques are available and well understood for characterizing Langmuir monolayers; the final products can often be transferred to solid supports by the Langmuir-Blodgett technique for further characterizations of their structure and physical properties.^{66,67}

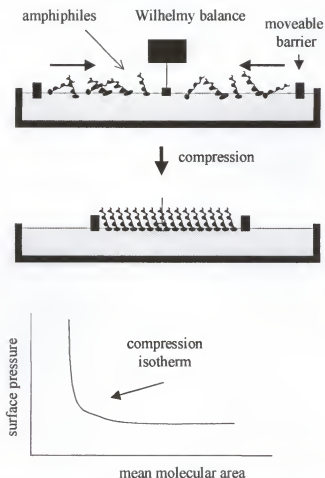
The general strategy is outlined in Scheme 1-1. To form extended inorganic networks at the water surface, an amphiphilic ligand system or transition metal



Scheme 1-1. A strategy for assembling coordinate covalent networks at the air-water interface. The geometry of the networks can be controlled through appropriate choice of amphiphile, bridging species, and solute building blocks.

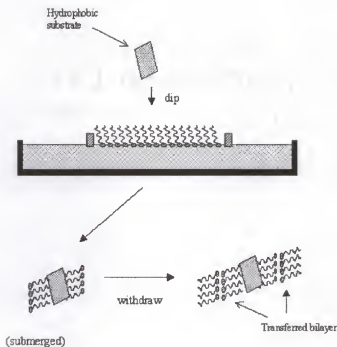
complex is spread in sufficient quantity to form a molecular monolayer on the water surface. The subphase will be a solution of another metal complex. Either the amphiphilic complex or the dissolved complex will contain cyanide ligands that can act to bridge the two complexes together resulting in a coordination polymer at the air-water interface. To achieve the desired geometrical product, either the complexes themselves will be designed with appropriate blocking ligands attached, or the air-water interface will direct the two-dimensional motif by limiting reactivity in the third direction.

The process for characterizing molecular monolayers on water surfaces by surface pressure vs. area isotherms was first described by Langmuir in 1917,⁶⁸ and is outlined in Scheme 1-2. A volatile solution of an amphiphilic molecule is spread on a water subphase contained in a Teflon trough. By compressing the moveable barriers, the



Scheme 1-2. A schematic depiction of the control and characterization of molecular order in aqueous Langmuir monolayers is shown. As the film is compressed, organization of the amphiphiles occurs resulting in a change in surface tension. The variation in surface tension is monitored by a Wilhelmy balance and is converted to a surface pressure vs. mean molecular area isotherm.

effective surface area per molecule decreases and the molecules are forced to close-pack into a condensed state. During the compression, the surface tension as measured by the Wilhelmy plate varies with the degree of order in the monolayers. Extrapolation of the steepest part of the resulting isotherm to the x-axis gives the mean molecular area per molecule. In addition, a flattening of the isotherm at high pressure and smaller area is attributed to the collapse of the film, or the limiting mean molecular area. The behavior



Scheme 1-3. A schematic depiction of the Langmuir-Blodgett technique for preparing thin films for aqueous Langmuir monolayers is shown. In addition to the method shown, transfer can also result by starting with a hydrophilic surface submerged in the subphase followed with a single up-stroke. The method thus provides a unique level of control in preparing monolayer to multilayer thin films.

of the isotherm can give indications as to whether the amphiphiles have cross-linked into a polymeric network on the water surface. Changes in the onset area, slope, and limiting mean molecular area between isotherms on pure water and isotherms run on metal containing subphases give definitive evidence for an interaction between the amphiphile and the subphase metal ions.

Thin Film Characterization Techniques

Conventional Methods

Characterization of reaction products formed at an air/water interface presents a significant challenge since the quantity of material is on the order of micrograms. To

obtain further evidence of reaction it becomes necessary to collect the film onto a solid support. The Langmuir-Blodgett technique, as shown in Scheme 1-3, allows for the transfer of a monolayer from the water surface onto a hydrophilic or hydrophobic surface. The Langmuir-Blodgett technique is a method for preparing multilayer assemblies by a step-wise deposition procedure.^{66,67} The film is compressed to the desired surface pressure and the substrate is dipped through the film into the subphase. The alkyl chains interact with the substrate on the down stroke and transfer to the solid support. The surface at the end of the dip is now terminated with the hydrophilic end of the amphiphiles and, upon removing the substrate, another layer of amphiphiles is transferred on the upstroke. The result is a bilayer of the amphiphiles held together through dipolar or covalent interactions between the hydrophilic head groups of the amphiphiles. The method also allows for the transfer of a single monolayer if the solid substrate is hydrophilic and the deposition procedure starts with the substrate submerged in the subphase.

As alluded to earlier, the structural characterization of the sub-microgram quantities present in thin films presents a significant challenge. The transferred film can be subjected to analysis by FTIR, UV-Vis, X-ray photoelectron spectroscopy (XPS), atomic force microscopy (AFM), scanning electron microscopy (SEM), and X-ray diffraction. To use UV-Vis and FTIR spectroscopies to characterize small quantities of materials like those obtained in monolayer reactions at a water surface, intense absorption processes in the product are needed. With transition metal complexes, d-d absorption bands are typically weak and the presence of other more intense absorption mechanisms,

such as ligand-to-metal charge transfer, or ligand π - π^* transitions is needed in order to be a useful characterization method in thin films.

FT-IR spectroscopy is usually quite useful in the study of thin films. The sensitivity of the method to submonolayer amounts of material is made possible through attenuated total internal reflectance crystals, hereafter named ATR crystals. These substrates are single crystal silicon or germanium and can be used clean as hydrophilic substrates or made hydrophobic by application of a layer of an alkyl silane. The geometry of the crystal is such that the incident IR radiation is internally reflected resulting in an evanescent wave that travels parallel to the sample surface. Vibrational modes with moderate to high absorptivities, such as C-H, C-N, and C-O are readily observed in monolayers quantities. This technique is used repeatedly throughout the experiments described hereafter since the majority of the complexes involved contain the cyanide ligand, and cyanide-stretching vibrations are quite intense.

Cyanide complexes can be well characterized by FT-IR spectroscopy by monitoring the C-N stretching frequency. These vibrations vary in frequency with changes in metal oxidation state and coordination environment.⁶⁹ This behavior is rationalized by considering the orbital interactions that are involved in transition metals complexed to cyanide. The cyanide anion lone pair is predominantly located on the carbon and nearly all of the monomeric cyano-complexes known are coordinated through carbon. This interaction has a strong sigma bonding interaction and effectively lowers electron density in the C-N antibonding orbital. As such, coordination of C-N to a metal center results in an increase in the C-N stretching frequency compared to the free ion. The C-N antibonding orbitals are low enough in energy to have significant π -bonding

interactions with the metal center as well. The metal donates electrons to this antibonding orbital through a process called back-bonding. The more efficient the back-bonding, the weaker the C-N bond, and the lower the C-N stretching frequency becomes. As a consequence of these two mechanisms, a general trend is observed as one progresses across the first row transition metals. For trivalent metal ion complexes, the higher nuclear charge from chromium(III) to cobalt(III) is expected to increase the sigma donation and strengthen the C-N bond; however, this is nearly balanced by an increased ability to back-bond to the ligand, which is working to weaken the C-N bond. The result is that the C-N stretching frequencies remain nearly constant for the hexacyanides of chromium (III) through cobalt (III), occurring around 2130 cm^{-1} . Another trend observed in metal-cyanides is that the C-N stretching frequency is lower for the divalent complex since the lower cationic charge decreases cyanide to metal sigma bonding and increases metal to cyanide back-bonding. Thus, $\text{K}_3\text{Fe}(\text{CN})_6$ shows a C-N stretch at 2130 cm^{-1} , whereas the same vibration occurs at 2060 cm^{-1} in $\text{K}_4\text{Fe}(\text{CN})_6$. A final consequence of the bonding interactions, and perhaps the most useful effect for characterizing polymeric metal cyanides, is the shift of the C-N stretching frequency when both the C and N atoms are coordinated. Coordination at the nitrogen end is similar in nature to the sigma donation of the C end, but with minimal back bonding abilities. The result, again, is that coordination through nitrogen removes electron density from the C-N antibonding orbital and strengthens the C-N bond.⁷⁰ This, combined with kinematic effects resulting from the increased rigidity of the structure, works to shift the C-N stretch to higher frequencies when cyanide assumes a linear bridging mode.⁷¹⁻⁷³ Therefore, this shift will be a key

signature of the formation of cyanide bridges in the structures prepared at the air-water interface.

Elemental composition of thin films can be accomplished through X-ray photoelectron spectroscopy (XPS). X-ray photoelectron spectroscopy is a surface sensitive technique that distinguishes elements by the binding energies of their valence electrons. The sample is prepared on a conducting substrate such as silicon, and subjected to an electron beam of varying energy. An energy sensitive detector analyzes the energy spectrum of the electrons ejected from the top few layers of the sample. Peaks will occur in the spectrum at energies corresponding to the binding energies of the electrons. Since these energies are unique to the specific elements of interest, they provide a method for the identification of the elements present in the sample. Further information is obtained by integrating the peak area in combination with calculations for the photo-quantum yield of the transition observed. The resulting ratio of integrated peak areas is proportional to the ratio of elements in the sample.

Surface morphology in thin films can be investigated by microscopic techniques such as SEM and AFM. Scanning electron microscopy is useful when lateral resolution on the sub-micron level is sufficient. For more detailed analysis where higher lateral resolution or accurate depth measurements are necessary, one must resort to AFM. With the appropriate choice of tips and scanning heads, AFM can give detailed surface morphology measurements with lateral resolution on the order of nanometers and depth resolution on the order of angstroms over sample areas varying from tens of nanometers to a hundred microns. Indeed, with certain systems where tunneling tips are applicable, lateral resolution can approach the angstrom level, giving a true atomic picture of the

surface composition. This technique is usually limited in its application for LB films since the surface layer is typically comprised of methyl terminated alkyl chains, which effectively mask the inner bilayer structure of interest.

Conventional X-ray sources can be used to characterize the lamellar organization in LB films. For well-organized LB films, the system mimics a powder diffraction pattern of a layered system under conditions of extreme preferred orientation. The plate-like domains are randomly arranged in the xy-plane, but have their z-axes aligned parallel. As such, the diffraction pattern will consist of a series of (00*l*) peaks which can be indexed to yield interlayer lattice spacings (*d*) by the Bragg equation: $n\lambda = 2d\sin(\theta)$, where θ is one-half the angle (2θ) where the diffraction peak occurs. In well-organized LB films, the (00*l*) peaks can be very intense and observable with a film thickness on the order of 10 bilayers. Diffraction arising from the in-plane structure is typically several orders of magnitude less intense since there is no preferred orientation of the in-plane scattering vectors and acquisition times are usually too long on a conventional diffractometer to be of use. In addition, the random scattering from the substrate is very intense relative to the scattering due to the thin film sample, and a special technique called grazing incidence X-ray diffraction (GIXD) is required to improve the signal to noise ratio. This technique is best performed using high brilliance X-ray sources such as synchrotrons. The GIXD experiment and another thin film characterizations using synchrotron radiation called X-ray absorbance fine structure (XAFS) will be described in detail in the following section.

Characterization of Thin Films Using Synchrotron X-ray Radiation

Synchrotron radiation⁷⁴ is produced in large particle accelerators called storage rings. A storage ring is a large, evacuated circular ring that may be a kilometer or more in circumference. It is lined with steering magnets (bending magnets) and rf generators, which work in tandem to keep packets of positrons or electrons circulating at energies of several gigaelectron volts. At these energies, the particles travel at velocities very near that of light. A consequence of this circular trajectory is a constant transverse acceleration of the packets of charged particles and a continuous emission of white radiation. The energy of this radiation is dependent on the energy of the particle beam and spans the region from ultraviolet to hard X-rays. The X-ray radiation is many orders of magnitude more intense than that from a typical diffractometer. Relativistic effects also work to force a very narrow collimation of the resulting radiation. This collimation makes a synchrotron source comparable to an optical laser with regard to beam divergence. This broad band of radiation leaves tangentially from the “bending magnets” in the storage ring at several different locations called beamlines. These beamlines can be equipped with optics and/or crystal monochrometers to select single wavelength radiation as necessary for individual experiments. These types of synchrotrons employing bending magnets are termed “second generation” synchrotrons.

The research requiring synchrotron radiation reported in this dissertation was performed at the Advanced Photon Source (APS), Argonne National Laboratory, Argonne, IL.⁷⁵ An aerial photograph and schematic of the facility are shown in Figure 1-1. Production of the beam begins with an electron gun that emits 100 keV electrons into a linear accelerator (linac). Here the electrons are ramped in energy by a series of accelerating structures to 200 MeV before striking a water-cooled 7 mm thick

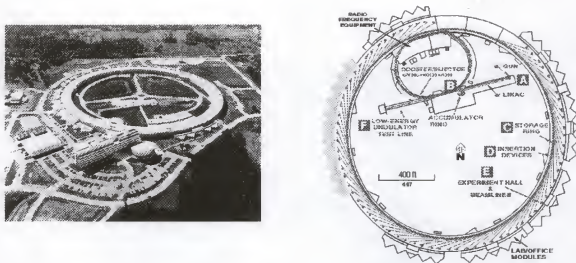


Figure 1-1. An aerial photograph and schematic depicting the synchrotron facility at the Advanced Photon Source, Argonne, IL (taken from reference 75).

tungsten disk. This interaction produces electron-positron pairs. The APS can operate using either electrons or positrons, but positrons are normally selected since their positive charge minimizes interactions with residual gas ions in the ring. The positrons are sent through a second stage linac that further accelerates them to 450 MeV. From here, the positrons are sent to a 368 m circumference booster ring where four 5-cell rf cavities increase the positron energies at a rate of 32 keV per turn. In 0.25 sec, the positrons orbit the ring 200,000 times as their energy climbs to 7 GeV. At this energy, the positrons have a velocity approximately equal to the speed of light. They are then injected into the 1104 m circumference main storage ring that is configured as a set of curves connected by straight sections. As the positrons change trajectory, their velocity changes, and radiation is emitted tangentially to the arc of the particle beam. Insertion devices, either

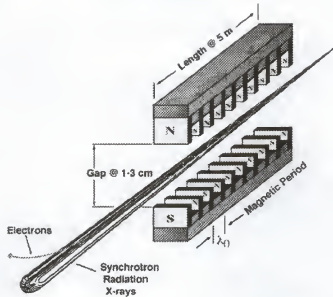


Figure 1-2. A schematic of a typical (undulator or wiggler) insertion device showing the rows of alternating pole magnets. Interaction of the radiation with the magnetic field results in an enhanced intensity of the X-rays through constructive interference effects. Synchrotrons such as the Advanced Photon Source, which employ insertion devices, are known as third-generation facilities (image taken from ref 75).

wigglers or undulators, are incorporated into the straight sections and greatly enhance the synchrotron radiation.

Facilities, such as the APS, which incorporate insertion devices are known as a “third generation” synchrotrons. These devices consist of a series of magnets oriented horizontally (wigglers) or vertically (undulators) to the main beam path (Figure 1-2). The magnetic poles alternate in polarity and introduce a sinusoidal motion to the main beam. This acceleration results in the emission of radiation. Undulators use a series of small deviations to produce an interference effect that results in nearly monochromatic radiation with vastly enhanced intensity. Wigglers, on the other hand, introduce a stronger magnetic field that destroys the sinusoidal motion via relativistic effects and

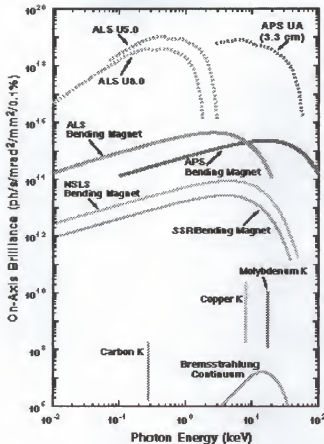


Figure 1-3. The X-ray brilliance of the Advanced Photon Source (APS) compared to other X-ray sources (taken from reference 75). Facilities such as the APS that incorporate insertion devices are known as a "third generation" synchrotrons.

produces equal intensity radiation over a broad range of energies. Compared to a bending magnet source employing a single magnetic pole, the radiation from a wiggler is enhanced relative to the number of magnetic poles. The insertion devices can produce a power density higher than that found on the surface of the sun and a combination of flux and brilliance $10^4 - 10^6$ greater than conventional X-ray sources (Figure 1-3). Third-generation storage rings maximize those x-ray beam qualities, flux and brilliance, that are needed for frontier experimentation. Flux and brilliance are benchmarks of x-ray beam quality. Both are based on a measure of the number of photons per second in a narrow

energy bandwidth and in a unit of solid angle in the horizontal and vertical directions.

Flux is the number of photons per second passing through a defined area, and is the appropriate measure for experiments that use the entire, un-focused x-ray beam.

Brilliance is a measure of the intensity and directionality of an x-ray beam. It determines the smallest spot onto which an x-ray beam can be focused.

Thirty-five "sectors" are marked on the experiment hall floor. Each of these sectors comprises two beamlines, one originating at a bending magnet in the storage ring lattice, the other at an insertion device. These sectors are the domain of the APS users and are the locations where a wide range of experiments take place. The beamline in which the University of Florida has an interest is maintained by a multi-institutional consortium call the Materials Research Collaborative Access Team, or MRCAT, and is located at sector 10ID.⁷⁶

The MR-CAT undulator line is fully operational. As described earlier, an undulator insertion device provides enhanced X-ray intensity over a narrow energy range. Experimenters have control over the undulator and can tune the energy range of the output by adjusting the "gap" between the magnetic poles. The larger the gap, the wider the energy range and lower the intensity of the resulting radiation. Typically the gap is set to 100-200 eV to compromise intensity and beam stability. Final selection of monochromatic radiation over an energy range of 4.8-30 keV is accomplished by a cryo-cooled Si (111) double crystal monochromator designed by the IIT Center for Synchrotron Radiation Research. The optimum energy range is between approximately 6 keV and 13 keV, since lower energy radiation is strongly scattered by air and higher energies require operation with crystal harmonics. As such, operations outside of the

optimum range, while possible, are less trivial and require greater attention to experimental parameters. The second crystal has a piezoelectric tuning actuator with a.c. feedback and a Bragg-normal motion that permits some degree of fixed-offset operation. The monochromator assembly is housed in a separate hutch (called the A-hutch) that is upstream from the main experimental station.

The term monochromator is somewhat of a misnomer since the radiation coming off the crystals contains harmonics due to higher order Bragg reflections. This is compensated for inside the main experimental hutch (called the B-hutch) by reflecting the beam off a flat, 60 cm long harmonic rejection mirror with Pt and Rh coatings. By adjusting the tilt of the mirror, the lower energy radiation can be selectively reflected while the higher energy harmonics are unaffected. This angle can be found by scanning the mirror tilt and monitoring the intensity of the reflected beam. The intensity will remain relatively constant until the angle passes a critical angle where the intensity drops rapidly. By setting the mirror tilt at a value just prior to the cut off angle, higher energy radiation is effectively discriminated since the angle at this position is above the critical angle for the higher energy components. The profile of the beam coming off the mirror is ovalar with a width of ~ 5 mm and a height of ~ 3 mm. The intensity of the beam varies over this area, with the most intense section in the center of the beam. A homogeneous section is selected by the use of motorized slits with a motor resolution on the order of microns.

The presence of a vertically deflecting mirror at the front of the experimental station requires all optical components to be mounted on an incline in order to be inline with the X-ray beam. This is accomplished by use of an X95 rail system, which also

performs the function of standardizing all component mounts to one of two rail-to-beam distances. A second float glass mirror is available for use as a steering mirror for liquid scattering experiments. This allows for a more facile transition between experimental operations.

The X-rail terminates down stream at an 8-circle Huber goniometer that is mounted on a large positioning table. The table can be moved vertically and horizontally perpendicular to the beam to synchronize the goniometer center to the beam position. Two of the 8 circles that control the detector position have encoded motors that permit continuous scanning and data acquisition using the multichannel scaler described below.

Several detector types are available for use in MR-CAT sector. High flux measurements, such as those required for incident beam monitoring, are accomplished through Daresbury design spectroscopy ion chambers for use on the main X95 spectroscopy rail or with smaller Cornell-type ion chambers that may be mounted on the spectroscopy rail or on the Huber goniometer detector arm. Lytle-type fluorescence detectors are also available and typically used in XAFS spectroscopy. The goniometer detector arm can be fitted with sensitive NaI scintillation detectors for high-resolution diffraction experiments. Data collection is accomplished through an instrument chain of Keithley electrometers, V-F converters and a 32 channel multi-channel scaler. The multi-channel scaler permits the simultaneous monitoring of the monochromator energy, detector outputs, and the goniometer detector motor positions for use in slew scan operations. Motor commands and data acquisition are handled by the MX system, written by William Lavender.⁷⁷

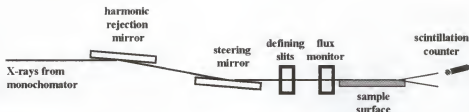


Figure 1-4. Schematic showing the experimental set-up for GIXD experiments. The sample surface can be either a solid support or a water surface. The steering mirror is float glass coated with a platinum strip and controls the incident angle to the water surface. For solid samples, the steering mirror is unnecessary since the incident angle can be controlled by the sample position.

Grazing Incidence X-ray Diffraction (GIXD)

To obtain X-ray diffraction patterns of monolayers requires a specialized technique developed over the past two decades (Figure 1-4). The technique is called grazing incidence X-ray diffraction (GIXD) and requires intense X-rays from synchrotron sources. The theory behind the technique has been described in detail and only a brief outline will be presented here.⁷⁸

The theory behind the technique is based on well-known laws of optics that govern the interaction of electromagnetic radiation with interfaces consisting of a change in index of refraction (n). A wave incident on a flat interface at some angle α_i is both refracted into the second medium and reflected off the surface. As α_i approaches some critical angle, α_c , the angle of the refracted wave with respect to the surface approaches zero and the incident wave is totally reflected. At incident angles just below the critical angle, the incident wave vector factorizes into two components, one horizontal and one vertical. This horizontally propagating (evanescent) wave has an exponentially dampened amplitude along the surface normal and a resulting penetration depth that

varies as a function of the incident angle. At X-ray wavelengths, the penetration depth in water when $\alpha_i = \alpha_c$ is approximately 100 nm, but decays rapidly to approximately 5 nm when $\alpha_i = (\frac{1}{2})\alpha_c$. The critical angle for water, at X-ray energies on the order of 10 keV, is ~ 2.4 mRad. At this angle, the incident radiation has become surface sensitive. At $\alpha_i = \alpha_c$, the evanescent and incident waves are in phase and the amplitude of the evanescent wave is effectively doubled. Since intensity is the square of the amplitude, the evanescent intensity is quadrupled at the critical angle. As the incident angle decreases below the critical angle, the incident and evanescent waves become more and more out of phase and the intensity of the evanescent wave decreases. In a typical GIXD experiment, the X-rays are incident on the water surface at $\sim 0.85\alpha_c$, which is an effective compromise between keeping the X-rays surface sensitive and keeping the evanescent intensity high. This same approach applies to LB films transferred onto solid supports as well.

This experimental technique has been readily applied to the structural characterization of aqueous Langmuir monolayers and LB films.⁷⁸⁻⁸⁰ In all cases of crystalline films, the materials are found to behave as 2D powders. That is, there is no preferential orientation of Bragg planes and the crystals are randomly dispersed through rotational disorder about the z-axis perpendicular to the plane of the film. While these two-dimensional powder patterns do not provide the detail available in traditional single crystal diffraction experiments, knowledge of the limited structural motifs possible for the packing of alkyl chains combined with lattice-energy calculations and the information derived through GIXD experiments can provide a structural picture of the LB film in surprising detail.⁷⁸⁻⁸⁰

In the simplest model, a domain of the film is treated as a two-dimensional crystal consisting of uniformly oriented rigid molecules. The scattering pattern is then governed by the structure factor reflecting translational order of the molecular centers in the plane of the monolayer and the form factor of the individual molecules. The translational order within the xy -plane will give rise to a diffraction peak at 2θ when the $(h\ k)$ lattice planes make an angle θ_{hk} with the evanescent beam fulfilling the Bragg condition $\lambda = 2d\sin(\theta_{hk})$. Unlike a three-dimensional crystal, there is no restriction on the z -component of the scattered beam. The Bragg scattered beam may go into the water or exit the surface at an angle θ_z . As a result, the 2D lattice confines the scattering vectors to Bragg rods instead of points. The Bragg rod will have an intensity profile, due to interference effects between the scattered wave and the wave reflected from the surface. The two waves will be in-phase when the scattered angle, θ_z , matches the critical angle, α_c , and a maximum will occur in the Bragg rod profile. At higher angles, the two waves become out of phase and the intensity decays. Coupled with this phenomenon, is the interaction of the molecular form factor with the Bragg rod profile. The structure factor for a rod like molecule is large only on a plane perpendicular to the rod long axis. The intersection of this plane with the Bragg rods will give rise to diffraction maxima.

Analysis of the GIXD patterns for Langmuir monolayers has been described in intricate detail⁷⁸⁻⁸⁰ and the following brief description of the method is heavily borrowed from these references. Close-packed alkyl chains, assuming rotational symmetry, can basically adopt three packing motifs: hexagonal, centered-rectangular, and oblique. If the molecules are all standing perpendicular to the film plane and the packing has hexagonal symmetry; in rectangular notation, the three lowest order peaks $(0\ 2)$, $(1\ 1)$ and $(1\ -1)$ are

degenerate (the (1 0) and (0 1) reflections are absent due to symmetry), and the Bragg rod will have its maximum at $\theta_z = 0$. If the molecules are all standing perpendicular to the film plane, and the unit cell stretches or shrinks towards a nearest neighbor, the cell is centered-rectangular. The (0 2) degeneracy is removed and two peaks with an approximately 2:1 intensity ratio will be observed in the xy-plane. If the unit cell stretches towards a nearest neighbor, the (0 2) peak will be at a larger angle than the (1 1) (1 -1) degenerate peak. If the cell shrinks, the opposite inequality is observed.

Symmetry can also be removed by tilting of the alkyl chains. If the alkyl chains tilt in a nearest neighbor direction, the cell is distorted to centered-rectangular and one of the degeneracies is removed. The result again is that two peaks with an approximately 2:1 intensity ratio will be observed in the xy-plane. The Bragg rods for the two peaks will have different intensity profiles with the non-degenerate peak having its maximum at $\theta_z = 0$, and the degenerate peak will have its maximum at $\theta_z > 0$ with θ_z dependent on the magnitude of the molecular tilt. To calculate the tilt angle, it's more convenient to plot the diffraction data relative to the incident wavevector "K" where $K_{xy} = (4\pi/\lambda)\sin\theta_{xy}$ and $K_z = (2\pi/\lambda)\sin\theta_z$. Now the tilt angle ϕ can be calculated via the relationship $\tan \phi = K_{dz} / [(K_{dxy})^2 - [(1/2)(K_{nxy})]^2]^{1/2}$ where K_{dz} is the K_z value for the degenerate reflection, K_{dxy} is the K_{xy} value for the degenerate reflection, and K_{nxy} is the K_{xy} value for the non-degenerate reflection. Similar geometric arguments can be applied to calculate tilt angles when the alkyl chains tilt towards a next-nearest-neighbor, or in an intermediate direction.⁷⁹

For the systems described throughout this dissertation, the analysis of the diffraction data is concerned primarily with the structure of a two-dimensional inorganic

network contained within the Langmuir monolayer or Langmuir-Blodgett film. The structure of the organic chains are of secondary importance since the rigid nature of the inorganic lattice will most often be incommensurate with the alkyl chain packing. The result of such a mismatch will be either a disordered arrangement of the organic chains or the formation of small aggregated domains, neither of which are well suited to fulfill the conditions for high quality diffraction. The interpretation of the diffraction data can also be more complex for inorganic systems, since the number of packing arrangements and possible lattices are much larger than in simple rod-like hydrocarbon chains. The Bragg rod profiles for planar inorganic networks will have their maximum intensity at the horizon due to the finite thickness of the quasi-two-dimensional system and as such yield little structural information. Interpretation of the in-plane diffraction pattern is made somewhat simpler by the reduction in Miller indices to two values for a planar lattice. Additional information can also be obtained through systematic absences present in the indexed diffraction peaks that result from crystal symmetries. However, a complete solution to the structure is still difficult if not impossible due to the infinite possible arrangements of the constituent atoms. The best approach is to use comparisons to analogous solid-state structures in combination with a chemical intuition of typical bonding arrangements and complex geometries to arrive at a structure that agrees well with the diffraction data.

X-ray Absorption Fine Structure (XAFS)

Complementary to x-ray diffraction is another technique useful in the structural characterization of materials. The technique is x-ray absorption fine structure (XAFS).^{81,82} When a collimated beam of monochromatic radiation travels through matter of thickness x , its intensity decays according to $I / I_0 = e^{-\mu x}$, where I_0 and I are the

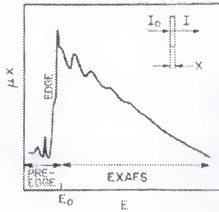


Figure 1-5. The absorbance coefficient for a typical substance at X-ray wavelengths spanning an adsorption edge energy (E_0). The fine structure is the result of interference effects between the propagating and backscattered photoelectron waves. The fine structure in the post edge region is the phenomenon known as XAFS (figure taken from reference 82).

incident and transmitted intensities and μ is the linear absorption coefficient. As the energy of the photons is increased, μ generally decreases until a critical energy is reached where the absorption suddenly increases several-fold. This discontinuity is referred to as an absorption edge and relates to the ejection of a core electron from an atom to a continuum state. Further increasing the energy will cause a further decrease in μ until another absorption edge is encountered. These absorption processes are designated as K, L, M, etc. according to the orbital state from which they originate. There is one absorption edge for the K shell, three for the L shell, five for the M shell, and so on.

Closer inspection of the X-ray absorption spectrum for materials often reveals a fine structure in the μx vs. E plot in the pre-edge and post-edge regions, Figure 1-5. Peaks in the pre-edge region arise from absorption processes involving the excitation of core electrons to bound states and can provide insight into bonding information such as

energetics of virtual orbitals, electron configuration, and site symmetry. Oscillations in the region 40-1000 eV beyond the absorption edge arise from final state interference effects involving scattering of the outgoing photoelectron from the neighboring atoms. These oscillations are the XAFS for X-ray absorption fine structure (also called EXAFS by some authors). In between the pre-edge and post-edge regions is the X-ray absorption near edge structure (XANES) that arises from effects such as many-body interactions, multiple scattering effects, distortion of the excited state wavefunction by the coulomb field, band structures, etc.

Since XAFS is an effect arising from the interference of the outgoing photoelectron wave from the absorbing atom with an incoming wave backscattered from a neighboring atom, then a detailed analysis of this interference effect could provide details about the local structure surrounding the absorbing atom. Indeed, this is the value of XAFS spectroscopy. As a local probe, XAFS can complement X-ray diffraction data since diffraction arises from a periodic arrangement of atoms over a large lattice and XAFS focuses on the coordination shell within 10 Å of the absorbing element. Of course, XAFS cannot compete with the amount of information available through single crystal diffraction where complete structure solutions are derived. But with samples where single crystals are unavailable, XAFS can offer a unique probe into local environments that may not be obtainable by other methods. For example, XAFS is applicable to gasses, liquids, solutions, and crystalline or amorphous solids. In addition, since XAFS results from an absorption process, it is element specific. Although the XAFS phenomenon and its basic explanation in terms of quantum mechanical interference effects have been known since the 1930, the phenomenon did not become a

practical experimental tool until Sayers, Stern, and Lytle distilled the essential physics of the process into the standard XAFS equation and proposed a simple method of data analysis.⁸³ This achievement, coupled with the availability of tunable, high flux, high energy-resolution synchrotron facilities, has led to an exponential growth in the number of XAFS experiments performed since 1970.

The interpretation of an XAFS spectrum, $\chi(E)$, acquired as a function of energy, first involves normalization to the background absorption (μ_0) by

$$\chi(E) = [\mu(E) - \mu_0(E)] / \mu_0(E) \quad [1-1]$$

followed by the conversion from E space to k space via the relationship

$$k = [(8\pi^2 m / \hbar^2)(E - E_0)]^{1/2} \quad [1-2]$$

from which structural parameters can then be determined by application of the standard XAFS equation

$$\chi(k) = \sum N_j S_i(k) F_j(k) e^{-2\sigma_j^2 k^2} e^{-2r_j / \lambda_j(k)} \frac{\sin(2kr_j + \phi_{ij}(k))}{kr_j^2} \quad [1-3]$$

Here $F_j(k)$ is the backscattering amplitude from each of the N_j neighboring atoms of the j th type with a Debye-Waller factor of σ_j (to account for thermal vibration and static disorder). The total phase shift of the photoelectron is $\phi_{ij}(k)$ and contains contributions for the absorbing atom i and the backscattering atom j . The term $e^{-2r_j / \lambda_j(k)}$ takes into account inelastic losses in the scattering process with λ_j being the electron mean free path, and the amplitude reduction factor, $S_i(k)$, takes into account inelastic losses due to multiple excitation. Thus, each XAFS wave is determined by the backscattering amplitude ($N_j F_j(k)$) modified by the reduction factors $S_i(k)$, $e^{-2\sigma_j^2 k^2}$, and $e^{-2r_j / \lambda_j(k)}$, the $1 / kr_j^2$

distance dependence, and the sinusoidal oscillation which is a function of interatomic distances ($2kr_j$) and the phase shift ($\phi_j(k)$).

A theoretical discussion on the origin of these parameters and their relevant effects on XAFS spectra is beyond the scope of this introduction;^{81,82} however, a few general points can be made. Since the sinusoidal XAFS oscillation results from the interference $\sin(2kr)$ term, with a frequency $2r$ in k space, the more separated the absorbing atom and backscattering atom (larger r) the higher the frequency of the oscillation. The intensity of a spherically propagated wave decreases as $1/r^2$, so the XAFS amplitude decays rapidly with distance. While the amplitude function $F_j(k)$ depends mainly on the type of backscatterer, the phase function contains contributions from both the propagating atom and the backscattering atom. It should also be mentioned that the standard XAFS equation is an approximation based on the assumption that the process results from a single-scattering event. This is normally a valid assumption since multiple-scattering pathways are merely a sum of all the scattering pathways that originate and terminate at the central (absorbing) atom. As such, the path lengths are typically quite large resulting in significant attenuation and high frequency oscillations that tend to destructively interfere. Multiple-scattering can become important when atoms are aligned in a collinear array. In these types of systems, the propagated wave is strongly forward-scattered by the intervening atom, resulting in significant amplitude enhancement. This process is most evident in systems where the bond angles are $180 \pm 30^\circ$. In these cases, modifications to the standard XAFS equation are necessary to take into account the multiple scattering processes.

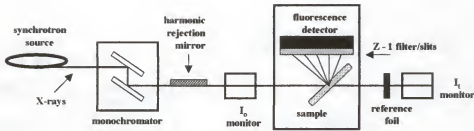


Figure 1-6. Schematic of an experimental setup for collection XAFS spectra in fluorescence mode.

The discussion to this point has centered on XAFS taken in absorbance mode, but the technique is also applicable in fluorescence mode. In fact, for thin film samples, such as those obtained by LB methods, the absorbance due to the sample is negligible and data can only be collected as fluorescence. A schematic of a typical experimental arrangement for collecting fluorescence XAFS spectra is shown in Figure 1-6. The source radiation is scanned over the required energy range by movement of the monochromator and reflected off a harmonic rejection mirror located inside the experimental hutch. The incident flux is monitored by an ion chamber positioned upstream from the sample-fluorescence detector assembly. The sample is then oriented 45° relative to the incident beam. The fluorescence detector (Lytle detector) is then placed at 45° relative to the sample with a Z-1 filter placed between the sample and Lytle detector. There is also a set of collimators oriented between the sample and Lytle detector to minimize randomly scattered X-rays from reaching the detector. A thin foil of the same element to be measured in the sample is positioned behind the sample housing and in front of a second ion chamber so that a reference absorbance edge can be measured *in situ*. This reference foil provides a convenient method of energy calibration since the absorbance edge is known to within a fraction of an eV for most elements. The measured

fluorescence spectrum can then be converted to an experimental spectrum $\mu(E)$ where the y-axis is the total linear absorption coefficient and the x-axis is energy. For fluorescence experiments, $\mu(E)$ is calculated by $\mu(E) = F / I_0$ where F is the measured fluorescence intensity and I_0 is the measured incident X-ray intensity. Prior to the experiment, the linearity of the detector responses should be verified. This can be accomplished by monitoring the ratio F / I_0 with full I_0 and after attenuation with appropriate filters to $(1/2)I_0$. If the detectors are linear, the ratio of F / I_0 will not vary by more than a few percent. If the response is not linear, then the sensitivity of the detectors should be adjusted by varying the detector gasses. To minimize background scattering from the sample support, the sample should be prepared on an "X-ray transparent" support such as Mylar.

An XAFS scan normally involves scanning the energy from ~ 150 eV before the edge to ~ 1000 eV past the edge. The scan step size can be varied to give a higher resolution in the vicinity of the edge (~ 1 eV / step) and a slightly lower resolution after the edge (~ 3 -5 eV / step). In addition, multiple scans can be taken and averaged for a better signal to noise ratio.

Once the data has been collected, the process of extracting the important structural information from the XAFS spectrum can begin. This process is greatly simplified by application of an appropriate software package such as WinXAS⁸⁴ that has been designed specifically for XAFS data reduction. In addition, the WinXAS program has been designed to accept inputs from modeling programs such as FEFF7⁸⁵ which can calculate theoretical XAFS parameters based on atomic coordinates prepared via the input program ATOMS.⁸⁶ Using these three programs in tandem, one can efficiently

perform the background subtractions, Fourier transformations, and curve fitting routines necessary for interpretation of the XAFS data.

The first step in the process of data reduction is the removal of a "raw background" which is normally present as a smoothly varying, low-order polynomial evident in the pre-edge and post-edge data curve and the normalization of the data to the edge step. In the WinXAS program, these steps can be preformed in one step by simply fitting the pre-edge (typically linear) and post-edge data (typically a second order polynomial) to two separate functions and subsequently subtracting them off. The next step is to convert the $\mu(E)$ from E space to k space. In order to do this, the edge energy (E_0) must be determined. With WinXAS, this is done by finding the inflection in the edge step using a second derivate curve. Once (E_0) has been determined, the conversion to k space can proceed by simply selecting the conversion step (with the proper (E_0) input) with the WinXAS program. The data at this stage still contains other "background factors" such as spectrometer baseline, beam harmonics, elastic scatterings, etc., which will are removed by fitting to a cubic spline function. The power and number of nodes in the spline function can be varied to get the best fit. The fit window is varied to provide the best result and is typically in the range $2.5 < k < 11$. Quality of fit can most easily be judged by monitoring the Fourier transformed "radial plot" which varies in real time in WinXas as the fitting window is varied. The main objective is to minimize peaks below one angstrom in the radial plot and to ensure that the radial plot remains relatively constant as the fitting window is changed. It is best to try several different cubic splines to determine which gives the best fit.

Once the background has been subtracted; the final stage is the Fourier transform. This is best done in combination with a Bessel window function that minimizes the high frequency ripples that result from the finite size of the transform data. It is also advisable to truncate the data window at values that give the smoothest continuation from one end of the data window to the next. Once the window has been chosen, the Fourier transform proceeds by opening a separate window where the results are displayed for four different values of k weighting. Typically for transition metals, it is best to use a k^3 weighting factor which amplifies the lower intensity high k data, giving better results.

The Fourier transform now yields the "radial plot" which consists of a series of peaks corresponding qualitatively to different coordination shells. The peak positions are not absolute and are offset by a phase shift. To fit the radial data, one must construct a model of the coordination environment using the program ATOMS. The important data here are atom type, coordination number, bond angles, and bond lengths. These values are read by the input program FEFF and imported into WinXas as the starting points for the fitting routine. The major problem with XAFS fitting is now apparent, as there are several fitting parameters in the XAFS equation to vary. The theoretical values calculated by FEFF are quite accurate, but if at all possible, model compounds should be run with known structures and similar bonding interactions to extract expected variables such as the Debye Waller factor and edge energy shifts. For the FeNi grid network, values were obtained from FeCo Prussian blues reported in the literature. With each variable having a starting value and expected range, the fitting can begin. In the beginning, hold different variables constant, and vary each individually to see the effects of each variable, then steadily progress including more variables until a good fit is

obtained. With a large number of variables, the fit is not absolute, but if the modeled cluster gives a good quality fit with reasonable values of the non-structure variables then the model cluster is well supported.

CHAPTER 2 MIXED-METAL MN-CO PHENYLPHOSPHONATES STRUCTURE AND MAGNETIC PROPERTIES

Introduction

Even before Clearfield's elucidation of the structure of the prototype $\alpha\text{-Zr}(\text{HPO}_4)_2 \cdot \text{H}_2\text{O}$,⁸⁷ layered metal phosphates were extensively studied primarily because of their ion exchange capabilities.⁸⁸ This initial interest has been extended to metal phosphonates where similar architectures are found⁸⁹⁻⁹³ and now includes organic networks that can be varied to further modify the properties of the layered solids.⁹⁴⁻⁹⁹ Recently, layered metal phosphates and phosphonates have been shown to exhibit interesting magnetic phenomena, including magnetic ordering, canted antiferromagnetism¹⁰⁰⁻¹⁰⁷ and antiferromagnetic resonance,¹⁰⁸ and they have been studied as models for two-dimensional (2D) magnetism. Our group has also extended these studies from the solid-state,¹⁰⁹ to monolayer¹¹⁰⁻¹¹² and multilayer thin films,¹¹³⁻¹¹⁹ where similar properties have been observed.

As part of our interest in 2D magnetism in metal phosphonate solids and thin films, we have investigated a series of mixed-metal $\text{Mn}^{2+}/\text{Co}^{2+}$ and $\text{Mn}^{2+}/\text{Zn}^{2+}$ phenylphosphonates. Two possibilities exist if mixed metal phases form, each giving rise to different magnetic behavior. If ions of a different spin state organize in an ordered fashion, then a new superstructure is formed giving rise to the possibility of ferrimagnetism if the spin state of the two ions is different. Alternatively, if the ions

distribute randomly, then a solid solution results. Historically, mixed metal solid solutions have been extensively studied¹²⁰ because they exhibit altered magnetic behavior and provide an opportunity to study the details of magnetic ordering mechanisms. Systems based on $\text{Mn}^{2+}/\text{Co}^{2+}$ have been popular choices, as the materials cover a range of dimensions, from quasi-1D¹²¹⁻¹²³ to quasi-2D¹²⁴ to 3D,¹²⁵ and in most cases an isotropic (Heisenberg-type) interaction describes the coupling between $S = 5/2$ spins of Mn(II) ions, while an anisotropic (Ising-type) interaction describes the coupling between “effective” $S = 1/2$ spins of Co(II) . Consequently, upon dilution these materials experience an interesting blend of competing spin and lattice dimensions. Despite previous studies on mixed-metal solids, there are still some unanswered questions. For example, in some cases, but not all, the combination of random mixing and magnetic frustration leads to spin glass behavior.¹²⁶ In addition, some ferrimagnetic systems have exhibited the interesting effect of negative magnetization.^{127,128} New examples of mixed-metal magnetic systems, either structurally ordered or as solid solutions, can provide the opportunity to further study some of these phenomena.

The divalent metal phenylphosphonates form an isostructural series (Figure 2-1),⁹¹ and we find that the mixed-metal analogs form as solid solutions of formula $\text{Mn}_x\text{Co}_{1-x}(\text{O}_3\text{PC}_6\text{H}_5)_2\text{H}_2\text{O}$ or $\text{Mn}_x\text{Zn}_{1-x}(\text{O}_3\text{PC}_6\text{H}_5)_2\text{H}_2\text{O}$. At low temperature, the pure Mn^{2+} and pure Co^{2+} phenylphosphonates experience long-range antiferromagnetic order at $T_N \approx 12$ K and 4 K, respectively. Upon dilution, the ordering temperatures are reduced compared to the values found for the pure compounds, and the resulting magnetic phase diagrams are reported here. For diamagnetic Zn^{2+} doping, *i.e.* $\text{Mn}_x\text{Zn}_{1-x}$, the reduction of T_N follows the prediction of mean field theory for $x > 0.6$ and this

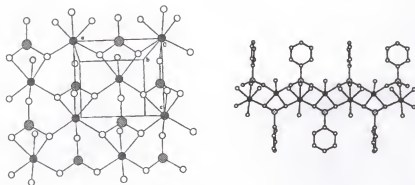


Figure 2-1. In-plane and cross-sectional view of $\text{Mn}(\text{O}_3\text{PC}_6\text{H}_5)\text{H}_2\text{O}$. Crystallographic data are taken from reference 5. Key: oxygen, small open circles; manganese, crosshatched circles; phosphorus, diagonal-hatched circles (phosphorus atoms above and below the plane are distinguished by hatches with different directions).

magnetic phase diagram was reported previously.¹²⁹ However, for the $\text{Mn}_x\text{Co}_{1-x}$ compounds, the reduction of T_N with doping concentration is weaker than expected on the basis of mean field theory. For $\text{Mn}_x\text{Co}_{1-x}$ at low temperatures, the magnetization of the Mn-rich specimens, *i.e.* $x > 0.25$, is characterized by canted antiferromagnetic behavior. On the other hand, the magnetization of the Co-rich specimens, *i.e.* $x < 0.25$, exhibits a very small negative magnetization behavior when the zero-field cooled and field cooled data are compared. The magnetic phase diagram for $\text{Mn}_x\text{Co}_{1-x}(\text{O}_3\text{PC}_6\text{H}_5)\text{H}_2\text{O}$ is reported here.

Experimental Section

Materials used. Reagent grade $\text{Mn}(\text{NO}_3)_2 \cdot 4\text{H}_2\text{O}$, $\text{CoCl}_2 \cdot 6\text{H}_2\text{O}$ and phenylphosphonic acid ($\text{C}_6\text{H}_5\text{PO}_3\text{H}_2$, 95%) were purchased from Aldrich (Milwaukee, WI) and used without further purification. The water used in all reactions was purified with a Barnstead NANOpure purification system that produced water with an average resistivity of $18 \text{ M}\Omega \text{ cm}$. $\text{Mn}(\text{O}_3\text{PC}_6\text{H}_5)\text{H}_2\text{O}$ and $\text{Co}(\text{O}_3\text{PC}_6\text{H}_5)\text{H}_2\text{O}$ were synthesized by

mixing equimolar amounts of the appropriate metal ion solution with a solution of phenylphosphonic acid (pH adjusted to 5-6 with 0.1 M KOH) both heated to 60°C prior to mixing. The solutions were allowed to stir for two hours at this temperature. For each sample, the precipitate was filtered, washed with water and subsequently with acetone, and then dried under vacuum.

Preparation of $\text{Mn}_x\text{Co}_{1-x}(\text{O}_3\text{PC}_6\text{H}_5)_2\text{H}_2\text{O}$ compounds. The mixed-metal phenylphosphonates $\text{Mn}_x\text{Co}_{1-x}(\text{O}_3\text{PC}_6\text{H}_5)_2\text{H}_2\text{O}$ were prepared in a manner similar to the pure metal phenylphosphonates but with slight modification. In each case, aqueous solutions of the metal salts in the desired molar ratios were heated to 60°C and added to a solution containing a slight excess of phenylphosphonic acid at pH 5-6. The resultant solutions were stirred for only 10 minutes before filtering the precipitate. The products were washed with water and acetone, and finally dried under vacuum. In all cases, the final Mn:Co ratios (determined by atomic absorption) of the solid-state materials were similar, *i.e.* within 10 %, to those of the starting metal salt solutions.

Instrumentation. Atomic absorption (AA) measurements were performed on a Perkin-Elmer Model 3100 atomic absorption spectrometer with a photomultiplier tube detector. For AA analysis, the solid-state samples were dissolved in a 1.0 M HCl solution. X-ray diffraction was done with a step scan (0.02° 2θ /step, 2 sec/step) using a Phillips APD 3720 X-ray powder diffractometer with the Cu K_α line as the source. Electron paramagnetic resonance (EPR) spectra were recorded on a Bruker (Billerica, MA) ER 200D spectrometer modified with a digital signal channel and a digital field controller. Data were collected using a U.S. EPR (Clarksville, MD) SPEC300 data acquisition program and converted to ASCII format using a U.S. EPR (Clarksville, MD)

EPRDAP data analysis program. Magnetization and AC susceptibility measurements were performed using a Quantum Design MPMS SQUID magnetometer. The DC measurements were made with a measuring field of 100 G or 1.0 kG when sweeping the temperature, or were made at 2 K while sweeping the field up to 50 kG. The AC susceptibility measurements used frequencies ranging from 17 Hz to 1.5 kHz and an AC field amplitude of 4.0 G. Additional low frequency (19 Hz) AC susceptibility measurements were performed with a homemade mutual inductance coil of a standard design.¹³⁰ High frequency (14 MHz) studies were conducted in a homemade tank-circuit biased with tunnel diode.^{130,131} For all of the magnetic studies, powder samples were contained in gelcaps or plastic vials, with the exception of the work performed at 14 MHz when the sample was loaded directly into the housing of the coil. The background signals arising from the gelcaps and vials were independently measured and were either negligible or subtracted from the data.

Results and Discussion

Sample Preparations

In order to encourage homogeneous solid solutions of composition $\text{Mn}_x\text{Co}_{1-x}(\text{O}_3\text{PC}_6\text{H}_5)\text{H}_2\text{O}$, and to prevent any annealing into a multi-phased system, samples were quickly precipitated and collected immediately. This procedure resulted in a decreased crystallinity of the solid solutions, relative to what is possible with the pure phases, although it is sufficient for powder XRD analyses and does not appear to influence the magnetic properties. All attempts to prepare mixed-metal samples of high crystallinity by slow growth techniques resulted in the formation of physical mixtures and/or multi-phase materials.

Table 2-1. Concentration of manganese in $\text{Mn}_x\text{Co}_{1-x}(\text{O}_3\text{PC}_6\text{H}_5)_2\cdot\text{H}_2\text{O}$ determined from AA spectroscopy and unit cell parameters determined from the 110, 011 and 030 hkl reflections in the corresponding powder XRD patterns.

Mol % Mn	a±0.01	b±0.01	c±0.01
100	5.73	14.34	4.94
95	5.73	14.34	4.94
82	5.70	14.34	4.92
68	5.68	14.34	4.90
55	5.66	14.34	4.88
35	5.65	14.34	4.88
30	5.64	14.34	4.87
21	5.62	14.34	4.86
19	5.63	14.34	4.85
11	5.61	14.34	4.85
10	5.61	14.34	4.85
0	5.60	14.34	4.83

Structural Characterizations

The relative percentage of manganese and cobalt in the solid solutions was determined from AA analyses (Table 2-1). Although AA spectroscopy gives an average stoichiometry, it cannot provide information about the structural homogeneity of the samples. Therefore, X-ray diffraction was used to determine if the final product consists of single or multiple phases. The structures of the pure manganese and cobalt phenylphosphonate compounds consist of layers of quasi-two-dimensional metal-phosphorus-oxygen sheets that define the *ac* plane, while the organic moieties project between the layers thus defining the *b*-axis (Figure 2-1).^{90,91} These materials are known to crystallize in the same space group, $Pmn2_1$, with slight modifications of the *ac* basal plane spacings.^{90,91} However, the inter-plane distances are almost identical because both compounds contain the same organic phenyl group.

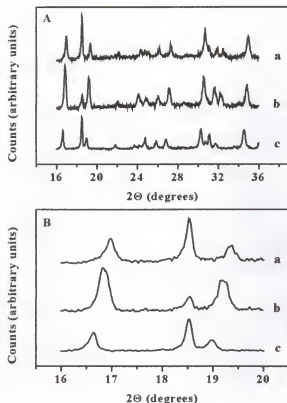


Figure 2-2. A: X-ray powder diffraction patterns of a: $\text{Co}(\text{O}_3\text{PC}_6\text{H}_5)\text{H}_2\text{O}$, b: $\text{Mn}_{0.35}\text{Co}_{0.65}(\text{O}_3\text{PC}_6\text{H}_5)\text{H}_2\text{O}$, c: $\text{Mn}(\text{O}_3\text{PC}_6\text{H}_5)\text{H}_2\text{O}$. B: Expansion showing, from left, 110, 030, 011 *hkl* reflections for a: $\text{Co}(\text{O}_3\text{PC}_6\text{H}_5)\text{H}_2\text{O}$, b: $\text{Mn}_{0.35}\text{Co}_{0.65}(\text{O}_3\text{PC}_6\text{H}_5)\text{H}_2\text{O}$, c: $\text{Mn}(\text{O}_3\text{PC}_6\text{H}_5)\text{H}_2\text{O}$.

Due to the symmetry of the $Pmn2_1$ space group, the 100 and 001 reflections are systematically absent, so the highest order reflections containing in-plane structural information are the 110 and 011. Although both of these reflections contain an inter-plane contribution, this distance remains essentially constant for all compositions. The 110, 030, and 011 reflections conveniently occur consecutively over a small range of 2θ in the X-ray diffractogram, making them a practical series for monitoring variations in the *ac* lattice spacings. The position of the 030 reflection in all samples is an internal reference that confirms that the inter-plane distances do not change as a function of

doping, allowing the 2θ values for the 110 and 011 reflections in the doped materials to be used to determine the in-plane lattice spacings.

Powder XRD patterns for the pure manganese and pure cobalt phenylphosphonates, as well as that of the $\text{Mn}_{0.35}\text{Co}_{0.65}$ sample are shown in Figure 2-2. The similarity of the patterns in Figure 2-2A make it clear that the mixed metal systems are isostructural with the parent compounds. An expansion of the region between 2θ values of $16\text{--}20^\circ$ in Figure 2-2B shows the 110, 030, and 011 reflections for the same three compounds. For the mixed-metal example, discrete 110 and 011 reflections are observed at 2θ values between those of the pure Mn^{2+} or Co^{2+} phases, while the 030 reflection remains the same for all three samples. These observations are consistent with the formation of a single homogeneous solid solution. Similar results were seen for all compositions, and Table 2-1 lists the corresponding a , b , c cell parameters for the pure and doped materials as calculated from the 110, 030, and 011 reflections. The cell edge lengths systematically shift in value as a function of x . The absence of any reflections corresponding to the pure single ion phenylphosphonates in the XRD patterns of the mixed-metal phenylphosphonates, combined with the observation that the detected reflections have 2θ values between those of the two pure compounds, provide convincing evidence that single phase solid solutions have been formed.

Electron Paramagnetic Resonance

Evidence for microscopic homogeneity of the solid solutions comes from EPR. The cobalt phosphonate is EPR silent at X-band, while the manganese analog gives a

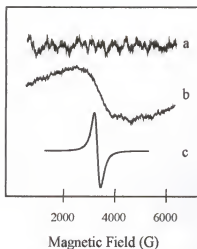


Figure 2-3. Room temperature EPR signals for polycrystalline a: $\text{Co}(\text{O}_3\text{PC}_6\text{H}_5)_2\text{H}_2\text{O}$, b: $\text{Mn}_{0.84}\text{Co}_{0.16}(\text{O}_3\text{PC}_6\text{H}_5)_2\text{H}_2\text{O}$, c: $\text{Mn}(\text{O}_3\text{PC}_6\text{H}_5)_2\text{H}_2\text{O}$.

broad line that is structureless as a result of dipolar interactions (Figure 2-3).¹³² The anisotropy of the EPR line width has previously been used to demonstrate the two-dimensional exchange pathways in the layered manganese phosphonates.^{109,132} As the percentage of Co^{2+} in the solid solution increases, the Mn^{2+} signal broadens (Figure 2-3) reflecting the randomization of the identity of the Mn^{2+} ions nearest neighbors. In the solid solution, there is no signal due to crystallites of pure $\text{Mn}(\text{O}_3\text{PC}_6\text{H}_5)_2\text{H}_2\text{O}$.

Magnetic Properties of $\text{Mn}(\text{O}_3\text{PC}_6\text{H}_5)_2\text{H}_2\text{O}$ and $\text{Co}(\text{O}_3\text{PC}_6\text{H}_5)_2\text{H}_2\text{O}$

The magnetic properties of several manganese and cobalt organophosphonates have been studied previously.^{101,102,104,105,108} The manganese phosphonates undergo a long-range ordering transition to a canted antiferromagnetic state at temperatures ranging from 12 K to 18 K, depending on the identity of the organophosphonate. Pure $\text{Mn}(\text{O}_3\text{PC}_6\text{H}_5)_2\text{H}_2\text{O}$ orders at $T_N \approx 12$ K.¹⁰⁸ The cobalt phosphonates also order antiferromagnetically, and for $\text{Co}(\text{O}_3\text{PC}_6\text{H}_5)_2\text{H}_2\text{O}$, we observe $T_N \approx 4$ K, as we describe later in this section.

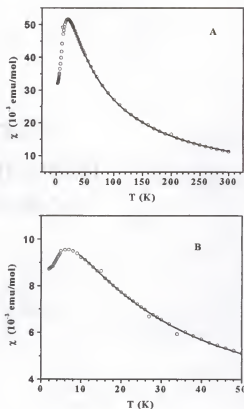


Figure 2-4. A. The temperature dependence of the DC magnetic susceptibility for $\text{Mn}(\text{O}_3\text{PC}_6\text{H}_5)\text{H}_2\text{O}$ after zero field cooling the specimen to 2 K and then measuring in a field of 1 kG. The results of a fit using a $S = 5/2$ Heisenberg high temperature expansion for $T > 20$ K are shown by the solid line with the result $J = -2.27 \pm 0.02$ K, as described in the text. B. The temperature dependence of the DC magnetic susceptibility for $\text{Co}(\text{O}_3\text{PC}_6\text{H}_5)\text{H}_2\text{O}$ after zero-field cooling the sample to 2 K and then measuring in a field of 1 kG. The results of a fit using an $S = 1/2$ Ising high temperature expansion for $T > 9.5$ K are shown by the solid line with the result $J = -2.43 \pm 0.05$ K, as described in the text.

The data in Figure 2-4 show the temperature dependence of the static magnetic susceptibility of the pure Mn and Co materials, acquired by cooling the samples in zero magnetic field and measuring in a DC field of 1 kG. The broad maximum in the susceptibility, χ_{max} , is characteristic of low dimensional antiferromagnetic interactions when short-range order correlations become greater than the thermal fluctuations of the

spins. These short-range correlations are established by magnetic exchange interactions, J , which are typically considered to be limited to nearest neighbor spins. In other words, the Hamiltonian may be written as

$$\mathcal{H} = -J \sum_{nn} \mathbf{S}_i \cdot \mathbf{S}_j \quad [2-1]$$

where \sum_{nn} runs over all pairs of nearest neighbor spins \mathbf{S}_i and \mathbf{S}_j . The susceptibility data for the manganese phosphonate may be fit with a 2D high temperature series expansion¹³³ for a quadratic layer of Heisenberg $S = 5/2$ spins based on eq. [2-1], and the solid line in Figure 2-4A shows the best fit to the data with $J = -2.27 \pm 0.02$ K. The fit was restricted to $T > 20$ K since at lower temperatures the fitting procedure is not valid. In the case of the pure cobalt phenylphosphonate, Eq. [2-1] still describes the simplest interactions for the case of this 2D, $S = 1/2$ Ising system when the spin operators are restricted to their z-components.¹³⁴ The solid line in Figure 2-4B is a fit, for $T > 9.5$ K, to a 2D, $S = 1/2$ Ising high temperature series expansion,¹³⁵ using an exchange constant of $J = -2.43 \pm 0.05$ K. It is noteworthy that the magnetic exchange parameters are very similar in spite of the significantly different spin values and spin dimension.

Previous studies¹⁰⁸ have identified the ordering in $\text{Mn}(\text{O}_3\text{PC}_6\text{H}_5)_2 \cdot \text{H}_2\text{O}$ as a transition to a canted antiferromagnetic state in analogy to other manganese organophosphonates.¹⁰¹ The magnetic moments assume a non-collinear orientation that produces a weak ferromagnetic moment that lies within the plane of the manganese ions. This moment, and hence the transition from the paramagnetic to the canted antiferromagnetic state, can be observed in a difference plot of the magnetization as a

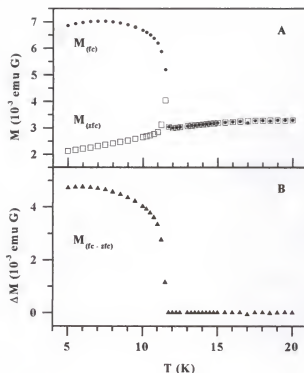


Figure 2-5. A. Field cooled (FC) and zero-field cooled (ZFC) magnetization data of manganese phenylphosphonate are shown as a function of temperature. Both data sets were acquired with a 100 G measuring field. B. The difference between field cooled and zero-field cooled magnetization versus temperature for $\text{Mn}(\text{O}_3\text{PC}_6\text{H}_5)\text{H}_2\text{O}$ measured in a field of 100 G.

function of temperature for experiments performed in field-cooled (fc) and zero-field-cooled (zfc) conditions, $\Delta M_{\text{fc-zfc}}$ (Figure 2-5). The ordering temperature, T_N , may be identified in the M_{fc} data as the temperature where the magnetization begins to deviate from its high temperature paramagnetic behavior, and from Figure 2-5, $T_N = 11.7$ K for $\text{Mn}(\text{O}_3\text{PC}_6\text{H}_5)\text{H}_2\text{O}$. Another parameter, T_N^* , is defined as the temperature at which $\Delta M_{\text{fc-zfc}}$ differs significantly from zero. These two temperatures, $T_N = 11.7$ K and

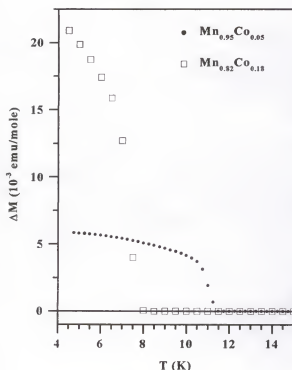


Figure 2-6. The difference between the field cooled and zero field-cooled magnetization, ΔM , is shown as a function of temperature. Typical data from the Mn-rich (*i.e.* $x > 0.25$) samples are shown when the magnetic field, for measuring and field cooling, was 100 G.

$T_N^* = 11.5$ K, are identifiable in Figure 2-5. The value of T_N^* changes as a function of the magnitude of the applied measuring field and as a result, for small values of T_N , it is best to acquire data with a smaller measuring field, typically 50 – 100 G. Due to this dependence upon measuring field, it is important to realize that T_N^* will always be lower than T_N , but T_N^* is nevertheless evidence of an ordered state with a weak ferromagnetic moment. In contrast to the weakly ferromagnetic manganese compound, the pure cobalt

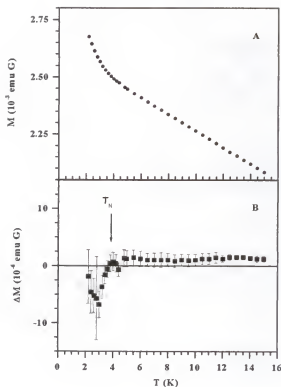


Figure 2-7. A. Field cooled and zero-field cooled DC magnetization for $x = 0.1$. Both data sets were acquired with a 100 G measuring field, and on this scale, the difference between the two data sets is not visually detectable. B. The difference between field cooled and zero-field cooled magnetization from A is shown as a function of temperature. The onset of a negative magnetization occurs at T_N , and this signature is characteristic for all the Co-rich (*i.e.* $x < 0.25$) samples.

compound is antiferromagnetic with $T_N = 3.9$ K, as determined from both DC magnetization and AC susceptibility measurements.

Magnetic Properties of the Solid Solutions

Typical magnetization plots for the solid solutions $\text{Mn}_x\text{Co}_{1-x}(\text{O}_3\text{PC}_6\text{H}_5)\text{H}_2\text{O}$ with $0.25 < x < 1.00$ are shown in Figure 2-6. The ordering temperatures identified in the magnetization vs. temperature plots are consistent, within experimental resolution, with

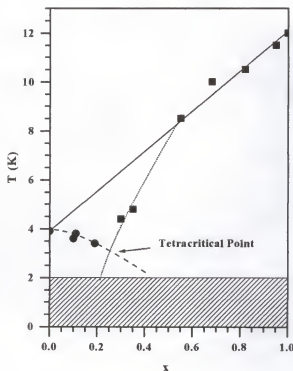


Figure 2-8. The magnetic phase diagram of $Mn_xCo_{1-x}(O_3PC_6H_5)H_2O$ indicating the ordering temperature vs. Mn^{2+} concentration. The phase diagram has a tetracritical point at $x = 0.25$, as described in the text. The present work was restricted to $T > 2$ K. The lines are guides for the eyes and are described in the text.

the temperatures of anomalies in the ac susceptibility studies. Like the pure

$Mn(O_3PC_6H_5)H_2O$, the solid solutions with $x > 0.25$ form canted antiferromagnets in the low temperature state. For $x < 0.25$, the ΔM_{fc-zfc} vs. temperature plots still reveal the ordering temperature, but the magnitude of ΔM_{fc-zfc} is much smaller and negative,

Figure 2-7. This point is discussed further, later in this section. Nonetheless, the

ordering temperatures were confirmed with AC susceptibility measurements, and they are included on Figure 2-8.

The mixed Mn/Co phenylphosphonates can be thought of as magnetically doped pure manganese or pure cobalt lattices with the other metal ion as impurity. Consequently, a reduction of T_N from the pure systems is anticipated. Since the magnetic exchange interactions and lattices are similar, the primary differences are the spin values and the dimension of the spins (*i.e.*, Ising-like or Heisenberg-like). Therefore, the reduction of T_N is not expected to be as strong as it is for the case of doping with diamagnetic spins, and these general tendencies are reflected in the phase diagram in Figure 2-8. In the Mn-rich regime, $T_N(x)$ closely follows a linear function with an $x = 0$ intercept (solid line) at the T_N value obtained for the pure Co material. For $0.25 < x < 0.60$, the perturbation of the magnetic correlations is stronger as the percolation threshold is approached and the reduction of T_N follows a trend qualitatively represented by the dotted line. For the Co-rich samples, there is not sufficient resolution in the identification of T_N to allow a specific x dependence to be identified, so the general trend is sketched by the dashed line. The prediction of a tetracritical point at $x = 0.25$ agrees well with a face-centered square planar lattice containing four nearest neighbors where one spin species dominates the magnetic exchange. In our case, the Mn^{2+} spins dominate the local magnetic environment. Tetracritical points^{120,136} have been observed previously in other doped magnetic systems containing competing magnetic anisotropies.¹³⁷

Search for Spin Glass or Precursor Phases

The assignment of the pure Mn^{2+} material as a canted antiferromagnetic $S = 5/2$ Heisenberg-like system and the pure Co^{2+} system as a quantum antiferromagnetic $S = 1/2$ Ising-like system opens the possibility of forming a spin-frustrated state in a randomly mixed Mn/Co system. In molecular magnetism, similar studies on layered materials have been reported.^{138,139} Thus, bimetallic oxalato layered mixed-metal compounds containing

competing ferro- and antiferromagnetic interactions have been magnetically characterized and in some cases spin glass behavior has been observed.¹⁴⁰ Spin-frustrated systems displaying magnetic properties characteristic of spin glasses have also been observed in doped magnetic materials possessing tetracritical points in their magnetic phase diagrams.^{121,123,141}

Time dependent thermal remnant magnetization studies were performed with two samples, $x = 0.30$ and 0.68 . In one set of experiments, the samples were zero-field cooled from 300 K to 5, 7, and 12 K in three separate runs. The process of cooling from 300 K to the low temperature fixed point required approximately 80 minutes. After equilibrium was established, a field of 1 kG was applied, and the magnetization was monitored for nominally 40 minutes. During this time, the magnetization was observed to relax towards an equilibrium value, and this process was easily fit by a simple exponential function, yielding time constants ranging from 700 to 1100 seconds. In a different measurement, the magnetization relaxation rates of the sample holders were studied and were determined to be negligible. The total change of the signal during the measurement after achieving the equilibrium state, as defined by the thermometer of the instrument, was about 1%. Although these results may be suggestive of behavior associated with a spin glass state, we consider them to be related to the process of cooling the powder samples. A simple cooling model¹⁴² provides a plausible explanation for the measured relaxation rates. It is noteworthy that the same type of behavior was observed for both samples and at all three of the temperatures that were studied. In other words, the experiments covered several of the magnetic phases shown in Figure 2-8, and in every instance, the behavior was always the same.

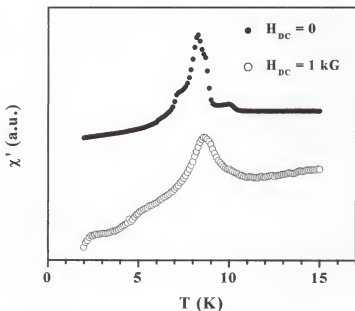


Figure 2-9. The real component of the AC susceptibility for $\text{Mn}_{0.18}\text{Co}_{0.82}(\text{O}_3\text{PC}_6\text{H}_5)\text{H}_2\text{O}$ at 17 Hz and an amplitude of 4 G. The AC susceptibility was studied in an applied field of zero and 1 kG, corresponding to the open and filled circles, respectively. The identification of T_N is consistent with the values determined by DC magnetization techniques. The AC response is understood as arising from the dynamics of the magnetic domains and the powder nature of the specimens, as described in the text.

In a second set of studies, the AC susceptibility of samples was investigated. The temperature dependences of the real component of the AC susceptibility in applied magnetic fields of zero and 1 kG are shown in Figure 2-9 for $x = 0.82$. Our AC studies of all x reproduced, to within experimental resolution, the ordering temperatures seen in the DC magnetization data. However, when no external DC magnetic field was present, new peaks were observed in the AC susceptibility signals, and these features were not present in the DC magnetization data. Upon application of a 1 kG field, these features were suppressed and, therefore, can be attributed to the dynamics of the magnetic domains and the powder nature of the specimens. The temperatures of the transitions as measured by

AC susceptibility did not appear to be frequency dependent from 17 Hz to 1.5 kHz.

Therefore, no spin glass behavior was observed in any of the samples at any temperature $T > 2$ K.

In summary, no evidence of a spin glass state was obtained in our measurements. It is important to note that a spin-flop transition has been observed in pure $\text{Mn}(\text{O}_3\text{PC}_6\text{H}_5)\text{H}_2\text{O}$ in magnetization vs. field studies performed at 2 K,¹⁰⁸ and a similar spin-flop transition is seen for the solid solution with $x = 0.84$. However, no spin-flop signatures were observed for samples with $x < 0.84$, where an increasing intrinsic background arising from competing magnetic spins may have masked the spin-flop transitions. Furthermore, we were particularly curious about the possibility of precursor behavior in the region near the tetracritical point, *i.e.* a region bounded by the solid, dotted, and broken lines in Figure 2-8. However, as discussed at the beginning of this section, no magnetic glassy behavior was observed in this region. Finally, we note that for $x = 0.30$ and 0.35 , our studies down to 2 K did not reveal any anomalies indicative of crossing into an "intermediate" phase.¹²⁰ Naturally, specific heat studies may provide additional information concerning the existence of and the identification of such a phase.

Negative Magnetization in the Cobalt-Rich Samples

For $x < 0.25$, ordering is observed, but the value of $\Delta M_{\text{fc-zfc}}$ is small and negative, Figure 2-7. Features in the ac susceptibility are observed at the same temperatures, so we associate these temperatures with the transition to long-range antiferromagnetic order. The negative magnetization shifts observed for the Co-rich specimens contrasts with the positive magnetization shifts detected for the Mn-rich materials. The phenomenon of negative magnetization has been identified previously in a variety of ferrimagnetic

materials.^{127,128} Naturally with the doped Co-rich specimens, similar arguments may be made if small regions of ferrimagnetic ordered phase are present. However, negative magnetization is also observed in the pure Co material, although it is even weaker than observed in the data shown in Figure 2-7B. Negative magnetization has previously been observed in the canted antiferromagnet,¹⁴³ and the same phenomenon may be responsible for the behavior observed for the cobalt phase ($x < 0.25$).

Conclusion

A new series of mixed metal phenylphosphonate solid solutions, $\text{Mn}_x\text{Co}_{1-x}(\text{O}_3\text{C}_6\text{H}_5)_2\text{H}_2\text{O}$, have been prepared and their magnetic properties investigated. Each composition undergoes long-range magnetic ordering to a canted antiferromagnetic state at temperatures, $T_N \lesssim 12$ K, and a magnetic phase diagram has been constructed based on individual DC and AC susceptibility measurements. For both the Mn^{2+} and Co^{2+} high concentration limits, T_N decreases relative to the pure single ion phosphonates, consistent with what is expected for magnetic ion impurity doping. The phase diagram includes four phases with a tetracritical point at $x = 0.25$ K, indicating a competition between the Heisenberg-like Mn^{2+} and the Ising-like Co^{2+} spins, with the $S = 5/2$ Mn^{2+} dominating the local environment. While prior studies on mixed-metal systems possessing competing spin types have shown evidence for spin-glass behavior, no such state is observed in the $\text{Mn}_x\text{Co}_{1-x}(\text{O}_3\text{C}_6\text{H}_5)_2\text{H}_2\text{O}$ solid solutions.

CHAPTER 3

STRUCTURE CHARACTERIZATION OF METAL PHOSPHONATE LANGMUIR-BLODGETT FILMS BY GRAZING INCIDENT X-RAY DIFFRACTION

Introduction

We have recently described the preparation of a series of metal phosphonate containing Langmuir-Blodgett films.^{109-111,113-119,132,144,145} These films, modeled after known layered organic/inorganic solids, demonstrate that it is feasible to incorporate an inorganic extended solid-state network into the hydrophilic region of a Langmuir-Blodgett bilayer assembly. Examples prepared to date include several divalent^{111,113,114,119,132,145} and trivalent metal phosphonate networks^{113,114,117} formed with straight chain alkylphosphonates as well as with organophosphonate amphiphiles containing azobenzene¹¹⁷ and tetrathiafulvalene¹¹⁹ functional groups. The inorganic lattice greatly enhances the stability of the resulting LB films¹¹⁸ and enables introduction of traditionally solid-state properties such as magnetism into these thin film materials.^{109,132,145} In addition, by employing functional phosphonic acids, LB films that combine properties of organic and inorganic assemblies have been prepared.^{117,119}

To date, direct structural characterization of the inorganic component of these metal phosphonate films is lacking. Analysis has generally relied on comparisons of spectroscopic and magnetic properties of the films with those observed for similar solid-state analogs. These comparisons have offered convincing, but nevertheless indirect, evidence that the inorganic lattices formed in the LB films are isostructural with the

known solids. We report here direct structural characterization of the inorganic lattices in a series of these metal phosphonate containing LB films using grazing incidence X-ray diffraction (GIXD). The results confirm the earlier conclusions that the inorganic lattice that forms in these LB films is isostructural with the solid-state analogues.

Experimental Section

The 16-bilayer manganese octadecylphosphonate¹⁴⁵ (**MnOPA**), 16-bilayer lanthanum octadecylphosphonate¹¹⁴ (**LaOPA**), and 15-bilayer manganese (4-(4'-tetradecyloxyphenyldiazenyl)phenyl)butylphosphonate¹¹⁷ (**MnA4**) LB films on glass slides were prepared as previously described. A "bilayer" is comprised of head-to-head layers of the phosphonate amphiphile sandwiching one metal ion layer.

The grazing incident X-ray diffraction experiments were conducted at the Materials Research Collaborative Access Team (MRCAT) beamline at sector 10 of the Advanced Photon Source, Argonne National Laboratory, Argonne, Illinois.⁷⁶ The beamline is equipped with an undulator insertion device, a double silicon crystal monochromator, harmonic rejection mirror, and a NaI scintillation counter mounted on an eight-circle Huber goniometer.¹⁴⁶ The sample was mounted in the center of the goniometer and aligned to make the $\lambda = 1.254 \text{ \AA}$ X-rays incident on the sample at an angle of 1.8 mrad. The evanescent wave produced at this low incidence angle allows for enhanced surface sensitivity. The beam was 2 mm wide by 0.2 mm high and irradiated an approximately 50 mm strip along the sample surface. The scattered X-rays were detected by scanning the scintillation counter through a plane parallel to the sample surface. Bragg rod profiles were obtained by scanning over the peaks of interest in the xy plane with successive steps in the z direction (perpendicular to the sample surface). The

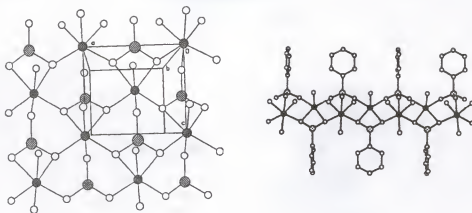


Figure 3-1 In-plane and cross-sectional view of $\text{Mn}(\text{O}_3\text{PC}_6\text{H}_5)\text{H}_2\text{O}$. Crystallographic data are taken from reference 16. Key: oxygen, small open circles; manganese, crosshatched circles; phosphorus, diagonal-hatched circles (phosphorus atoms above and below the plane are distinguished by hatches with different directions).

scattered X-rays were collimated through a set of Soller slits prior to detection giving an instrumental resolution in Q_{xy} of 0.0015 \AA^{-1} , and Q_z of 0.01 \AA^{-1} where

$$Q_{xy} = (4\pi/\lambda)\sin\theta_{xy} \text{ and } Q_z = (2\pi/\lambda)\sin\theta_z.$$

Results and Discussion

Manganese Octadecylphosphonate Film

The structural prototype of the $\text{Mn}(\text{O}_3\text{PR})\text{H}_2\text{O}$ manganese phosphonates is the phenyl analog, $\text{Mn}(\text{O}_3\text{PC}_6\text{H}_5)\text{H}_2\text{O}$, the structure of which was determined by Cao et al and is shown in Figure 3-1.⁹¹ The solids crystallize in the $Pmm2_1$ space group, and the phenylphosphonate has unit cell parameters $a = 5.734$, $b = 14.33$, and $c = 4.945$. The lamellar material consists of two-dimensional manganese-oxygen networks in the ac plane separated in the b direction by the phenyl groups of the phenylphosphonate ligands. If the in-plane manganese-oxygen network is considered alone, it can be described with a

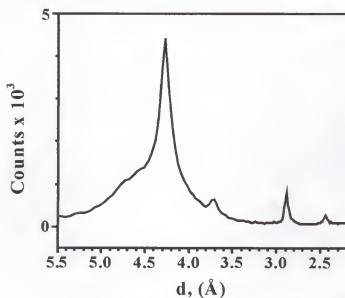


Figure 2. The grazing incidence X-ray diffraction pattern obtained on a 16-bilayer sample of **MnOPA**.

face-centered rectangle unit cell with edges $a = 5.734 \text{ \AA}$ and $b = 4.945 \text{ \AA}$ (in the two-dimensional cell, the b axis corresponds to the c axis in the $Pmm2_1$ space group).

The background corrected GIXD pattern obtained from the **MnOPA** LB film is shown in Figure 3-2. The pattern consists of four distinct diffraction peaks corresponding to lattice spacings of 4.27, 3.71, 2.88, and 2.44 \AA . The latter three peaks are due to scattering from the manganese-oxygen network of the inorganic lattice and can be indexed to a face-centered rectangular cell with Miller indices of (1 1), (2 0), and (0 2), respectively, corresponding to unit cell parameters of $a = 5.76 \text{ \AA}$ and $b = 4.88 \text{ \AA}$. The (1 0) and (0 1) reflections are absent due to the centered cell. The indexed diffraction pattern of the LB film agrees very well with the unit cell for the solid-state manganese phenylphosphonate verifying that the inorganic network formed in the LB film is isostructural with the analogous solids. Analysis of the peak width for the isolated

(0 2) peak by application of the Scherrer equation¹⁴⁷ yields an average structural coherence length of ~ 180 Å.

The intense broad peak in the diffraction pattern at a spacing of 4.27 Å is typical of inter-alkyl chain distances.^{78,79} The presence of a single diffraction peak is usually interpreted as hexagonal close packing of freestanding chains. This packing motif is unlikely in **MnOPA** due to the structural constraints of the underlying inorganic network that yields an average cross-sectional area per alkyl chain of 28 Å². Interlayer spacings determined from previous X-ray diffraction data indicate a tilt angle of approximately 30°, and Bragg rod scans of the GIXD peak confirm this assessment. The absence of the additional diffraction peaks that are expected from a lower symmetry cell is likely due to a small coherence length of the alkyl packing, resulting from significant disorder in the organic network induced by the lattice mismatch between the rigid inorganic layer and the alkyl chain packing. A similar situation has been observed for alkyl chains tethered to a rigid polymer backbone.¹⁴⁸

Azobenzene Derivatized Manganese Phosphonate Film

The GIXD pattern for a 15-bilayer film of **MnA4** is shown in Figure 3-2. As in **MnOPA**, the pattern shows the expected peaks corresponding to the (2 0) and (0 2) Bragg planes for the manganese phosphonate lattice at spacings of 2.88 Å and 2.44 Å. The (1 1) peak expected at 3.71 Å is obscured in **MnA4** by the strong scattering from the organic groups. The spacings for the inorganic lattice yield the same centered rectangular cell, $a = 5.76$ Å and $b = 4.88$ Å, observed for the **MnOPA** film, verifying that the same inorganic network forms in each case.

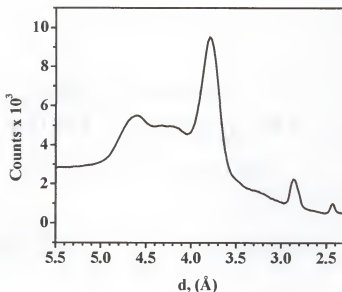


Figure 3-3. The grazing incidence X-ray diffraction pattern obtained on a 15-bilayer sample of **MnA4**.

As expected, the packing of the organic groups is different in the two manganese phosphonate films. In contrast to the intense reflection at 4.27 Å in **MnOPA**, the **MnA4** film has a strong reflection at 3.79 Å and a weaker reflection at 4.59 Å. Previous investigations into the structure of azobenzene-containing alkane thiol monolayers on gold by Caldwell *et al.* suggested that the azobenzene groups, when tethered to the surface with flexible alkyl segments, can aggregate into tightly packed islands forming a herringbone motif.⁹⁴ Thus, the azobenzene unit, although not completely independent of the Au(111) surface, strongly influences the overall packing arrangement.⁹⁴ In the case of the SAMs on gold, the azobenzene groups were proposed to pack with hexagonal symmetry with an intermolecular separation of 4.5 Å, which gave rise to a single diffraction peak at 3.9 Å. The presence of two diffraction peaks at 4.59 Å and 3.79 Å in **MnA4** suggests a deviation from hexagonal symmetry and therefore a different packing

arrangement of the azobenzene groups than was observed for the SAMs on gold. This variation likely results from a combination of the rectangular symmetry of the underlying manganese phosphonate lattice and the shorter alkyl tether in **MnA4** preventing a high degree of aggregation. A unit cell for the organic network can be assigned by assuming the azobenzenes tilt by 22° along the direction parallel to the manganese face diagonal. This arrangement would result in an oblique unit cell of dimensions $a = 7.0 \text{ \AA}$ and $b = 5.8 \text{ \AA}$ and $\gamma = 140^\circ$ for which the reflections at 4.59 \AA , and 3.79 \AA can then be assigned to the $(1\ 0)_{\text{org}}$ and $(0\ 1)_{\text{org}}$ Bragg planes, respectively (the subscript *org* is used to differentiate the organic network when it is considered independently from the inorganic network). The $(2\ -2)_{\text{org}}$ reflection for the organic lattice is predicted at 2.88 \AA , commensurate with the $(2\ 0)$ reflection of the parent inorganic network. This peak may contain intensity from both networks. Support for this assignment comes from the peak width, which is larger than either the related 2.44 \AA peak that arises from the inorganic network or the corresponding peak from Figure 3-1 for **MnOPA**. This arrangement of the azobenzene groups would also lead to significant π -interactions perpendicular to the $(0\ 1)_{\text{org}}$ Bragg plane and π -stacking is supported by UV-Vis spectroscopy, reported previously.¹¹⁷

Lanthanum Octadecylphosphonate Film

Trivalent lanthanum phosphonates are also known to form layered structures in the solid state, now consisting of two-dimensional oxygen-bridged La^{3+} networks separated by the organic substituents of the phosphonate group. The GIXD pattern for the **LaOPA** LB film is compared to the diffraction pattern obtained for a powdered sample of lanthanum butylphosphonate in Figure 3-4. The similarities in the diffraction patterns of the two materials indicate that the inorganic network formed in the LB film

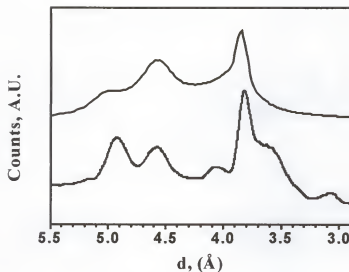


Figure 3-4. The grazing incidence X-ray diffraction pattern obtained on (top) a 16-bilayer sample of **LaOPA** compared to a X-ray powder diffraction pattern of (bottom) lanthanum butylphosphonate.

is isostructural with the shorter chain solid-state analog. The trivalent lanthanum ion requires two phosphonates (one monobasic and one dibasic) to preserve electric neutrality, resulting in a higher density of alkyl chain packing than is observed for the manganese phosphonates. Bragg rod scans of the GIXD peaks and interlayer spacings obtained from conventional X-ray diffraction indicate an absence of any significant tilt angle in the alkyl chains. As a result, the organic and inorganic networks lie on the same two-dimensional lattice, and the observed diffraction peaks are a composite of scattering from the inorganic extended network and the alkyl chain molecular network. The entire pattern can be indexed to an oblique cell with $a = 12.05 \text{ \AA}$, $b = 10.55 \text{ \AA}$, and $\gamma = 72^\circ$. The assigned unit cell is essentially a $1.5 \times a$, $2 \times b$ super cell of the in-plane cell derived from X-ray powder diffraction studies of lanthanum methylphosphonate.¹⁴⁹ More complete structures of lanthanum benzylphosphonate and lanthanum phenylphosphonate

Table 1. The calculated and observed lattice (d) spacings, in Å, for the proposed lanthanum octadecylphosphonate unit cell, $a = 12.05$ Å, $b = 10.55$ Å, and $\gamma = 72^\circ$.

(h,k)	calc	obs
(0,2)	5.02	5.0
(2,2)	4.53	4.57
(3,0)	3.82	3.85
(3,2)	3.63	3.68
(3,-2)	2.67	2.67
(2,-3)	2.56	2.56
(-2,4)	2.07	2.11
(4,-3)	1.90	1.98

have been determined,¹⁵⁰ however, the methyl derivative was chosen as the structural analogue to the LB film since both are alkylphosphonates. The methylphosphonate diffracts in a triclinic space group with $a = 5.398$, $b = 8.168$, $c = 10.162$, $\alpha = 73.76^\circ$, $\beta = 83.89^\circ$, and $\gamma = 73.5^\circ$.¹⁴⁹ The in-plane lanthanum-oxygen network of an individual layer can be assigned two-dimensional parameters based on this structure of $a = 5.398$ Å, $b = 8.168$ Å, $\gamma = 73.5^\circ$ with two lanthanum ions per unit cell. The larger unit cell for the LB film is necessary to make the organic and inorganic sublattices commensurate. The calculated lattice spacings are compared to the experimental spacings in Table 3-1. This cell contains three lanthanum ions and six phosphonate groups and provides an average molecular cross-sectional area per phosphonate group of approximately 20 Å^2 , consistent with a close-packed, upright organization of the alkyl chains.

Conclusions

The GIXD experiments on a series of Mn^{2+} and La^{3+} metal phosphonate LB films prove that the inorganic networks in these films are isostructural with their known solid-state analogs, confirming earlier assignments that were based on spectroscopic data. The three examples described here make up an interesting series. The **LaODP** film provides an example where the inorganic and organic networks can be described with the same two-dimensional unit cells. In the **MnA4** film, the two networks are commensurate, but best described with independent cells. And finally, the packing of the organic network in the **MnODP** film appears to be incommensurate with the inorganic network. These observations reinforce the idea that the metal phosphonate extended lattice will form regardless of the organic groups, as long as the space requirements of the metal ion lattice can be met. The larger energy associated with the metal/ligand interactions determines the structure and the area available to the organic groups.

CHAPTER 4

FORMATION OF AN EXTENDED TWO-DIMENSIONAL COORDINATE COVALENT SQUARE GRID NETWORK AT THE AIR WATER INTERFACE

Introduction

Many advances in the pursuit of nanoscale objects make use of supermolecular assembly, the synthesis of larger structures from molecular building blocks.¹ Inspired by biological self-assembly, much supermolecular chemistry holds structures together with directed, non-covalent interactions such as hydrogen bonding, van der Waals, electrostatic, and π -stacking forces.^{2,4} However, bonding is not restricted to weak interactions, and the directional properties of coordinate covalent bonding have also lead to many interesting structures.^{2,4-13}

Among the motivations for the pursuit of nanometer scale objects is the need for electronics architectures that are beyond the scope of present-day lithographic technologies.^{151,152} Such architectures will require both nanometer scale device components and infrastructures such as wires, insulation, and shielding that can service or interface with these devices at the nanometer scale.² In addition to electronics and information storage, other applications of nanoscale architectures include catalysis and separations, while nanoscale objects also have tremendous potential as molecular level probes and transducers for chemical recognition sensing.¹⁵²

Many of these applications are likely to require positioning the structures at surfaces. For example, the electronics architectures mentioned above will have to be

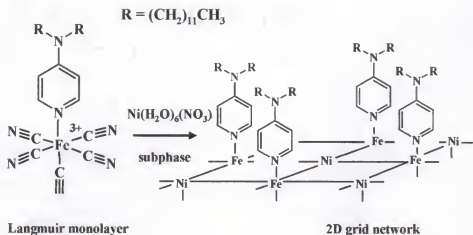
fabricated onto a support. Two-dimensional (2D) grid structures have been proposed as separations media,¹⁵³⁻¹⁵⁶ which will require their positioning at an interface between phases. Interfaces may also play a role in the “manufacture” of supermolecular structures, providing a way of directing interactions by orienting molecules at the surface for subsequent reaction. Therefore, there is a significant need to investigate the application of supermolecular assembly processes at interfaces.⁵⁷⁻⁶⁵ With a growing understanding of how to synthesize supermolecular objects, we can now begin to study how the requirements of such assembly processes can be adapted for fabrication at interfaces. Included in this goal is the need to investigate ways to use the interface itself as a structure-directing feature in the assembly of supermolecular architectures.

Air/liquid interfaces are often used to direct assembly processes, and a careful understanding of these processes is now possible largely as a result of surface sensitive characterization methods, including grazing incidence X-ray diffraction.⁸⁰ Traditional Langmuir monolayers can form two-dimensional molecular crystals,^{66,79,80,157} or can selectively bind molecules or ions from the subphase to produce multicomponent assemblies.^{80,158-160} Langmuir monolayers are also used to induce the heterogeneous nucleation of three-dimensional crystals, where chemical or stereochemical features of the monolayer can direct the morphology, orientation, or chemical identity of the product crystals.¹⁶¹⁻¹⁶³ Supermolecular objects have also been prepared in situ at the air/water interface.⁸⁰ For example, the 2x2 and 3x3 metal ion molecular grids first described by Lehn et al.¹⁶⁴⁻¹⁶⁶ been formed at the air/water interface by reaction of Langmuir monolayers of the linear multidentate ligands with aqueous metal ions.^{62,63} These and other examples are included in a recent comprehensive review by Kuzmenko et al.⁸⁰

Less common are extended two-dimensional covalent grid networks. The best-described examples are those of Michl and coworkers who use the principles of modular chemistry to prepare surface-anchored two-dimensional covalent networks.^{153-155,167,168}

As part of our investigation of these issues, this article describes the assembly of a two-dimensional nickel-iron-cyanide grid network at the air/water interface. Numerous solid-state compounds based on bridging cyanides are known^{19,21,22,33,38,51,52,169-172} with the prototype being Prussian blue. Recent interest in these compounds stems from the cyanide ligand's ability to efficiently mediate magnetic exchange, and many new mixed-metal Prussian blue-like structures have been developed with fascinating magnetic properties.^{51,52,169,173,174} Structures with one- and two-dimensional coordinate covalent networks are also known,^{33,170,171} and metal cyanide complexes have been used as building blocks in the preparation of "zero-dimensional" clusters.^{19,21,22,172} In all cases, the structure directing elements are the well-defined bond angles of the transition metal complexes and the linear bridging cyanide ligands.

Our approach for assembly at an interface is outlined in Scheme 4-1. The target is a square grid nickel-iron-cyanide network that arises from the 90° bond angles around the starting iron cyanide complex. The product is a single monolayer of a two-dimensional square grid because the amphiphilic dialkylaminopyridine ligand confines the iron complex to the interface, which then directs the condensation reaction within the plane of the water surface. In the absence of the interface, the pentacyanoferrate (3+) starting complex is capable of forming bridges that lead to geometries other than a square grid, and when the reaction is carried out in solution, only amorphous products are observed.



Scheme 4-1. Assembly of a two-dimensional square grid network at the air/water interface.

The interface facilitates bridging in the equatorial plane of the amphiphilic complex, and therefore plays an important role in controlling the final structure.

A potential obstacle to confining reactants to an interface is that reactivity can be limited by restricted diffusion.¹⁵⁶ A gas/liquid interface minimizes this problem, allowing studies to focus on the structure-directing elements of the reactants and surface. In addition, structures formed at the air/water interface can be transferred from the water surface to solid supports using standard Langmuir-Blodgett film methods. The transferred films allow for a more thorough measurement of the structural and physical properties of the interface-formed networks. The condensation reaction outlined in Scheme 4-1 is followed at the air/water interface with surface pressure measurements and with Brewster angle microscopy (BAM), and the structure of the resulting nickel-iron-cyanide network is confirmed in transferred films with optical and infrared spectroscopy, X-ray absorption fine structure (XAFS), grazing incidence X-ray diffraction (GIXD) and magnetization measurements.

Experimental Section

Synthesis

Materials. Unless otherwise indicated, all reagents were purchased from Aldrich (Milwaukee, WI) or Fisher Scientific (Pittsburgh, PA) and used without further purification. The 4-aminopyridine was recrystallized from water prior to use.

Instrumentation. All NMR spectra were obtained on a Varian VXR-300 spectrometer. The characteristic solvent peaks were used as reference values. Elemental analyses and mass spectrometry analyses were performed by the University of Florida Spectroscopic Services laboratory, where high-resolution mass spectra were collected on a MAT 95Q, Finnigan MAT (San Jose, CA). Melting points were obtained on a Thomas-Hoover Capillary melting point apparatus and are uncorrected. UV-Vis spectra were obtained on a Hewlett-Packard 8452A diode array spectrophotometer. IR spectra as KBr pellets were recorded on a Mattson Instruments (Madison, WI) Research Series-1 FTIR spectrometer with a deuterated triglycine sulfate (DTGS) detector.

N-methyl-4-didodecylaminopyridinium iodide (1). A solution of 3.54 g (0.015 mol) N-methyl-4-aminopyridinium iodide¹⁷⁵ and 9.37 g (0.0375 mol) of 1-bromododecane in acetonitrile (75 mL) was refluxed over 5.5 g K₂CO₃ (0.04 mol) for three days. The acetonitrile was removed and the organic materials dissolved in chloroform and filtered. The chloroform was removed under reduced pressure and 20 mL of diethyl ether was added to the orange oil that remained. Addition of the ether solution to 150 mL of pentane with vigorous stirring precipitated the product. The solid was filtered and washed well with diethyl ether and dried under vacuum (7.8 g, 91%) ¹H NMR (CD₃Cl), ppm: 8.45, d, 2H; 6.79, d, 2H; 4.11, s, 3H; 3.37, t, 4H; 1.54, m, 4H; 1.19-

1.25, m, 36H; 0.80, t, 6H. Calcd for $C_{30}H_{57}N_2I$: C, 62.92; H, 10.03; N, 4.89. Found: C, 63.25; H, 10.64; N, 4.89. Melting point: 99-101 °C. MS (445).

4-didodecylaminopyridine (2). Demethylation of **1** was accomplished in a manner analogous to a previously reported procedure for the demethylation of pyridinium salts.¹⁷⁶ A stirred mixture of 7.5 g of **1** and 40 g of pyridine hydrochloride were refluxed under nitrogen in the absence of solvent. After 24 hours the mixture was cooled and 75 mL of water was added to dissolve the excess pyridine hydrochloride. The crude product was filtered off and redissolved in 100 mL chloroform. The chloroform solution was extracted three times with 50 mL portions of concentrated ammonium hydroxide and dried over anhydrous $MgSO_4$ before removal of the solvent under reduced pressure. Acetonitrile (100 mL) was added to the oil that remained and the mixture was vigorously stirred in an ice bath. The precipitated solid was redissolved in diethyl ether (100 mL), treated with 200 mg of activated carbon and filtered through Celite. The ether filtrate was mixed with 80 mL of acetonitrile and concentrated under a stream of N_2 to precipitate the pure product as beige solid. The solid was washed with acetonitrile and dried under vacuum (3.9 g, 70%). 1H NMR (CD_3Cl), ppm: 8.16, d, 2H; 6.41, d, 2H; 3.25, t, 4H; 1.57, m, 4H; 1.26-1.31, m, 36H; 0.88, t, 6H. Calcd for $C_{29}H_{54}N_2$: C, 80.86; H, 12.64; N, 6.50. Found: C, 81.14; H, 12.28; N, 6.58. mp 54-56 °C MS (431 (H^+)).

Bis(tetramethylammonium) pentacyano(4-didodecylaminopyridine)-ferrate(III) · 6H₂O (3). The preparation of the amphiphilic pentacyanoferrate complex was adapted from a previously reported procedure for the preparation of disodium pentacyano(4-octadecylamino-pyridine)ferrate(III).¹⁷⁷ To a solution of 1.9 g (0.0044 mol) of **2** in methanol (50 mL) at 40 °C was added 0.40 g (0.0015 mol)

$\text{Na}_3[\text{Fe}(\text{CN})_5\text{NH}_3] \cdot x\text{H}_2\text{O}$. The suspension was stirred for 12 hours in air yielding a dark purple solution. The methanol was concentrated at room temperature under reduced pressure to a volume of 10 mL and 40 mL of chloroform added. The insoluble iron salts were filtered off through Celite and the solvents removed. The product was dissolved in 50 mL methanol and precipitated by the addition of AgBF_4 (0.003 mol) in 25 mL methanol. The solid was filtered, washed with methanol and ether, and transferred to a methanol solution of tetramethyl ammonium bromide (0.003 mol). The mixture was stirred vigorously for four hours and then filtered to remove the AgBr . The violet filtrate was concentrated at room temperature to a few milliliters and added to 75 mL acetonitrile. Concentration of the acetonitrile under a stream of nitrogen, followed by the addition of several volumes of acetone precipitated the complex as a violet powder, which turns blue upon hydration. The solid was dried under vacuum in a desiccator over P_2O_5 (0.412 g, 35 %). IR (KBr pellet): $\nu_{\text{C-N}}(\text{cm}^{-1})$ 2126, 2116. Calcd for $\text{C}_{42}\text{H}_{90}\text{N}_9\text{O}_6\text{Fe}$: C, 57.78; H, 10.4; N, 14.44. Found: C, 57.30; H, 10.76; N, 14.68.

Films

Materials. Unless noted, all reagents were used as received.

Substrate preparation. Single-crystal (100) silicon wafers, purchased from Semiconductor Processing Co. (Boston, MA), were used as deposition substrates for X-ray photoelectron spectroscopy (XPS). X-ray diffraction, FT-IR, UV-Vis, and GIXD samples were prepared on petrographic slides that were purchased from Buehler Ltd (Lake Bluff, IL). Samples for SQUID and XAFS investigations were prepared on Mylar (Dupont) substrates cleaned prior to use with absolute ethanol. The silicon, glass, and quartz substrates were cleaned using the RCA procedure¹⁷⁸ and dried under nitrogen.

All substrate surfaces were made hydrophobic by deposition of a monolayer of OTS.^{179,180}

Instrumentation. The LB films were prepared by using a KSV Instruments 5000 trough modified to operate with double barriers. The surface pressure was measured with a filter paper Wilhelmy plate suspended from a KSV microbalance. Subphase solutions were prepared from 17.8-18.1 M Ω cm water delivered with a Barnstead Epure system. The XPS spectra were obtained on a Perkin-Elmer (Eden Prairie, MN) PHI 5000 series spectrometer using the Mg K α line source at 1253.6 eV. Typical operating pressure was 4×10^{-10} bar. X-ray diffraction was performed with a Philips APD 3720 X-ray powder diffractometer with the Cu K α line, $\lambda = 1.54$ Å. Magnetization measurements were performed on a Quantum Design MPMS SQUID magnetometer.

GIXD and XAFS experiments using synchrotron radiation were performed at the Advanced Photon Source, Argonne, IL, at the Materials Research Collaborative Access Team beamline (sector 10). The XAFS spectra of LB films transferred to Mylar were recorded in fluorescence mode using a Lytle detector. The sample film was oriented at 45 degrees to the incident beam and the detector at 90 degrees relative to the incident beam. Energy calibration was accomplished by simultaneously recording transmission XAFS spectra through the appropriate metal foil positioned behind the LB film sample. Transmission intensity was measured using an ion chamber detector charged with the appropriate air/N₂ ratio to give a linear response over the scanned energy range. The sample used for XAFS was 100 bilayers. XAFS scans were taken over both the Fe and Ni edges from 150 eV before the edge step to 1 keV beyond the edge in separate runs for each edge. Data analysis was performed using the Winxas program.⁸⁴ Background

subtraction and normalization to the edge step was done with a linear fit to the pre-edge region and a second order fit to the post edge region. The atomic absorption correction was done on the k^3 weighted data using a cubic spline function. Fourier transforms of the k^3 -weighted data were done in combination with a Bessel window function. No smoothing functions or Fourier filters were applied to the data (for an overview of the data analysis see Chapter 1) The GIXD scans were performed on LB films transferred to glass slides. The sample was positioned in the center of an 8-circle Huber goniometer and oriented at an angle of 0.13 degrees relative to the incident beam. The incident beam was collimated to 200 microns high by 1500 microns wide and tuned to a wavelength of 1.254 Å. Diffracted intensity in the xy plane was measured using a NaI scintillation counter mounted on the Huber goniometer. The diffracted signal was collimated prior to the detector using Soller slits giving an experimental resolution on the order of 0.015 Å⁻¹.

Film preparation. The amphiphilic iron complex **3** was spread onto the water surface from a chloroform solution. All multilayer films of the nickel-iron-cyanide network were transferred as Y-type films onto hydrophobic substrates at a surface pressure of 25 mN/m over a subphase 1 g/L in Ni(NO₃) at ambient temperature. The average transfer ratios for both the upstroke and downstroke were 0.85.

Results

Langmuir Monolayers and LB Film Transfer

The amphiphilic iron complex **3** forms a well-behaved monolayer on the water surface. Brewster angle microscopy indicates the amphiphile is in a liquid expanded state at zero surface pressure at room temperature. Compression of the monolayer at room temperature produces the surface pressure versus area isotherm shown in Figure 4-1.

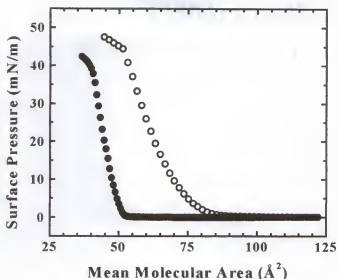


Figure 4-1. Room temperature surface pressure vs. mean molecular area isotherms for complex **3** over pure water (open circles) and over a 1 g/L Ni(NO₃)₂ (filled circles).

The complex is slightly soluble on pure water and a creep of approximately 15 Å²/molecule/hour is seen at a surface pressure of 1 mN/m, Figure 4-2.

The behavior of **3** over a subphase containing Ni²⁺ is markedly different from that over pure water. Brewster angle microscopy indicates that the monolayer is in a condensed phase at zero surface pressure when the subphase contains Ni²⁺. Evidence for a condensed phase at zero surface pressure is also given by the isotherm shown in Figure 4-1. The mean molecular area of 52 Å² at the onset of pressure for the complex over a Ni²⁺ subphase is nearly identical to the mean molecular area at collapse of the complex over pure water. Additionally, the slope of the isotherm is steeper when **3** is compressed over a Ni²⁺ subphase. As will be demonstrated, this behavior results from a condensation reaction between the ferric amphiphile and the aqueous nickel ions.

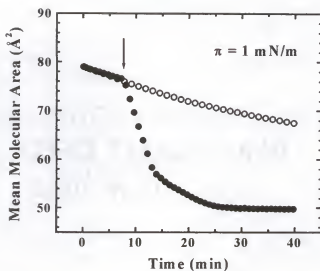


Figure 4-2. The change in mean molecular area versus time at a surface pressure (π) of 1 mN/m for complex **3** over pure water (open circles), and over pure water with subsequent injection of a $\text{Ni}(\text{NO}_3)_2$ solution (at the time indicated by the arrow) under the monolayer (filled circles). Condensation of the monolayer occurs immediately after injection of the Ni^{2+} solution.

The reaction at the air/water interface was also detected by monitoring the change in mean molecular area (MMA) versus time at a constant surface pressure as shown in Figure 4-2. A monolayer of **3** was first compressed over pure water to a pressure of 1 mN/m. A slow and linear creep is seen in the film due to the slight solubility of **3**. When 10 mL of a solution of $\text{Ni}(\text{NO}_3)_2 \cdot 6\text{H}_2\text{O}$ (at a concentration to give a final subphase concentration of 1 mM Ni^{2+}) is then injected under the monolayer, a rapid drop in the MMA is seen. The MMA eventually stabilizes at a value of 50 \AA^2 , which after correction for the initial creep of *ca.* $2\text{-}3 \text{ \AA}^2$, agrees well with the 52 \AA^2 seen at 1 mN/m in the compression isotherm performed over Ni^{2+} , shown in Figure 4-2.

To further characterize the product of the condensation reaction occurring on the water surface, the networks were transferred to various supports by the Langmuir-

Blodgett (LB) technique. The nickel-iron-cyanide network transferred well as Y-type films from a subphase containing 1 g/L $\text{Ni}(\text{NO}_3)_2$ at a surface pressure of 25 mN/m giving an average transfer ratio of 85% (due to the rigid nature of the film) on both the up strokes and the down strokes on all substrates used. In contrast, in the absence of Ni^{2+} , amphiphile **3** transfers on the down stroke, but washes off on the up stroke.

Spectroscopic Analyses

Pentacyanoferrate(III) complexes coordinated to a 4-aminopyridine ligand display an intense ligand to metal charge transfer band between 500 and 700 nm, depending on the identity of the 4-aminopyridine derivative and the nature of the solvent.^{181,182} This charge transfer band is also observed in the transferred films containing the nickel-iron-cyanide network. The intensity of the charge transfer band increases linearly with the number of transferred bilayer and demonstrates a reproducible transfer of the network from one bilayer to the next. In addition, the presence of this band in the LB films confirms that the integrity of the iron complex is preserved over the course of film formation.

Evidence that nickel is incorporated in the transferred film is found by XPS. A survey scan of a monolayer transferred on the upstroke onto a clean silicon wafer shows both Fe ($2p_1$ and $2p_3$) and Ni ($2p_1$ and $2p_3$) peaks. Analysis of the integrated areas of the XPS multiplex scans using a take-off angle of 80 degrees and taking into account differences in photoelectron escape depths¹⁸³⁻¹⁸⁵ for both sets of peaks yields an Fe:Ni ratio of 1:1 +/- 10%. This ratio is expected if the Ni^{2+} ions are incorporated into a face-centered square grid assembly as depicted in Scheme 4-1.

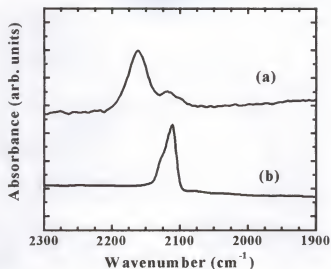


Figure 4-3. FT-IR absorption spectra of the C-N stretching region for (a) a monolayer film of the nickel-iron-cyanide grid network transferred to a silicon ATR crystal, and (b) a KBr pellet of pure **3**.

Confirmation of cyanide bridging in the monolayer networks is found by comparing the C-N IR stretches in the LB film and a KBr pellet of pure **3** (Figure 4-3). In **3**, the cyanide-stretching region shows a strong band at 2111 cm^{-1} and a shoulder at 2126 cm^{-1} . These bands are in agreement with the pseudo C_{4v} symmetry of the complex. The FT-IR spectrum of a monolayer of **3** reacted with Ni^{2+} and transferred to a silicon ATR crystal shows a dominant cyanide stretching band at 2162 cm^{-1} and a weaker band at 2118 cm^{-1} . This shift to higher energy is typical when cyanide assumes a bridging mode.⁷¹⁻⁷³

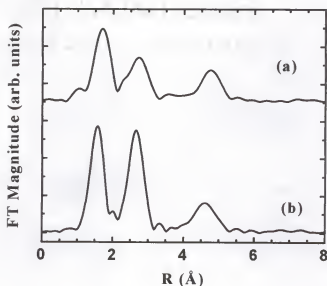


Figure 4-4. Magnitude of the Fourier transforms (FT) of the (a) nickel edge and (b) iron edge k_3 -weighted XAFS for a 100-bilayer sample of the nickel-iron-cyanide grid network transferred to Mylar. The “R-axis” has not been corrected for phase shifts. No amplification factors were applied to either trace.

XAFS Analysis

The non-phase-shift corrected Fourier transforms of the k^3 weighted XAFS of the nickel-iron-cyanide network transferred onto Mylar are shown in Figure 4-4 for the iron and nickel edges. Both sets of data show a similar pattern with three dominant peaks attributed to the first three coordination shells. For the iron edge, the first two peaks correspond to the C and N of the cyanide ligand, respectively, and the third peak to the nickel ion coordinated to the nitrogen end of the cyanide bridge. For the nickel edge transform, the peak assignments can be made with the first peak corresponding to the cyanide nitrogen and most likely coordinated water, the second peak to the cyanide carbon, and the third peak to the iron atom. The significant intensity of the peaks at

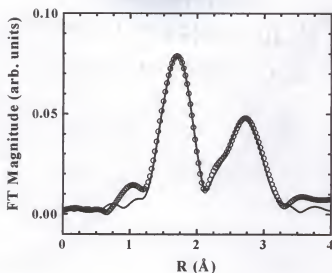


Figure 4-5. Fit (solid line) to the first two coordination shells of the Fourier transformed nickel edge XAFS (circles) of the nickel-iron-cyanide grid network on Mylar. The fit was calculated using FEFF7 codes for a model Ni^{2+} cluster coordinated in-plane by the nitrogen end of four cyanides and axially by two oxygen ligands.

approximately 4.5 Å in both radial plots has been explained in other cyanide-bridged systems as resulting from the focusing effect of the linear cyanide bridge.^{186,187}

The results of a fit to the first two coordination shells in the nickel edge k^3 weighted Fourier transformed XAFS data are shown in Figure 4-5. The fit was accomplished using the program Winxas with inputs from theoretical XAFS parameters generated from FEFF 7.0 codes^{85,86} for a model nickel cluster composed of two axial oxygen atoms and four equatorial nitrogen-bound, iron-terminated cyanide ligands. The coordination number for Ni was fixed and both shells were fit simultaneously using an intrinsic reduction factor (S_0^2) of 0.52 for each and an edge energy shift (ΔE_0) of 1.0 and 6.0 for the first and second shells, respectively. The S_0^2 and ΔE_0 values used in the fit were similar in magnitude to those reported in the XAFS analysis of a similar metal-

cyanide system.¹⁸⁸ The bond distances extracted from the fitting procedure were (in Å): Ni-N, 2.09; Ni-O, 2.11; Ni-C, 3.22; and C-N, 1.13; and are reasonable if compared to similar compounds.^{37,38,40} Fits to the Ni edge XAFS were limited to the first two coordination shells due to complexities arising from the large number of multiple scattering pathways contributing to the third coordination shell.

X-ray Diffraction and GIXD

The lamellar order in the multilayer films of the nickel-iron-cyanide network was confirmed by X-ray diffraction from a 30-bilayer sample. An intense diffraction peak at 2.5 degrees 2θ and a weaker harmonic at 5 degrees 2θ can be assigned to the (001) and (002) Bragg reflections and yield an inter-bilayer spacing of 35 Å. This inter-bilayer spacing is reasonable for the size of the amphiphile deposited as Y-type bilayers.

Grazing incidence X-ray diffraction was used to verify the presence of any long-range in-plane structural correlations in the film. The diffraction pattern obtained for a 39-bilayer sample of the iron-cyanide-nickel network transferred to glass is shown in Figure 4-6. The counts are normalized to the most intense peak and plotted versus the in-plane scattering vector $Q_{xy} = (4\pi/\lambda)(\sin\theta_{xy})$. The three intense peaks can be assigned to the (2,0), (2,2), and (4,0) Bragg reflections at d spacings of 5.10 Å, 3.61 Å, and 2.56 Å, respectively, from a face-centered square cell with an edge of $a = 10.2$ Å. The broad background centered at $ca. Q_{xy} = 1.41 \text{ Å}^{-1}$ and the shoulder at 1.58 Å^{-1} are likely due to the poorly organized alkyl chains.^{78,79} The isolated (4,0) peak was fit to a Lorentzian function and yielded a full width at half maximum ($Q_{xy_{fwhm}}$) of 0.1 Å^{-1} . Insertion of this value into the Scherrer equation,¹⁴⁷ $\xi = [(1.8\pi) / (Q_{xy_{fwhm}})]$, yields an average crystalline

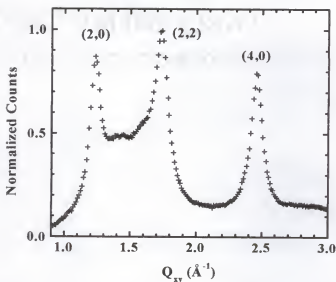


Figure 4-6. The difference between the field cooled and zero field-cooled magnetization, DM, is shown as a function of temperature. Typical data from the Mn-rich (i.e. $x > 0.25$) samples are shown when the magnetic field, for measuring and field cooling, was 100 G.

coherence length (ξ) of $\sim 60 \text{ \AA}$, or 5 unit cell lengths, indicating that the 2D networks cover an average area of approximately 3600 \AA^2 .

Magnetic Properties

The magnetic properties of a 10 cm^2 sample containing 300 bilayers (150 bilayers per side) of the nickel-iron-cyanide network transferred to Mylar were investigated by SQUID magnetometry. Two measurements were performed, one with the sample surface oriented parallel to the magnetic field and one with the sample surface oriented perpendicular to the magnetic field. The background corrected field-cooled magnetization versus temperature obtained in a field of 20 G is shown in Figure 4-7. The rise in magnetization below $T_c = 8 \text{ K}$ observed in both orientations is attributed to the onset of ferromagnetic order. The magnetic behavior is clearly anisotropic, with the sample displaying a stronger magnetic response when the surface is oriented parallel to

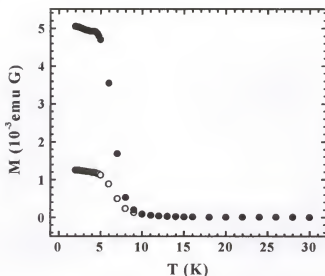


Figure 4-7. The temperature dependence of the magnetization after field cooling in 20 G with the sample surface aligned parallel (filled circles) and perpendicular (open circles), to the magnetic field. The measuring field was 20 G. The break at $T_c = 8$ K is indicative of long-range ferromagnetic order between the Fe^{3+} ($S = 1/2$) and Ni^{2+} ($S = 1$) centers.

the magnetic field. The presence of a ferromagnetic state at low temperature is further supported by the magnetization vs. field data taken at 2 K. The sample shows a rapid increase in magnetization at low field followed by a gradual approach toward saturation at higher fields. Cycling the magnetic field at 2 K results in the hysteresis loops (corrected for the diamagnetic background) shown in Figure 4-8. The plots are normalized to the magnetization at 5 T. Again, there is clear anisotropy in the magnetic behavior between the two orientations of the sample with respect to the field. When the field is parallel to the sample surface, the magnetization increases more rapidly with respect to the field and the remnant magnetization is 35% versus 8% in the perpendicular orientation. The coercive field is also slightly anisotropic, being 140 G in the parallel orientation and 110 G in the perpendicular orientation.

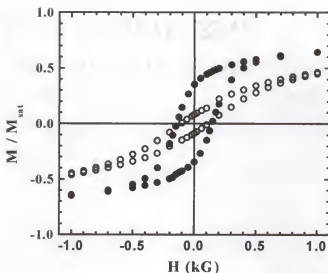


Figure 4-8. Hysteresis loops measured at 2 K with the sample surface aligned parallel to (filled circles) and perpendicular to (open circles) the applied magnetic field. The magnetization is normalized to the saturation magnetization.

Discussion

Choice of System and Monolayer Behavior

Designing a system to result in the formation of a coordinate-covalent network at the air-water interface requires the appropriate transition metal complex building blocks. Octahedral transition metal ions possessing linear bridging ligands are well suited to the assembly of square-grid networks since the required 90° bond angles are inherently present. By substituting one position with a hydrophobic ligand, the building block can be made amphiphilic and thus tailored for assembly reactions at the air-water interface. Condensation of the amphiphilic building block can then be accomplished by reaction with a suitable aqueous transition metal ion contained in the subphase. Confinement of the reacting system to the water surface directs the resulting structure to a two-dimensional motif.

The numerous examples of pentacyanoferrate complexes and the substitutional inertness of the cyanide ligand make this class of compounds well suited to our assembly strategy. Multilayer films of the single chain derivative of **3**, (4-octadecylamino-pyridine)pentacyanoferrate(III) (**4**) has previously been described.¹⁸⁹ The sodium salt of **4** was reported to be too soluble for film preparations, but when prepared as a mixed film with hexadecyltrimethylammonium counterions, stable Langmuir monolayers resulted. No difficulties with hydration of the single-chain complex were reported.

We decided to modify the pentacyanoferrate complex to the dual chain derivative to match more closely the size of the amphiphilic ligand with that of the metal complex head group. The addition of a second alkyl chain also decreased the solubility of the complex and eliminated the need for long chain alkyl ammonium counterions. It was found to be beneficial to exchange the sodium counterions for tetramethyl-ammonium ions to decrease the hygroscopic nature of the complex and to aid its dissolution in chloroform. The resulting complex forms a Langmuir monolayer that creeps slowly on water (Figure 4-2), but forms a highly stable film after reaction with aqueous Ni^{2+} ions to form an insoluble polymeric network.

Evidence for the condensation reaction is seen in-situ at the air/water interface. In the absence of Ni^{2+} , **3** forms a liquid expanded phase upon compression. This behavior is reasonable, as amphiphiles with twelve-carbon alkyl tails do not normally form condensed phases at the air-water interface at room temperature.¹⁹⁰ Upon addition of Ni^{2+} , a condensed phase is seen in the pressure vs. area isotherm and in Brewster angle microscopy. The mean molecular area of 52 \AA^2 at the onset of pressure correlates with

the limiting area per molecule of the complex over pure water and suggests that the film is highly condensed at zero pressure over the Ni^{2+} subphase.

In a mixed-metal cyanide square grid network (Scheme 4-1), a centered unit cell will have two iron amphiphiles per unit cell. Doubling the area per molecule, determined from the pressure vs. area isotherm, gives a cell area of 104 \AA^2 , which then corresponds to a cell edge distance of 10.2 \AA . This value is in agreement with the 10.2 \AA^2 determined for the cell edge by GIXD and suggests that the mean molecular area is determined by the lattice spacing of the inorganic two-dimensional grid network and not by the Van der Waals interactions of the organic chains.

Furthermore, BAM and surface pressure data indicate that the nickel-iron-cyanide network forms with or without preorganization of the monolayer. That is, the MMA obtained by compression of the iron amphiphile over a Ni^{2+} subphase is very close to the MMA obtained after injection of a Ni^{2+} solution under an organized monolayer of the iron complex. A condensed film is formed at zero pressure over the Ni^{2+} subphase, and subsequent compression of the film only acts to push together domains that have already assembled at the interface.

Structure of the Network

The formation of an extended two dimensional array is dependent on the exclusive bridging of the four in-plane cyanide ligands, as bridging of the trans cyanide ligand would effectively terminate the structure and result in an amorphous inorganic polymer. Evidence for a well-organized network from GIXD, XAFS, and FT-IR suggests that while coordination of the axial cyanide is possible, this mode is most likely labile in the absence of the added stability brought on by extended bridging interactions.

The results of the GIXD clearly show the presence of a structurally coherent inorganic network in the mixed metal film. The three peaks shown in Figure 4-6 fit very well to the expected ($h\ k$) pattern for a face-centered square grid network. The unit cell edge length of 10.2 Å deduced from the diffraction data is very similar to that reported in cubic Prussian blue derivatives.¹⁹¹ The high background scattering near 1.4 Å⁻¹ and 1.6 Å⁻¹ is in the range of Q_{xy} normally seen for alkyl chain packing and suggests that the alkyl chains are loosely organized. This observation would be expected in light of the large area per alkyl chain in the condensed network.

The XAFS data complement the conclusions of the GIXD experiments. The Ni-N, C-N, and Ni-C distances of 2.09 Å, 1.13 Å, and 3.22 Å, respectively, were obtained from modeling the Ni edge XAFS. Combining these bond lengths with the average Fe-C bond length of 1.95 Å reported for other Fe-CN-Ni bridged systems,^{38,40} leads to a Ni-Fe separation of 5.17 Å. This value is close to the 5.10 Å separation deduced from the GIXD. The quality of the XAFS fit supports the modeled nickel coordination environment in which the octahedral nickel ions are coordinated in-plane by the nitrogen terminus of the cyanide bridge and the axial sites by oxygen, most likely from coordinated water.

Magnetism

The formation of a structurally coherent inorganic network at the air-water interface is confirmed by the transition to a ferromagnetic state below 8 K in the multilayer film containing 150 bilayers per side. The ability of the cyanide ligand to mediate magnetic exchange between two paramagnetic metal ions is well known and has been extensively explored in cubic Prussian blue derivatives. In particular, the Fe³⁺/Ni²⁺ Prussian blue^{192,193} was found to be ferromagnetic with a T_c of 23 K. In addition,

ferromagnetic exchange has also been reported in a series of two-dimensional cyanide-bridged iron-nickel compounds with T_c 's on the order of 10 K.^{38,194} The ferromagnetic behavior of these materials is rationalized¹⁹⁵ by realizing that for octahedral metal centers, the magnetic orbitals are the Fe^{3+} ($S = 1/2$) t_{2g} and the Ni^{2+} ($S = 1$) e_g sets, and that the cyanide orbitals that overlap with each of them are orthogonal.

For the Fe^{3+}/Ni^{2+} LB film system, the ordering temperature of 8 K is lower than the T_c of 23 K observed in the cubic analogue, and is more similar in magnitude to the ordering temperature reported in other low dimensional Fe-CN-Ni networks.¹⁹⁶ Lower ordering temperatures for the 2D systems relative to the cubic analogues is expected as the number of exchange pathways per magnetic ion is reduced. Further evidence for a two dimensional network is obtained from the anisotropic magnetic behavior seen in the film. The stronger magnetic response of the sample when oriented with the surface parallel to the magnetic field suggests a magnetic easy axis within the plane of the network. A strict analysis of a magnetic vector in the film is limited though due to uncertainties in how the microscopic surface roughness of the substrate affects variations in the orientation of network sheets relative to the plane defined by the macroscopic substrate. The high anisotropy of the magnetization does discriminate against the magnetic behavior arising from cubic Prussian blue-like particles and is highly suggestive of a low dimensional system.¹⁹⁷ More detailed studies on the magnetic properties of the LB film networks are ensuing since the unique structural features of these monolayer networks may provide experimental probes of the exchange coupling interactions in metal cyanide networks and the how the issue of dimensionality influences ordering in mixed-spin 2D systems.^{198,199}

Mechanism and Structure Directing Elements

The two-dimensional nickel-iron-cyanide network forms at the air/water interface, but does not require pre-organization of the amphiphiles. The condensation reaction proceeds in the absence of applied surface pressure when the amphiphile **3** is spread on the Ni^{2+} containing subphase, in which case subsequent reduction of the surface area simply compresses the preformed domains. Compression of the film thus appears to do little to extend the in-plane order of the networks, and instead, only works to increase the density of the domains allowing for better transfer of the networks to solid supports. Pre-organization of the amphiphile, followed by injection of Ni^{2+} ions into the subphase results in the same network, with no significant difference in domain organization.

Control of the reaction to form the square grid network results from the orientational constraints of the octahedral metal complex with linear cyanide bridging in combination with the interface as a structure-directing element. This view is supported by attempts to form the same networks from solution. The analogous reaction of **3** with Ni^{2+} in methanol yields an insoluble precipitate, which is shown by X-ray diffraction to be amorphous. When compared to the homogeneous reaction, the air-water interface not only directs the structure of the final material, but also acts to enhance the structural coherence length as well.

It is interesting to compare the mechanism of formation of the metal cyanide two-dimensional networks to other examples of Langmuir-Blodgett films that contain inorganic networks. For example, there are now several examples of metal phosphonate based LB films, where the inorganic extended solid networks determine the in-plane structures.^{109,117,145} The difference is that for the metal phosphonates, the LB films form with the same structure that forms in the solid-state. The structure is determined by the

inorganic lattice energy. With the metal phosphonates, the LB film processing directs where the structure will form and affords control of the fabrication to one layer at a time, but the air/water interface does not act as a structure-directing element. In contrast, the iron-cyanide-nickel network described here does not form from compound **3** in the absence of the interface. The interface directs where the reaction will take place and limits the reaction to one layer at a time, but importantly, it also directs the structure.

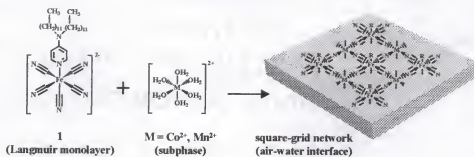
Conclusions

An amphiphilic octahedral iron complex containing linear cyanide ligands was designed and synthesized as a building block for the assembly of two dimensional square grid nickel-iron-cyanide networks at the air-water interface. The reaction of Langmuir monolayers of this complex with aqueous nickel ions contained in the subphase results in the formation of coordinate covalent networks. Characterization of these networks by various techniques indicates that the structure is two-dimensional and coherent over an average domain size of 3600 \AA^2 . Magnetic measurements indicate a ferromagnetically ordered state below 8 K with the magnetic behavior highly dependent on the orientation of the sample with respect to the field. This synthetic method demonstrates that the air-water interface can function as a structure-directing element in the assembly of new supermolecular network solids and, in addition, provides a means for transferring these materials in a controlled fashion to solid supports. This assembly strategy may aid in the future development of nanoscale materials and with interfacing them at a surface.

CHAPTER 5 INTERFACIAL ASSEMBLY OF CYANIDE-BRIDGED FE-CO AND FE-MN SQUARE GRID NETWORKS

Introduction

Coordination chemistry routes to finite and infinite networks make use of the predictable directional characteristics of coordinate covalent bonds.^{14,15,28,29,45-47,200-202} Tunable variables like stoichiometry, template additives, secondary structure building blocks, or kinetic control are used to determine the final network structure, and several examples are included in the current issue. Potential applications of inorganic finite and infinite networks include recognition and sensing, catalysis, electronic and optical functions, and magnetic effects related to information storage.^{152,200,202} It is interesting to note that several of these applications are likely to involve positioning at surfaces, and routes to locate the finite or infinite networks at interfaces will be needed.^{57-60,62-65,203,204} One approach is to involve the interface directly in the assembly, to carry out the network fabrication where it will be located. In this case, the interface can play a role in determining the network structure. Examples of assembly at liquid interfaces have been published, including some two-dimensional infinite networks.^{62,63,80,154,155,167,168} The surface of a liquid retains the structure directing character of an interface, but at the same time is fluid and can facilitate diffusion of reactants. Careful understanding of these processes is now possible largely as a result of surface sensitive characterization methods, including grazing incidence X-ray diffraction as detailed in a recent review.⁸⁰



Scheme 5-1. Assembly of two-dimensional grid networks at the air-water interface.

We recently reported the fabrication of an $\text{Fe}^{3+}/\text{Ni}^{2+}$ mixed-metal cyanide-bridged square grid network at the air-water interface, showing that the interface can act as a structure directing entity when preparing coordinate covalent networks.²⁰⁵ In this paper, we show the process is general and describe two new examples of square grid networks prepared as monolayers at the air/water interface. The technique, outlined in Scheme 5-1, uses the air/water interface and involves the reaction of an amphiphilic pentacyanoferrate (3+) complex (**1**) confined to a monolayer on a aqueous subphase containing a second divalent metal ion. By confining one of the reactants to the air/water interface the propagation of the structure in the third dimension is prevented, resulting in a planar network at the water surface. The effect of the interface works in tandem with the defined bond angles of the octahedral metal complexes and the linear geometry of the cyanide bridge to direct the final structure of the network to a face-centered square grid array. The same reactants in a homogeneous reaction give amorphous colloidal products, thus illustrating the ability of an interface to direct the structure of the network. Also, the interface-assembled network can be conveniently transferred to solid supports by the

Langmuir-Blodgett technique, permitting added structural and materials property characterization.

The cyanide ligand is particularly attractive for use in network assembly. Its linear geometry and ambidentate nature make for a versatile building block when combined with various transition metal complex geometries.^{13,19,21,22,38,51,52,169-172} In addition, cyanide has been shown to mediate both magnetic and electronic exchange between the bridged metal centers, giving rise to materials with interesting physical properties, including a family of molecule-based magnets.^{51-53,169,173,174} We previously reported an $\text{Fe}^{3+}/\text{Ni}^{2+}$ cyanide bridged network prepared at the air/water interface and showed it to be magnetic.²⁰⁵ This study extends the series to include $\text{Fe}^{3+}/\text{Co}^{2+}$ and $\text{Fe}^{3+}/\text{Mn}^{2+}$ mixed metal cyanide networks. These new two-dimensional networks are also magnetic, and their behavior is compared to related three-dimensional hexacyanometalate complexes.

Experimental Section

Materials. The amphiphilic complex tetramethylammonium pentacyano(4-didodecylaminopyridine)ferrate(III) $\cdot 6\text{H}_2\text{O}$ was prepared as previously described.²⁰⁵ Attenuated total reflectance (ATR) FT-IR samples were prepared as monolayers on clean silicon ATR crystals. Grazing incidence X-ray diffraction (GIXD) samples were prepared on petrographic slides that were first cleaned using the RCA procedure¹⁷⁸ and made hydrophobic by deposition of a monolayer of octadecyltrichlorosilane.^{179,180} Samples for SQUID magnetometry measurements were prepared on Mylar (Dupont) substrates cleaned with absolute ethanol prior to use.

Film preparation. The amphiphilic iron complex **1** was spread onto the water surface from a chloroform solution. Multilayer films of the iron-cyanide-manganese and

iron-cyanide-cobalt networks were transferred as Y-type films onto hydrophobic substrates at a surface pressure of 25 mN/m over a subphase 1 g/L in $\text{Mn}(\text{NO}_3)_2 \times \text{H}_2\text{O}$ or $\text{Co}(\text{NO}_3)_2 \times \text{H}_2\text{O}$ at ambient temperature. Transfer ratios for both the upstrokes and downstrokes were between 0.85 and 1 for all layers.

Instrumentation. IR spectra were collected using a Mattson Instruments (Madison, WI) Research Series-1 FTIR spectrometer with a deuterated triglycine sulfate (DTGS) detector. The LB films were prepared by using a KSV Instruments 5000 trough modified to operate with double barriers. The surface pressure was measured with a filter paper Wilhelmy plate suspended from a KSV microbalance. Subphase solutions were prepared from 17.8-18.1 M Ω cm water delivered with a Barnstead Epure system. Magnetization measurements were performed on a Quantum Design MPMS SQUID magnetometer. GIXD experiments using synchrotron radiation were performed at the Advanced Photon Source, Argonne, IL, at the Materials Research Collaborative Access Team beamline (sector 10).^{76,205} The GIXD scans were performed on LB films transferred to glass slides. The sample was positioned in the center of an 8-circle Huber goniometer and oriented at an angle of 0.13 degrees relative to the incident beam. The incident beam was collimated to 200 microns high by 1500 microns wide and tuned to a wavelength of 1.254 Å. Diffracted intensity in the xy plane was measured using a NaI scintillation counter mounted on the Huber goniometer. The diffracted signal was collimated prior to the detector using Soller slits giving an experimental resolution on the order of 0.015 Å⁻¹.

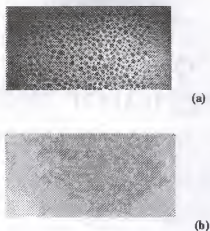


Figure 5-1. BAM images taken at zero surface pressure of complex **1** over (a) pure water and over (b) a 1 mmol Mn^{2+} subphase.

Results and Discussion

Langmuir Monolayers

Evidence for the condensation reaction is first seen directly at the air/water interface using the traditional Langmuir monolayer methods of Brewster angle microscopy (BAM) and pressure vs. area isotherms. At room temperature, the amphiphilic pentacyanoferrate (3+) complex **1** is in a liquid expanded phase on water (with NaCl), forming two-dimensional bubbles at the interface in the absence of applied pressure (Figure 5-1a). As the film is compressed, a continuous film forms. The pressure vs. area isotherm for **1** does not show evidence for a phase transition with increased pressure, indicating that **1** maintains the liquid expanded phase up until collapse.

If a complexing metal ion (Mn^{2+} or Co^{2+}) is added to the subphase, the amphiphile behaves very differently, forming a condensed phase at all pressures. The monolayer must be compressed to a much smaller area before the surface pressure increases (Figure 5-2). After the surface pressure begins to rise, the slope is much sharper than in the absence of complexing ions, reflecting the lower compressibility of the film. The

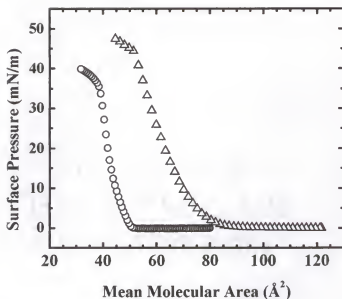


Figure 5-2. Room temperature surface pressure vs. mean molecular area isotherms for complex 1 over pure water (triangles) and 1g/L $\text{Co}(\text{NO}_3)_2$ (circles).

condensed phase over Mn^{2+} is seen in the BAM image, Figure 5-1b. The behavior is consistent with cross linking of the amphiphiles by the subphase metal ions through cyanide bridges to form a network. The limiting area for the condensed films at low applied pressures is between 50 and 60 $\text{\AA}^2/\text{amphiphile}$, which will be shown, below, to agree with XRD data.

Infrared Spectroscopy

The network monolayers can be transferred onto solid supports using traditional LB deposition procedures, permitting further structural and physical property characterization. Evidence for cyanide bridging is seen by FTIR. Attenuated total reflectance FTIR spectra of the cyanide stretches for the condensed films are compared in Figure 5-3 to those of (1), obtained as a KBr pellet. The spectrum of complex (1) shows a band at 2111 cm^{-1} with a shoulder at 2128 cm^{-1} and is in the typical range with the

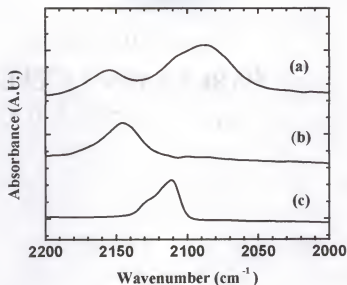


Figure 5-3. Infrared absorbance spectra of the C-N stretching region for monolayer films on Si ATR crystals of the grid network formed from the reaction of complex 1 with (a) Co^{2+} and (b) Mn^{2+} compared to (c) the spectrum of 1 as a KBr pellet.

expected splitting for an Fe^{3+} pentacyanide complex. The Fe-Mn film shows a broad band centered at 2145 cm^{-1} and agrees well with the CN stretching frequency reported for the related $\text{Mn}_3[\text{Fe}(\text{CN})_6]$ Prussian blue analogue,²⁰⁶ confirming the presence of Fe-CN-Mn bridging in the film. The FT-IR spectrum for the Fe-Co film is more complex and shows a split band with a peak at 2155 cm^{-1} and a broad peak at 2090 cm^{-1} . A similar splitting has been reported in a $\text{Co}[\text{Fe}(\text{CN})_6]$ Prussian blue analogue and has been attributed to the presence of two different oxidation states of the iron cyanide complex.²⁰⁷ The peak at higher wavenumbers is due to an $\text{Fe}^{3+}\text{-CN-Co}^{2+}$ bridge and the lower energy peak to an $\text{Fe}^{2+}\text{-CN-Co}^{2+}$ bridge. The band reported at 2133 cm^{-1} for $\text{Co}[\text{Fe}(\text{CN})_6]$ attributed to an $\text{Fe}^{2+}\text{-CN-Co}^{3+}$ bridge is not observed in the monolayer Fe-Co film. The IR data suggest that some Fe^{3+} is reduced in the network, as in the three-dimensional

analog, but the relatively large excess of Co^{2+} in the subphase assures that any Co^{3+} that forms in the network is quickly reduced, leaving only Co^{2+} in the film.

Grazing Incidence X-ray Diffraction

The in-plane structure of the networks is confirmed by X-ray diffraction. The small quantity of material and strong background scattering make conventional X-ray sources ineffective for characterizing the in-plane structure of thin films. However, the combination of enhanced X-ray flux from synchrotron radiation with grazing incidence angles reduces the signal to noise ratio to a level where scattering from as little as a monolayer film can be detected. This method of grazing incidence X-ray diffraction (GIXD) has been described in detail.⁷⁸ The GIXD patterns obtained on 15-bilayer samples of the Fe-Mn and Fe-Co networks transferred to glass slides are shown in Figure 5-4. Both patterns show the same three peaks, with slight shifts in spacing, and confirm that the Fe-Mn and Fe-Co networks are isostructural. The diffraction peaks for the Fe-Mn film correspond to lattice spacings of 5.18 Å, 3.69 Å, and 2.61 Å. The analogous spacings for the Fe-Co film are 5.10 Å, 3.62 Å, and 2.55 Å, respectively. Both patterns can be indexed to a face centered square network with Miller indices of (20), (22), and (40), in order from large to small spacings, and yield face-centered square unit cells of $a = 10.36$ Å for the Fe-Mn and $a = 10.20$ Å for the Fe-Co networks. Analysis of the peak widths of the (20) and (40) reflections in both films by application of the Scherrer equation¹⁴⁷ yields a structural coherence length of approximately 80 Å for both films.

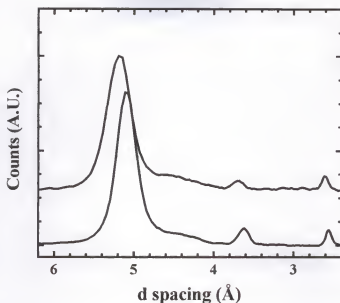


Figure 5-4. Grazing incidence X-ray diffraction patterns for 10 bilayer samples on glass of the (a) Fe-Mn and (b) Fe-Co grid networks. Both patterns can be indexed to a face-centered square grid network with cell edges of 10.4 Å (a) and 10.2 Å (b).

Magnetism

The three-dimensional analogs $\text{Mn}_3[\text{Fe}(\text{CN})_6]_2$ and $\text{Co}_3[\text{Fe}(\text{CN})_6]_2$ are low-temperature ferrimagnets with T_c of 9 K and 14 K, respectively.¹⁹² Magnetic exchange in these compounds is mediated by the cyanide ligand. The temperature dependent magnetization for the two-dimensional assemblies is reported in Figure 5-5 for the Fe-Co film and in Figure 6 for the Fe-Mn film, each in two orientations. The Fe-Co sample was 100 bilayers per side and the Fe-Mn sample 125 bilayers per side. Both films were on 10 cm^2 of Mylar substrate. The magnetic behavior of each film is consistent with the ferrimagnetic exchange observed for the three-dimensional parent compounds, although a significant diamagnetic background contribution from the Mylar substrate makes it difficult to unambiguously quantify the moments to discern ferrimagnetism from

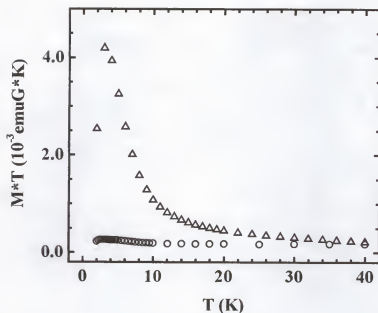


Figure 5-5. The temperature dependence of the product of the zero-field magnetization (measured in 20 G) and temperature for a 100 bilayer (per side) sample of the Fe-Co network on Mylar showing the anisotropy of the magnetic response when the field is applied parallel to the sample surface (triangles) and perpendicular to the sample surface (circles).

ferromagnetic exchange in the transferred films. The magnetic response of each film is anisotropic with respect to the sample orientation in the applied magnetic field. The Fe-Co film shows negligible magnetic response (Figure 5-5) when the field is applied perpendicular to the magnetic planes. Conversely, magnetization increases rapidly below 10 K with the applied field parallel to the plane of the network. The magnetic response of the Fe-Mn film (Figure 5-6) is also anisotropic, but in the opposite sense. The variation in the orientation of the magnetic easy axes must reflect the reduced symmetries of the crystal fields in the two-dimensional networks and the differences in single ion

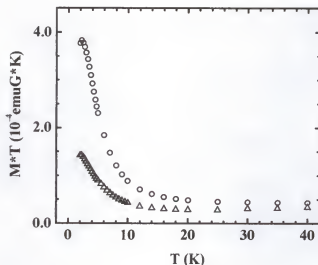


Figure 5-6. The temperature dependence of the product of the zero-field cooled magnetization (measured in 20 G) and temperature for a 125 bilayer (per side) sample of the Fe-Mn network on Mylar showing the anisotropy of the magnetic response when the field is applied perpendicular to the sample surface (circles) and parallel to the sample surface (triangles).

anisotropies expected for Co^{2+} , Mn^{2+} , and low spin Fe^{3+} . The pentacyanoferrate(3+) complex common to both structures is a low-spin d^5 ion, known to experience significant spin-orbit coupling.²⁰⁸ In addition, the 4-aminopyridine ligand and bridging of the in-plane cyanides lowers the symmetry of the Fe^{3+} site. When coupled with the isotropic $S = 5/2$ Mn^{2+} ion, the ferric site can be expected to define the magnetic easy axis. In the case of the Fe-Co material, the strong Ising character of the Co^{2+} ion dominates, in this case confining the moments to the network plane. The anisotropy of the Fe-Co film is similar to that observed for the analogous Fe-Ni film that was described previously.²⁰⁵

When the monolayers are transferred to solid supports for magnetic studies they form bilayers with the metal cyanide networks depositing face-to-face. Each inorganic bilayer is then separated from the next by the alkyl tails of the amphiphilic aminopyridine

ligand. The exact nature of the interaction between the face-to-face networks is not yet clear, nor is its influence on the anisotropic response. More detailed magnetic studies comparing true monolayers with the multilayer films are underway. Nevertheless, magnetic exchange in the films provides additional evidence that extended networks form in the condensation reaction at the air/water interface. In addition, the anisotropic magnetic behavior discriminates against a cubic Prussian blue-like product and is consistent with a planar structure.

Conclusions

Reaction of an amphiphilic pentacyanoferrate(3^+) complex at the air/water interface with divalent metal ions from the subphase results in two-dimensional cyanide-bridged coordinate-covalent networks. Confining one of the reactants to the surface of water illustrates the concept that the interface can be used as a structure-directing element for preparing two-dimensional arrays. The same reaction in the absence of the interface generates amorphous colloids. The cyanide bridges mediate magnetic exchange, just as in the related three-dimensional hexacyanometalate analogs, but the two-dimensional networks lead to anisotropic behavior that changes with the identity of the metal ions.

CHAPTER 6
FERROMAGNETISM AND SPIN-GLASS BEHAVIOR IN LANGMUIR-BLODGETT
FILMS CONTAINING A TWO-DIMENSIONAL IRON-NICKEL CYANIDE SQUARE
GRID NETWORK

Introduction

Metal cyanides are a structurally diverse class of materials. The best known examples come from the family of "Prussian blues" (named after the mixed-valent deep blue $\text{Fe}^{\text{III}}[\text{Fe}^{\text{II}}(\text{CN})_6]$) which consist of octahedral metal ions bridged through $[\text{M}(\text{CN})_6]^{n-}$ to form three-dimensional cubic solids.²⁰⁹ However, many other structural motifs have been realized by introducing "blocking ligands" to one or both of the metal complex building blocks, thereby lowering their symmetry and the symmetry of the final cyanide-bridged arrays. This strategy has yielded an array of structures over a wide range of dimensionality including clusters,¹⁸⁻²⁵ molecular squares,^{26,27} linear chains,³⁰⁻³² ladders,^{33,34} as well as quasi-two-dimensional square-grid³⁷⁻⁴⁰ and "honeycomb" networks.^{41-43,210,211}

Aside from their structural diversity, metal-cyanides also show interesting magnetic behavior. For many examples, the nature of the magnetic exchange can be anticipated in advance from basic orbital interaction arguments and the predictable structure-directing quality of the cyanide bridge. This inherent ability to tailor both the structure and magnetic exchange in metal-cyanide systems makes this family of materials well suited for studying molecule-based magnetic phenomena. Indeed, a wide range of

Initial investigations into the magnetic properties of the multiple bilayer films comprised of these Fe-Ni networks by DC magnetometry revealed a ferromagnetic state below 8 K. Single-layer control over the deposition process provides an opportunity to observe how the magnetic properties of the system evolve as it changes from a monolayer to a bilayer to a multilayer film. We report herein a detailed investigation of the magnetic properties of this 2D system using both DC and AC magnetometry which reveals both ferromagnetic and spin-glass behavior at low temperatures.

Experimental

Materials. Nickel nitrate hexahydrate (99%) was purchased from Aldrich (Milwaukee, WI) and used as received. The amphiphilic complex (**1**) Bis(tetramethylammonium) pentacyano(4-didodecylaminopyridine)ferrate(III) · 6H₂O was prepared as described.²⁰⁵ Subphase solutions were prepared from 17.8–18.1 MΩ cm water delivered with a Barnstead Epure system.

Film preparation. All films were prepared on Mylar substrates precleaned with absolute ethanol. The 150 bilayer-per-side sample was prepared as previously described.²⁰⁵ Briefly, a Langmuir monolayer of complex **1** is reacted at the air water interface over a subphase containing 1 g/L of Ni(NO₃)₂·6H₂O (see Scheme 6-1). The resulting square grid network that forms is transferred at a surface pressure of 25 mN/m as a y-type film by the Langmuir-Blodgett technique. The transfer ratio (T_R) of the 150 bilayer sample (**FeNi-150**) was $T_R = 1.0 \pm 0.1$ for both the upstrokes and downstrokes throughout the transfer process (where $T_R = 1.0$ signifies a complete monolayer transfer). A separate sample consisting of a single bilayer (**FeNi-bi**), i.e. one downstroke followed by one upstroke, was prepared on a Mylar surface pre-coated with 5 bilayers of

octadecanol (for increased hydrophobicity). The transfer ratio for **FeNi-bi** was $T_R = 1.0 \pm 0.1$ for both the downstroke and upstroke. A sample consisting of a single monolayer of the Fe-Ni grid network (**FeNi-mono**) was prepared using a single transfer starting with the Mylar immersed in the subphase, i.e. hydrophilic transfer. The transfer ratio for **FeNi-mono** was $T_R = 1.0 \pm 0.1$.

For magnetic measurements, each sample measuring 10 cm^2 was cut and packed into gel caps for SQUID magnetometry. The rectangular pieces were packed parallel to one another and oriented with the plane of the sample surface aligned parallel ($//$) or perpendicular (\perp) to the applied DC or AC magnetic fields. Background corrections were applied by subtraction of the diamagnetic signal measured on a similar (within 3%) mass of clean Mylar and sample container.

Instrumentation. The LB films were prepared by using a KSV Instruments 5000 trough modified to operate with double barriers. The surface pressure was measured with a filter paper Wilhelmy plate suspended from a KSV microbalance. Magnetization measurements were performed on a Quantum Design MPMS SQUID magnetometer. For the AC susceptibility, χ_{AC} , all measurements of the in-phase (real or dispersive) susceptibility, χ' , and out-of-phase (imaginary or absorptive) susceptibility, χ'' , were made after zero field cooling the sample, with subsequent warming under zero applied DC field and an oscillating AC field of 4 G.

Results

Film Structure

The two-dimensional grid network prepared as shown in Scheme 6-1 has been structurally characterized by grazing incidence x-ray diffraction, x-ray absorption fine structure, infrared spectroscopy, and x-ray photoelectron spectroscopy.²⁰⁵ The in-plane structure of the network consists of a face-centered square grid array of low spin Fe^{III} ions that are bridged through cyanide to Ni^{II} ions. The in-plane lattice parameter is $a = 10.4 \text{ \AA}$, which yields an Fe-Ni separation of 5.2 \AA . The average structure coherence length, as determined from x-ray diffraction, is approximately 6 unit cell lengths. This gives an average coherent particle size on the order of 3600 \AA^2 , which would contain approximately 144 ions (72 Fe^{III} ions and 72 Ni^{II} ions).

As depicted in Scheme 6-1, the networks can be transferred to solid supports in a controlled fashion by the LB technique. If the dipping cycle begins with the substrate submerged, withdrawal of the substrate will result in the transfer of a single monolayer of the Fe-CN-Ni network (**FeNi-mono**) oriented such that the inorganic network is in direct contact with the substrate surface. In this case, the planar network is an isolated two-dimensional system (it is not truly isolated, as a large anisotropic background arises from the substrate). On the other hand, if the substrate begins above the water surface, one dipping cycle of passing the substrate into the subphase and back out results in a bilayer (**FeNi-bi**), with the organic portion of the material in contact with the substrate and inorganic networks face-to-face, sandwiched in the center of the bilayer. The nature of the bonding interaction in the interfacial region between the networks is uncertain, but likely contains a mixture of covalent bonding via coordination of the axial cyanide of the iron complex to Ni^{2+} ions in the adjacent layer, hydrogen bonding via intercalated water

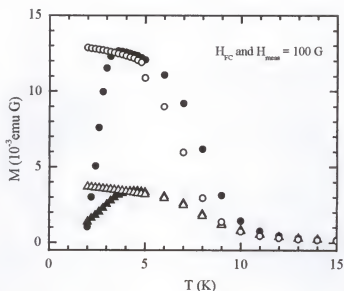


Figure 6-1. Background corrected $M(T)$ for FeNi-150 aligned parallel to the applied field [(○) field-cooled and (●) zero field-cooled] and perpendicular to the applied field [(△) field-cooled and (▲) zero-field cooled]. Cooling fields and measuring fields were each 100 G.

molecules, or simple electrostatic interactions. These interactions should give an average distance between inorganic networks within the bilayer on the order of 10 Å or less.

Finally, if the dipping cycled is repeated through 150 cycles (FeNi-150), each bilayer of the Fe-CN-Ni network will be deposited onto the previous bilayer forming a y-type LB film with alternating regions of organic-to-organic and inorganic-to-inorganic contacts.

DC Magnetometry

The field-cooled (M_{fc}) and zero-field-cooled (M_{zfc}) magnetizations as a function of temperature for FeNi-150 in two orientations with respect to the applied field are shown in Figure 6-1. Both M_{fc} curves show a rapid rise in the magnetization at lower temperatures below approximately 10 K, gradually saturating below 5 K. This behavior is indicative of ferromagnetic exchange in the film. Ferromagnetism is rationalized in

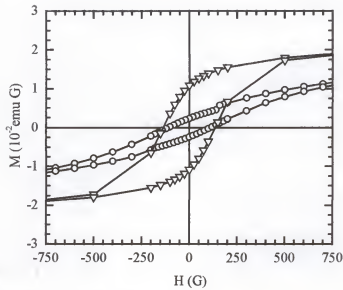


Figure 6-2. Background corrected $M(H)$ measured at 2 K for **FeNi-150** aligned parallel (\circ) to the applied field and perpendicular (∇) to the applied field. (The total sweep width was -50 kG to 50 kG). The lines are guides to the eye.

this system as resulting from the orthogonal low spin $S = \frac{1}{2} \text{Fe}^{\text{III}} \text{T}_{2g}$ and $S = 1 \text{Ni}^{\text{II}} \text{e}_g$ magnetic orbitals favoring the maximum total spin in accordance with Hund's rule. The field-cooled magnetic response of the material is clearly anisotropic with $M_{\parallel} \sim 4M_{\perp}$ at $T = 4$ K and reflects the planar anisotropy of the network.

Ferromagnetism in **FeNi-150** is also supported by the hysteresis in M vs. H at $T = 2$ K as shown in Figure 6-2. Again, the magnetization is anisotropic with a larger remnant magnetization when the sample is aligned parallel to the applied field. The coercive fields are slightly anisotropic as well with $H_c = 135 \pm 5$ G in the parallel orientation, and $H_c = 110 \pm 5$ G in the orientation perpendicular. The nature of the LB film samples results in significant diamagnetic background arising from the substrate and sample container, making it difficult to quantify the film response at high magnetic fields. Therefore, the saturation moment and saturation fields are not well defined.

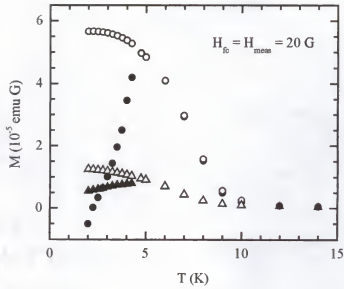


Figure 6-3. Background corrected $M(T)$ for **FeNi-bi** aligned parallel to the applied field [(○) field-cooled and (●) zero field-cooled] and perpendicular to the applied field [(△) field-cooled and (▲) zero-field cooled]. Cooling fields and measuring fields were each 20 G.

Plots of the magnetization of **FeNi-bi** as a function of temperature for both field-cooled and zero-field-cooling are shown in Figure 6-3. Data are shown for the parallel and perpendicular orientations. As observed in the multilayer sample, there is a sudden rise in the field-cooled magnetization below 10 K, signaling ferromagnetic exchange. The magnetization tends toward saturation below 4 K. The field-cooled magnetic response shows a slightly larger anisotropy than observed in the multilayer sample with $M_{//} \sim 5M_{\perp}$ at $T = 2$ K.

The M vs. H plots are shown in Figure 6-4 for **FeNi-bi** in both orientations. The magnetic behavior is anisotropic in both the remnant magnetization and coercive field with $H_c = 75 \pm 5$ G in the parallel orientation, and $H_c = 55 \pm 5$ G when perpendicular.

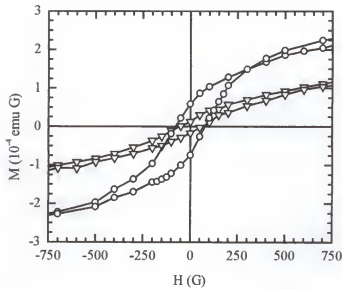


Figure 6-4. Background corrected $M(H)$ at 2 K for **FeNi-bi** aligned parallel (\circ) to the applied field and perpendicular (∇) to the applied field. (The total sweep width was -50 kG to 50 kG). The lines are guides to the eye.

The coercive fields for the **FeNi-bi** are significantly smaller than those observed in the multilayer film.

The field-cooled and zero-field-cooled magnetizations as a function of temperature for the **FeNi-mono** sample are shown in Figure 6-5. The magnetic response in the monolayer film shows a higher anisotropy than the bilayer or multilayer films, with the magnetization in the parallel orientation an order of magnitude more intense than the perpendicular. The parallel M_{fc} increases abruptly with decreasing temperature below $T \approx 7$ K, suggesting the onset of ferromagnetic order. The onset temperature is below the 10 K seen in the **FeNi-bi** and **FeNi-150** samples, perhaps reflecting the decrease in the number of possible exchange pathways in the isolated monolayer film.

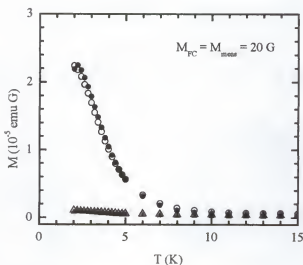


Figure 6-5. Background corrected $M(T)$ for **FeNi-mono** aligned parallel to the applied field [(○) field-cooled and (●) zero field-cooled] and perpendicular to the applied field [(△) field-cooled and (▲) zero-field cooled]. Cooling fields and measuring fields were each 20 G.

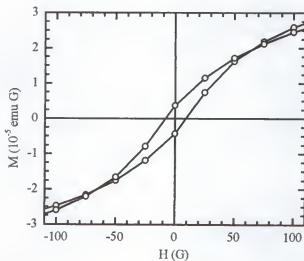


Figure 6-6. Background corrected $M(H)$ measured at 2 K for **FeNi-mono** aligned parallel to the applied field. (The total sweep width was -50 kG to 50 kG). The lines are guides to the eye.

The M vs. H hysteresis loop for the **FeNi-mono** measured in the parallel orientation at $T = 2\text{ K}$ is shown in Figure 6-6. The data indicate a very weak hysteresis with a coercive field on the order of $H_c = 10\text{ G}$. This value is close to the instrumental resolution, which is limited by the pinned flux within the instrument, also found to be on the order of 10 G .

AC Magnetometry

The nature of the low temperature magnetic behaviors of the films were further probed using AC magnetometry. The temperature-dependent χ_{ac} for **FeNi-150** in the parallel orientation, measured at 17 Hz , 170 Hz , and 1.0 kHz are shown in Figure 6-7. The data show both χ' (real) and χ'' (imaginary) components. The presence of a χ'' component is indicative of uncompensated moments in agreement with the hysteresis observed in the $M(H)$ data, shown in Figure 6-2. The frequency dependence of the peak position in both components is a signature of spin-glass behavior.¹²⁶ The spin glass transition temperature, $T_g = 5.4\text{ K}$, is defined by the maximum in the $\chi'(T)$ plot at low frequency, here 17 Hz . The anisotropy of the magnetization is again revealed by comparison to the $\chi_{ac}(T)$ data taken on **FeNi-150** in the perpendicular orientation shown in Figure 6-8. While the two components are present with similar frequency dependence, the magnitude of the magnetic response is an order of magnitude lower than in the parallel orientation. The temperature of the $\chi'(T)$ maximum (5.2 K) is slightly less than that extracted from the parallel orientation.

The $\chi_{ac}(T)$ data for the parallel orientation of **FeNi-bi**, shown in Figure 6-9, are noticeably different than what is observed for the multi-layer film. The broad feature in the $\chi'(T)$ is clearly resolved into two components in the $\chi''(T)$ data. The presence of a

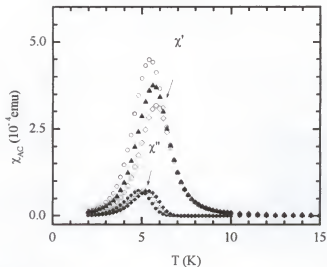


Figure 6-7. The background corrected AC susceptibility, $\chi'(T)$, [(\circ) 17 Hz, (\blacktriangle) 170 Hz, and (\diamond) 1 kHz] and $\chi''(T)$, [(\bullet) 17 Hz, (\triangle) 170 Hz, and (\blacklozenge) 1 kHz] for FeNi-150 aligned parallel to the applied field. The samples were measured with an AC field of 4 G under zero applied DC field.

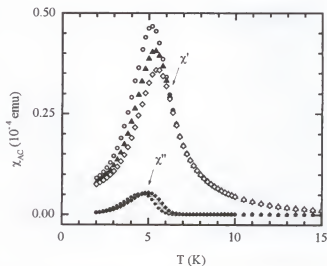


Figure 6-8. The background corrected AC susceptibility, $\chi'(T)$, [(\circ) 17 Hz, (\blacktriangle) 170 Hz, and (\diamond) 1 kHz] and $\chi''(T)$, [(\bullet) 17 Hz, (\triangle) 170 Hz, and (\blacklozenge) 1 kHz] for FeNi-150 aligned perpendicular to the measuring field. The samples were measured with an AC field of 4 G under zero applied DC field.

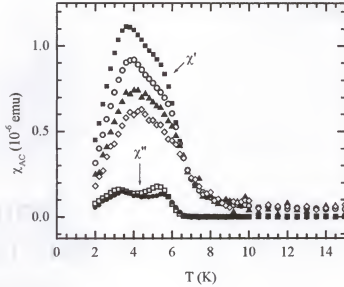


Figure 6-9. The background corrected AC susceptibility, $\chi'(T)$, [(■) 1 Hz, (○) 17 Hz, (▲) 170 Hz, and (◇) 1 kHz] and $\chi''(T)$, [(□) 1 Hz and (●) 17 Hz] for **FeNi-bi** aligned parallel to the measuring field. The samples were measured with an AC field of 4 G under zero applied DC field.

$\chi''(T)$ component is evidence of an uncompensated moment, which further supports the hysteresis observed at $T = 2$ K in the $M(T)$ data, Figure 6-4. Spin glass behavior in **FeNi-bi** is indicated by the frequency dependence of the $\chi'(T)$ and $\chi''(T)$ peak positions. The peak position of the higher temperature shoulder in the $\chi'(T)$ is difficult to discern unambiguously, but is very similar to the peak at $T_g = 5.4$ K observed for the **FeNi-150** sample at the same frequency (17 Hz). The data for the two samples are compared in Figure 6-10. The lower temperature peak of **FeNi-bi** yields a separate glass temperature at 17 Hz of $T_g = 3.8$ K. An interpretation of this feature will be discussed below. The anisotropy of the DC measurements is reproduced in the $\chi_{ac}(T)$ where the perpendicular susceptibility (not shown) is an order of magnitude less intense than that seen in the parallel orientation.

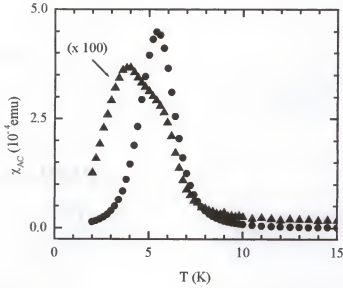


Figure 10. The background corrected AC susceptibility, $\chi'(T)$, measured in 17 Hz for **FeNi-bi** (▲) (scaled $\times 100$) and **FeNi-150** (●). Both samples were aligned parallel to the measuring field. The samples were measured with an AC field of 4 G under zero applied DC field.

The $\chi_{ac}(T)$ data measured at 1 Hz, 17 Hz, 170 Hz, and 1.0 kHz for the parallel orientation of **FeNi-mono** are shown in Figure 6-11. The presence of a $\chi''(T)$ component indicates the presence of an uncompensated moment in the monolayer film, albeit the peak has not clearly formed by $T = 2$ K, and lends support to the weak hysteresis observed in the DC $M(H)$ data at $T = 2$ K. The effect of frequency on the $\chi''(T)$ peak position cannot be unambiguously determined, however a shift in the onset temperature is suggested in the data. The $\chi'(T)$ clearly shows a frequency dependence which again is indicative of spin-glass behavior. The glass temperature $T_g = 2.4$ K extracted from the peak position at 17 Hz is below the glass temperatures of the bilayer and multilayer films. Comparing the magnetic response of the film between two orientations shows a similar magnetic anisotropy to that observed in the χ_{dc} measurements with χ_{ac} an order of

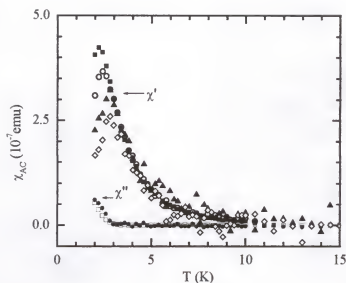


Figure 11. The background corrected AC susceptibility, $\chi'(T)$, [(■) 1 Hz, (○) 17 Hz, (▲) 170 Hz, and (◇) 1 kHz] and $\chi''(T)$, [(□) 1 Hz and (●) 17 Hz] for **FeNi-mono** aligned parallel to the measuring field. The samples were measured with an AC field of 4 G under zero applied DC field.

magnitude larger in the parallel orientation versus the perpendicular orientation (not shown).

Discussion

Magnetic Anisotropy

The magnetic anisotropy of the thin film samples containing the Fe-CN-Ni grid networks provides convincing evidence for the low-dimensional nature of the materials. Even though a crystal-like analysis is not possible, some general conclusions can be made regarding the nature of the anisotropy. The magnetic easy axis clearly has a major vector component oriented parallel to the plane of the substrate surface, i.e. within the plane of the grid network. This anisotropy most likely arises from the spin-orbit coupling of the magnetic moments to the structural anisotropy. The most pronounced anisotropic behavior is observed in the monolayer sample, **FeNi-mono**, which has a ratio of field-

cooled $M_{\parallel} : M_{\perp}$ at $T = 2$ K of *ca.* 22:1. This ratio decreases in the bilayer and 150 bilayer samples to *ca.* 4.6:1 and 3.4:1, respectively. This trend suggests the presence of interlayer coupling between the face-to-face networks within the bilayer region. This exchange is also evidenced by the increase in T_c from 2.4 K in the monolayer film to 5.4 K in the bilayer and multilayer films.

The nature of the bonding interactions between adjacent networks within the bilayer regions remains uncertain. However, a comparison of the magnetic behavior of the bilayer and multilayer samples to those of other 2D metal-cyanide systems may provide some insight. Of particular relevance are the quasi-2D square-grid³⁷⁻⁴⁰ networks constructed from iron(III)hexacyanide and nickel bis(diamine) complexes and the honeycomb^{41-43,210,211} networks constructed from chromium(III)hexacyanide and nickel(cyclam) complexes. In general, these lamellar solids consist of cyanide-bridged two-dimensional sheets separated one from another by a solvent or counterion layer. The exchange within the sheets is ferromagnetic, but when the inter-sheet separation is reduced below *ca.* 10 Å, inter-sheet antiferromagnetic exchange often results leading to an antiferromagnetic ground state.^{43,196,210,211,213,214} Even though the inter-planar distance within the bilayers of the **FeNi-bi** and **FeNi-150** samples are less than 10 Å as evidenced from x-ray diffraction data,²⁰⁵ no metamagnetic behavior is observed in these samples. This suggests that the interaction between face-to-face networks within the bilayer region is predominantly covalent in nature, brought about through bridging of the axial cyanide of the amphiphilic pentacyanoferrate complex to available coordination sites of nickel ions in the adjacent network. This covalent bonding arrangement would favor

ferromagnetic exchange by the same mechanism that promotes ferromagnetism within one network plane.

Spin Glass Behavior

The DC magnetometry studies on each of the three samples yielded M_{fc} and M_{zfc} traces (Figures 6-1, 6-3, and 6-5) with a characteristic “λ” shape that is typically observed in either ferromagnetic or spin glass materials.^{126,218} The films also displayed a hysteresis in their magnetization vs. field plots that are also signs of ferromagnetic order or spin glass behavior. On the other hand, the frequency dependence of the $\chi_{ac}(T)$ data for each of the three samples investigated indicates that these materials are not long-range ordered ferromagnets at low temperature, since such systems would not show a frequency dependence in their susceptibility at or below 1 kHz. Such frequency dependence is typically assigned to either superparamagnets or spin glasses. A spin glass state can be distinguished from a superparamagnet by quantifying the frequency dependence through the ratio ϕ ¹²⁶

$$\phi = \Delta T_f / [(T_f \Delta(\log \omega))] \quad (1)$$

where T_f is the temperature at which the maximum in $\chi'(T)$ occurs, and ΔT_f is the difference in T_f between an initial frequency ω and final frequency ω_f . The values of ϕ obtained for **FeNi-bi** and **FeNi-150** are 0.05 and 0.04, respectively, which fall within the typical range for insulating spin-glasses¹²⁶ and are very similar to those reported by Buschmann^{216,217} for a series of hexacyanomanganate Prussian blue analogues.

A somewhat larger value of $\phi = 0.10$ was obtained for **FeNi-mono** which falls between the extreme case of $\phi = 0.28$ reported for the superparamagnet $\alpha\text{-(Ho}_2\text{O}_3\text{)(B}_2\text{O}_3\text{)}$,

and $\phi \sim 0.005$ for insulating spin-glasses.¹²⁶ Attempts to fit the data to the Arrhenius equation, eq. 2,

$$\ln(\tau/\tau_0) = [E_a/(k_B T)] \quad (2)$$

where τ is the average relaxation time corresponding to the frequency of the AC measurement, and E_a/k_B is the energy barrier to magnetic reversal in an isolated particle, yields a $\tau_0 = 1 \times 10^{-14}$ sec and $E_a/k_B = 70$ K. The value of $\tau_0 = 1 \times 10^{-14}$ sec fall below the range of $1 \times 10^{-11} < \tau_0 < 1 \times 10^{-9}$ predicted for non-interacting ferromagnetic particles²¹⁹ and indicates the presence of inter-particle interactions. The strength of the interaction increases significantly as one progresses to the isolated bilayer and multilayer films where $\tau_0 = 1 \times 10^{-20}$ sec ($E_a/k_B = 170$ K) and $\tau_0 = 1 \times 10^{-30}$ sec ($E_a/k_B = 350$ K), respectively. Therefore, the system may best be described as a progression from moderately interacting ferromagnetic particles in the monolayer to a collective strongly interacting glass-like state in the bilayer and multilayer films.

The two peak profile observed in the $\chi(T)$ data for **FeNi-bi** is unique to the sample and warrants further discussion. Similar dual peak profiles observed in $M[\text{Mn}(\text{CN})_6]$ ($M = \text{Cr}, \text{Mn}$) Prussian blue analogues have been assigned to reentrant spin glass behavior,²¹⁷ however such a characterization here is inappropriate since both peaks show frequency dependence. Therefore neither peak corresponds to an ordered ferromagnetic state. A more likely explanation arises by comparing the $\chi_{ac}(T)$ data for **FeNi-bi** to the $\chi_{ac}(T)$ data for **FeNi-150**, as shown in Figure 6-10. The glass transition temperature is a function of the disorder of a material, with more disordered materials giving lower glass transition temperatures. Analysis by grazing incidence diffraction indicates in-plane coherence lengths of about 6 unit cells. This estimate is an average,

and each bilayer will have some domains that are larger and some smaller, and some areas that are relatively disordered. The two processes observed in $\chi_{ac}(T)$ likely reflect two different sets of domains. Since the bilayers are fabricated using the same process for each sample, the **FeNi-bi** and **FeNi-150** should possess essentially the same degree of structural disorder within each bilayer. Therefore the absence of a low temperature peak in the **FeNi-150** sample may be due to interactions that are present in the multilayer sample but absent in the single bilayer, such as long-distance dipolar exchange forces. The dipolar exchange between layers could provide an extra interaction pathway that ties the less coherent two-dimensional domains to the larger ones. The lack of similar dipolar forces in the isolated bilayer sample results in each of these domains adopting a unique glass transition temperature. Similar dipolar forces have been shown to operate over relatively long distances (~ 35 Å inter-bilayer spacing) in other lamellar ferromagnetic materials.⁴⁴

Conclusions

The interfacial assembly of a two-dimensional Fe-CN-Ni grid network in combination with the controlled deposition capability of the Langmuir-Blodgett technique yields novel low-dimensional thin films where the effects of interlayer interactions on magnetic properties can systematically be studied. The results show a variation in magnetic behavior upon progressing from a two-dimensional monolayer to a two-dimensional bilayer to a multilayer film. The progressive changes demonstrate the influences of dimensionality and interlayer coupling on the magnetic behavior in molecule-based materials. All of the materials studied show highly anisotropic magnetic behavior, with the highest anisotropy observed in the isolated monolayer film. Each

system also shows the presence of ferromagnetic domains at low temperature. The bilayer and multilayer assemblies show clear spin-glass behavior whereas the isolated monolayer film may be just as well described as a moderately interacting superparamagnetic system.

CHAPTER 7

SEQUENTIAL ASSEMBLY OF HOMOGENEOUS MAGNETIC PRUSSIAN BLUE FILMS ON TEMPLATED SURFACES

Introduction

Prussian blue is a mixed-valent cubic iron-cyanide polymer of approximate composition $\text{Fe(III)}_4[\text{Fe(II)(CN)}_6]_3 \cdot 14\text{H}_2\text{O}$.¹⁹¹ The material possesses an intense metal-to-metal charge transfer absorbance band that gives it a deep blue color. The intense color of the material and the dependence of the color on oxidation state have led to numerous investigations into applications involving electrochromic materials.²²⁰⁻²²³ In addition, the structure of the material typically includes defects due to incomplete displacement of coordinated water on the bridged metal sites. These defects lead to a charge imbalance that is compensated for by the incorporation of alkali cations into the structure.¹⁹⁵ As such, Prussian blue and related compounds have also been investigated for potential applications in cation sensors.²²⁴⁻²²⁷

The Prussian blue structure is not limited to iron and the compositions can be varied to include numerous combinations of transition metal ions in various oxidation states. The incorporation of various mixtures of transition metal ions and hexacyanides provides an opportunity to tune the physical properties of the resulting solids. One particular property of these Prussian blue "hybrids" that has generated a great deal of interest is their magnetic behavior.^{13,195} The synthetic versatility of Prussian blues coupled with the ability of the bridging cyanide ligand to efficiently mediate magnetic

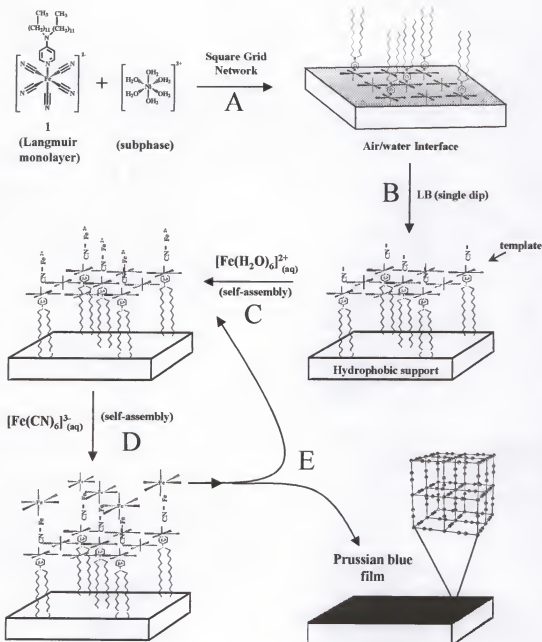
exchange has led to several high T_c mixed-spin molecular based magnetic systems,^{52,192,228} including some which order well above room temperature.^{51,173,174,215}

Also of interest is the photo-induced magnetization in Fe-Co Prussian blue analogues.^{207,229-231}

Much of the excitement over the magnetic behavior of the Prussian blue family of materials stems from the fact that they are a molecular-based class of materials. This can be viewed as an advantage over metal oxides since metal cyanides can be synthesized under mild synthetic conditions and easily isolated. Unlike oxides, which are typically black, most metal cyanides are colored species and thereby possess the potential to form transparent magnetic films.⁵⁶

Many of the aforementioned properties of Prussian blues make them attractive candidates for uses in materials spanning a wide range of potential applications. Most of these applications would require incorporating these functionally diverse materials into homogeneous thin films, and several methods aimed at depositing Prussian blue analogs onto solid supports have been reported. These methods include adsorption on sol-gel films,²³² sequential deposition onto polyelectrolyte coated surfaces,²²⁴ adsorption at Langmuir-Blodgett films.^{64,233} The most commonly applied technique is the electrochemical deposition of the materials on electrode surfaces,^{54,56,227,234-239} The morphologies of the respective films vary from disperse collections of crystallites to fairly continuous amorphous coatings.

Our approach to forming thin homogeneous Prussian blue films is outlined in Scheme 7-1. The method is based on the sequential deposition procedure that has previously been used with polyelectrolyte-modified surfaces. However, our method



Scheme 7-1. Sequential deposition of Prussian blue begins by first templating a hydrophobic surface with one monolayer of a two-dimensional Fe-CN-Ni network preformed at the air-water interface (A). The monolayer film is transferred by the LB technique and removed from the trough after a single transfer (once down). The templated surface now consists of what is essentially one layer of the Prussian blue structure (B). Subsequent immersion in an aqueous solution of the appropriate metal ion (C) followed by immersion in an aqueous solution of a hexacyanometalate (D) results in the growth of a thin film of the polymeric metal cyanide. The cycle is repeated as necessary (typically 5-10 cycles) to achieve a homogeneous film (E).

differs in that the hydrophobic surface is first templated with a two-dimensional iron-nickel-cyanide grid network. The template layer is prepared at the air-water interface of a Langmuir-Blodgett trough by spreading a monolayer of an amphiphilic pentacyanoferrate(III) complex on a subphase containing aqueous nickel (II) ions. The two-dimensional grid network which forms has been well characterized and is, in essence, one layer of the cubic Prussian blue cell.²⁰⁵ The reacted film can then be transferred onto a hydrophobic support by the Langmuir-Blodgett technique. The film is only transferred in the down direction leaving the surface of the substrate terminated with the reactive cyanides from the pentacyanoferrate complex which are ideally organized into a 2D face-centered grid motif. As such, the surface is well matched for subsequent epitaxial deposition of the bulk cubic solid via the sequential adsorption of first aqueous metal ions, then hexacyano metal ions. Surface morphology investigations using AFM and SEM indicate that the surface coverage is exceptional, and magnetic measurements reveal that the magnetic properties of the solid-state materials are reproduced in the thin film structures.

Experimental

Materials. Reagent grade FeCl_2 , $\text{Ni}(\text{NO}_3)_2 \cdot 6\text{H}_2\text{O}$, CrCl_2 , $\text{K}_3\text{Fe}(\text{CN})_6$, $\text{K}_3\text{Cr}(\text{CN})_6$, $\text{Ag}(\text{NO}_3)$, and CsI were purchased from Aldrich (Milwaukee, WI) and used without further purification. The $\text{Cs}_x\text{K}_{(1-x)}[\text{Cr}(\text{CN})_6]$ complex was prepared as follows. To 25 mL of an aqueous solution containing 1 g (3.1 mmol) $\text{K}_3\text{Cr}(\text{CN})_6$ was added 25 mL of an aqueous solution containing 3.3 equivalents (10.0 mmol) of $\text{Ag}(\text{NO}_3)$. The precipitated $\text{Ag}_3\text{Cr}(\text{CN})_6$ was collected by filtration, washed thoroughly with water, and suspended in a 20 mL aqueous solution of 3.2 g (12.4 mmol) CsI . The solution was stirred vigorously

at room temperature for 2 hours and the AgI that formed was removed by filtration through Celite. Addition of 50 mL absolute ethanol to the filtrate precipitated the $\text{Cs}_3[\text{Cr}(\text{CN})_6]$ complex salt, which was collected by filtration and subsequently dried under vacuum in a desiccator (yield 1.4 g). The complex gave a UV-Vis and IR spectra identical to the $\text{K}_3\text{Cr}(\text{CN})_6$ starting material. The amphiphilic complex bis(tetramethylammonium) pentacyano(4-didodecylaminopyridine)ferrate(III) $\cdot 6\text{H}_2\text{O}$ (1) was prepared as previously described.²⁰⁵

Instrumentation. UV-Vis spectra were obtained on a Hewlett-Packard 8452A diode array spectrophotometer. The LB films (template monolayers) were prepared by using a KSV Instruments 5000 trough modified to operate with double barriers. The surface pressure was measured with a filter paper Wilhelmy plate suspended from a KSV microbalance. Subphase solutions were prepared from 17.8-18.1 M Ω cm water delivered with a Barnstead E-pure system. Magnetization measurements were performed on a Quantum Design MPMS SQUID magnetometer. Grazing incidence x-ray diffraction (GIXD) experiments using synchrotron radiation were performed at the Advanced Photon Source, Argonne, IL, at the Materials Research Collaborative Access Team beamline (sector 10).⁷⁶ The GIXD scans were performed on films prepared on glass slides. The samples were positioned in the center of an 8-circle Huber goniometer and oriented at an angle of 0.13 degrees relative to the incident beam. The incident beam was collimated to 200 microns high by 1500 microns wide and tuned to a wavelength of 1.254 Å. Diffracted intensity in the xy plane was measured using a NaI scintillation counter mounted on the Huber goniometer. The diffracted signal was collimated prior to the detector using Soller slits giving an experimental resolution on the order of 0.015 Å⁻¹.

Film preparation. AFM, SEM, UV-Vis, and GIXD samples were prepared on glass slides that were purchased from Buehler Ltd (Lake Bluff, IL). Samples for SQUID investigations were prepared on Mylar (Dupont) substrates cleaned prior to use with absolute ethanol. The glass substrates were cleaned using the RCA procedure¹⁷⁸ and made hydrophobic by deposition of a monolayer of OTS.^{179,180}

Formation of the template layer. The amphiphilic iron complex **1** was spread from a chloroform solution onto surface of a subphase 1 g/L in $\text{Ni}(\text{NO}_3)_2 \cdot 6\text{H}_2\text{O}$. All template monolayer films of the nickel-iron-cyanide network were transferred with one downstroke onto hydrophobic substrates at a surface pressure of 25 mN/m. The average transfer ratios were >90%.

Formation of the Prussian blue films. The bulk Prussian blue film is assembled onto the templated substrate by a sequential deposition process. After transfer of the template layer by the LB method, the substrate was removed from the trough and rinsed briefly with water. The substrate was then immersed in the appropriate 0.01 M aqueous FeCl_2 , $\text{Ni}(\text{NO}_3)_2 \cdot 6\text{H}_2\text{O}$ or CrCl_2 solution for ~ 1 min then rinsed twice by brief immersion in two separate beakers of nanopure water, then once by immersion in methanol, and finally dried under a stream of nitrogen before the process was repeated with an aqueous solution 0.01 M in the appropriate $\text{K}_3\text{Fe}(\text{CN})_6$ or $\text{K}_3\text{Cr}(\text{CN})_6$ complex salt. The $\text{K}_x\text{Cr}^{\text{II}}_{(1-x)}[\text{Cr}^{\text{III}}(\text{CN})_6]$ film was prepared under a N_2 atmosphere with N_2 -purged solutions. A $\text{Cs}_x\text{K}_{(1-x)}[\text{Cr}(\text{CN})_6]$ solution 10 mM in CsNO_3 and was used in the synthesis of the $\text{Cs}_x\text{Ni}^{\text{II}}_{(1-x)}[\text{Cr}^{\text{III}}(\text{CN})_6]$ film. One deposition cycle is comprised of one immersion, subsequently, in each of the metal ion solutions.

Results and Discussion

Film Deposition

Our method for preparing thin metal cyanide films is outlined in Scheme 7-1. The schematic is specific to the preparation of a Prussian blue film, but the method itself is general and various combinations of aqueous metal salts and hexacyano complexes can be substituted for the $\text{Fe}^{2+}_{(\text{aq})}$ and $[\text{Fe}(\text{CN})_6]^{3-}$ ions depicted in Scheme 7-1. Central to the concept is the preparation of the template layer that is formed by the reaction of a Langmuir monolayer of an amphiphilic pentacyanoferrate(III) complex (**1**) with aqueous Ni^{2+} ions in the subphase. Nickel ions are used in the template layer since these ions have been shown to form a structurally coherent two-dimensional grid network when reacted with **1**.²⁰⁵ Transfer of the grid network to a hydrophobic surface by the Langmuir-Blodgett technique is terminated with the substrate immersed in the subphase and subsequently removed, then cycled through solutions of the appropriate metal complex building blocks. In this way, a thin film of the bulk solid is deposited on the surface.

Two AFM images, typical of the films prepared by Scheme 7-1, are shown in Figure 1a and 1b. Figure 1a is an AFM image of a $\text{Ni}[\text{Cr}^{\text{III}}(\text{CN})_6]$ film after 3 deposition cycles, and Figure 1b is an AFM image of an $\text{Fe}^{\text{III}}[\text{Fe}^{\text{II}}(\text{CN})_6]$ film after 5 deposition cycles. Both films were prepared on glass substrates made hydrophobic by a monolayer of octadecyltrichlorosilane. Both images show complete surface coverage over the $100\text{ }\mu\text{m}^2$ area investigated. The darker brown background in both images was verified as the metal-cyanide film by comparison to other images taken at defect sights. The lighter regions in both films are due to smaller crystallites on the surface and indicate that film growth likely proceeds through domain formations and not via a layer per cycle mechanism. This conclusion is also supported by the $\sim 30\text{ nm}$ average thickness of the

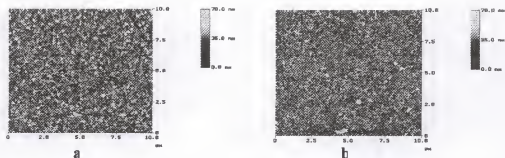


Figure 7-1. AFM images of (a) a $\text{Ni}[\text{Cr}^{\text{III}}(\text{CN})_6]$ film after 3 deposition cycles, and (b) an $\text{Fe}^{\text{III}}[\text{Fe}^{\text{II}}(\text{CN})_6]$ film after 5 deposition cycles. Both films were prepared on glass substrates as described in the text.

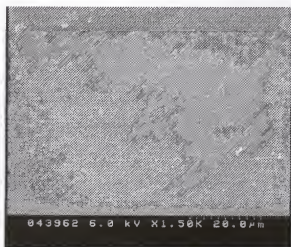


Figure 7-2. An SEM image taken of an $\text{Fe}^{\text{III}}[\text{Fe}^{\text{II}}(\text{CN})_6]$ film after 10 cycles. The film was prepared on a glass substrate as described in the text.

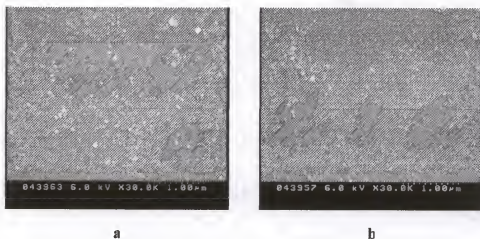


Figure 7-3 SEM images of (A) an $\text{Fe}^{\text{III}}[\text{Fe}^{\text{II}}(\text{CN})_6]$ film after 10 cycles and (B) a $\text{Ni}[\text{Fe}^{\text{III}}(\text{CN})_6]$ film after 10 deposition cycles. Both films were prepared on glass substrates as described in the text.

films, which is higher than, would be expected for cubic particles with a 1 nm unit cell length. Further evidence that the surface coverage is complete in these films is provided by the SEM images taken of the materials. An SEM image taken of an $\text{Fe}^{\text{III}}[\text{Fe}^{\text{II}}(\text{CN})_6]$ film after 10 cycles is shown in Figure 7-2. The abrasion in the upper left corner clearly shows the substrate below a Prussian blue film that is continuous over the remaining $400 \mu\text{m}^2$. Similar results were obtained on the other metal-cyanide films. Images taken at higher magnification of the same $\text{Fe}^{\text{III}}[\text{Fe}^{\text{II}}(\text{CN})_6]$ film and of a different $\text{Ni}[\text{Fe}^{\text{III}}(\text{CN})_6]$ film after 10 deposition cycles are shown in Figures 7-3a and b, respectively. The images are similar to those obtained with AFM (Figure 7-1) and show the presence of smaller crystallites above a continuous underlying film.

The surface morphology studies discussed above show that the assembly process depicted in Scheme 7-1 is somewhat idealized with respect to the mechanism of film growth. The film is not deposited as one unique layer per cycle (one cycle being steps C

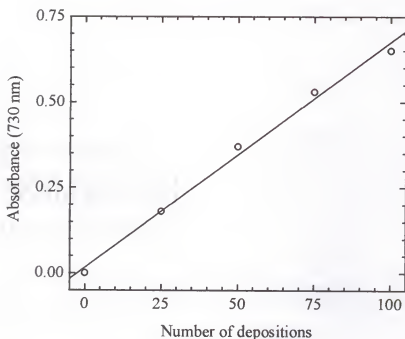


Figure 7-4. Linear fit to the absorbance at 730 nm versus deposition cycle for the $\text{Fe}^{\text{III}}[\text{Fe}^{\text{II}}(\text{CN})_6]$ film through 100 cycles. The film was prepared on a glass substrate as described in the text.

and D) but through a mixture of domain formation and multiple deposits per cycle that lead to a complete surface coverage, albeit with variations in film thickness. Even so, the growth of the film is quite regular in quantity as evidenced by the near linear increase in absorbance versus deposition cycle for the $\text{Fe}^{\text{III}}[\text{Fe}^{\text{II}}(\text{CN})_6]$ film through 100 cycles, as indicated in Figure 7-4. Furthermore, the transparency of the resulting blue film provides further evidence of structural homogeneity and small grain size in the material (Figure 7-5).

Structural characterization of the self-assembled films was performed using grazing incidence x-ray diffraction from a synchrotron source.²⁰⁵ The diffraction patterns obtained for a $\text{Fe}^{\text{III}}[\text{Fe}^{\text{II}}(\text{CN})_6]$ film after 100 deposition cycles and a $\text{Ni}^{\text{II}}[\text{Cr}^{\text{III}}(\text{CN})_6]$ film



Figure 7-5. A photograph demonstrating the transparency of an $\text{Fe}^{\text{III}}[\text{Fe}^{\text{II}}(\text{CN})_6]$ film after 100 deposition cycles. The film was prepared on a glass substrate as described in the text.

after 20 cycles are shown in Figure 7-6 and Figure 7-7, respectively. Both diffraction patterns can be indexed to a face-centered cubic cell with $a = 10.26 \text{ \AA}$ for the $\text{Fe}^{\text{III}}[\text{Fe}^{\text{II}}(\text{CN})_6]$ structure, and $a = 10.48 \text{ \AA}$ for the $\text{Ni}^{\text{II}}[\text{Cr}^{\text{III}}(\text{CN})_6]$ structure. Both values of the unit cell parameter are within the range typically observed for Prussian blues compounds.^{13,195,209,234} Analysis of the (200) peak widths in each of the diffraction patterns by application of the Scherrer method¹⁴⁷ yielded average structural coherence lengths of 190 \AA and 150 \AA for the $\text{Fe}^{\text{III}}[\text{Fe}^{\text{II}}(\text{CN})_6]$ and $\text{Ni}^{\text{II}}[\text{Cr}^{\text{III}}(\text{CN})_6]$ films, respectively.

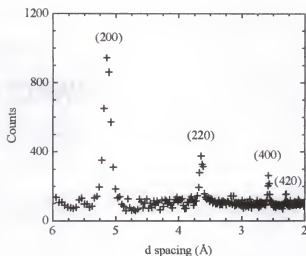


Figure 7-6. The GIXD pattern obtained for an $\text{Fe}^{\text{III}}[\text{Fe}^{\text{II}}(\text{CN})_6]$ film after 100 deposition cycles. The Miller indices are derived from a cubic unit cell with $a = 10.26 \text{ \AA}$.

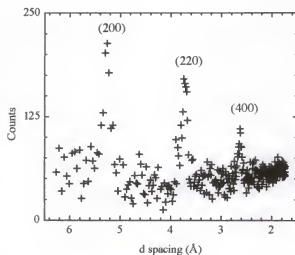


Figure 7-7. The GIXD pattern obtained for an $\text{Ni}^{\text{II}}[\text{Cr}^{\text{III}}(\text{CN})_6]$ film after 20 deposition cycles. The Miller indices are derived from a cubic unit cell with $a = 10.48 \text{ \AA}$.

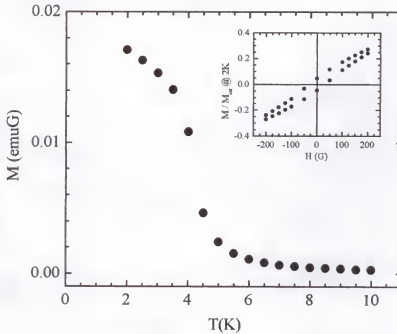


Figure 7-8. The field-cooled magnetization in 20 G as a function of temperature and hysteresis loop (inset) for a 10 cm^2 $\text{K}_x\text{FeIII}_{(1-x)}[\text{FeII}(\text{CN})_6]$ film after 100 deposition cycles.

Magnetism

The magnetic properties for each of the films prepared on Mylar substrates were measured as a function of temperature and field. The results for the 10 cm^2 $\text{K}_x\text{Fe}^{\text{III}}_{(1-x)}[\text{Fe}^{\text{II}}(\text{CN})_6]$ film measuring after 100 deposition cycles are shown in Figure 7-8. The solid-state analogue is a known ferromagnet below a $T_c = 5.6 \text{ K}^{240}$ and similar results are observed in the current thin film sample. The field-cooled magnetization versus temperature, $M_{fc}(T)$, shows a rapid rise at $T_c = 5 \text{ K}$ and the material displays a clear hysteresis at $T = 2 \text{ K}$ in the magnetization versus field, $M(H)$, plot with a coercive field (H_c) of 30 G (Figure 7-8 inset). Both behaviors are consistent with the presence of ferromagnetic order in film.

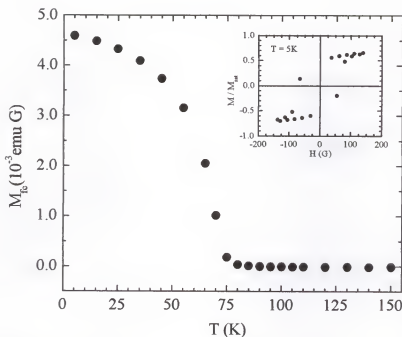


Figure 7-9. The field-cooled magnetization in 20 G as a function of temperature and hysteresis loop (inset) for an $8 \text{ cm}^2 \text{ Cs}_x\text{Ni}_{(1-x)}[\text{Cr}^{\text{III}}(\text{CN})_6]$ film after 20 deposition cycles.

The $M_{fc}(T)$ and $M(H)$ data for a $8 \text{ cm}^2 \text{ Cs}_x\text{Ni}_{(1-x)}^{\text{II}}[\text{Cr}^{\text{III}}(\text{CN})_6]$ film after 20 deposition cycles is shown in Figure 7-9. The ferromagnetic ordering temperature, $T_c = 75 \text{ K}$, extracted from the $M_{fc}(T)$ data is slightly lower than the $T_c = 90 \text{ K}$ reported for the bulk solid.¹⁶⁹ Ordering temperatures in Prussian blue analogues $\text{C}_x\text{M}^{\text{A}}_{(1-x)}[\text{M}^{\text{B}}(\text{CN})_6]$ are known to be sensitive to the ratio of M^{A} to M^{B} and this ratio is often affected by the identity of the counterion C.¹⁹⁵ Since the structural coherence of the film was confirmed by GIXD, the lower ordering temperature observed in the film most likely reflects a lower Ni:Cr ratio in the film relative to the solid-state material. The material displays a clear hysteresis at 5 K with an H_c of 70 G and a remnant magnetization (M_{rem}) 50% of the saturation value. Both of these values are nearly identical to those reported by Gadet for the solid analogue.¹⁹⁵

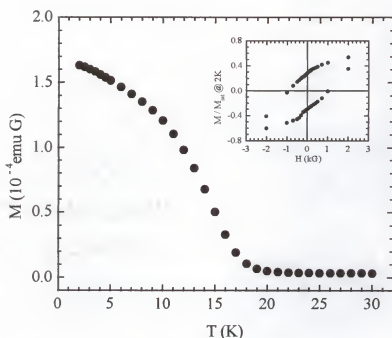


Figure 7-10. The field-cooled magnetization in 20 G as a function of temperature and hysteresis loop (inset) for a 6 cm² K_xNi^{II}_(1-x)[Fe^{III}(CN)₆] film after 10 deposition cycles.

Magnetic measurements were also undertaken on a 6 cm² K_xNi^{II}_(1-x)[Fe^{III}(CN)₆] film after 10 deposition cycles. The results are shown in Figure 7-10. The $M_{fc}(T)$ data show a transition to a ferromagnetic state at $T_c = 18$ K. This is lower than the $T_c = 23.6$ K reported for the analogous solid.¹⁹³ Once again, the lower T_c in the film relative to the solid most likely results from a slightly lower Ni : Fe ratio in the material.¹⁹⁵ The hysteresis loop measured at $T = 2$ K for the material shows a M_{rem} which is 30% of the saturation value and a relatively large $H_c = 1000$ G. The magnitude of the coercive field is less than half the $H_c = 2500$ G reported for the solid¹⁹³ and may reflect an improved structural coherence in the thin film sample.

Higher T_c films are obtained when the K_xCr^{II}_(1-x)[Cr^{III}(CN)₆] compound is assembled on the surface. The K_xCr^{II}_(1-x)[Cr^{III}(CN)₆] family of materials are known

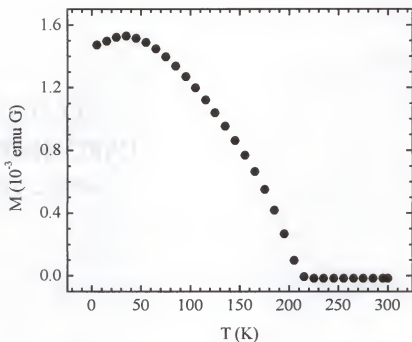


Figure 7-11. The field-cooled magnetization in 20 G as a function of temperature and hysteresis loop (inset) for a 7 cm² K_xCr^{II}_(1-x)[Cr^{III}(CN)₆] film after 40 deposition cycles.

ferrimagnets with $150 \text{ K} < T_c < 270 \text{ K}$ depending on the Cr^{II} : Cr^{III} ratio.^{52,54,233} The higher T_c 's result from the cyanide mediated antiferromagnetic coupling between adjacent metal sites. The $M_{fc}(T)$ for a 7 cm² K_xCr^{II}_(1-x)[Cr^{III}(CN)₆] deposited film after 40 deposition cycles is shown in Figure 7-11. The data show the onset of long-range order at a $T_c = 215 \text{ K}$ which is well within the reported range for K_xCr^{II}_(1-x)[Cr^{III}(CN)₆] compounds.^{52,54,233} The hysteresis loop measured at 10 K showed a very weak $H_c \sim 10 \text{ G}$. The small value of H_c suggests a significant oxidation of the Cr^{II} species in the film, as a higher Cr^{III} content has been shown to greatly reduce the value of the coercive field in chromium cyanides.²³³

Conclusions

A method for the deposition of bulk Prussian blues as thin homogenous films using an LB deposited monolayer of an Fe-CN-Ni two-dimensional grid network preformed at the air-water interface as a template layer has been demonstrated. The procedure is applicable to hydrophobic surfaces and thus compliments the often-used electrochemical methods that take place at conducting surfaces. The technique yields films with virtually complete surface coverage as evidenced by AFM and SEM. Application of the synthetic procedure yielded magnetic films with properties comparable to their solid-state analogues. The results demonstrate a potential application of interfacially assembled inorganic networks as templates for the epitaxial growth of thin solid films.

CHAPTER 8

INVESTIGATIONS INTO THE INTERFACIAL ASSEMBLY OF LINEAR CHAIN AND 2D HEXAGONAL NETWORKS

Introduction

The linear cyanide bridge is a versatile building block in supermolecular chemistry. When used in the form of simple octahedral hexacyano complexes bridged through other octahedral complexes, the inherent 90 degree bond angles lead to the cubic Prussian blue structures.¹³ Additionally, the carbon and nitrogen end of the ligand have different ligand field strengths. This can result in the carbon-bound complex adopting a tetrahedral or square planar geometry whereas the nitrogen bound complex remains octahedral. The bridged networks then contain a mixture of site symmetries that subsequently result in networks other than simple cubic networks observed in the Prussian blue materials. This synthetic approach has been exploited in some cadmium cyanides where the clathration of solvent molecules leads to porous solids similar to zeolites.²⁴¹⁻²⁴³ Lower symmetry metal cyanides such as the square planar $[\text{Ni}(\text{CN})_4]^{2-}$ can also be bridged through octahedral complexes yielding planar networks.²⁴⁴⁻²⁴⁶

A different and far more versatile synthetic strategy employed in supermolecular cyanide-bridged systems is the use of "blocking ligands" on one or both of the complex building blocks. The blocking ligands effectively lower the symmetry of the system and can prevent the uninhibited growth of the polymer through three dimensions. Some of

the blocking ligand that have been used to date include bidentate diammines and bipyridines, tridentate and tetradentate cyclic amines, and planar conjugated systems such as salen and terpyridine. The resulting networks vary from “zero”-dimensional clusters to linear chains to two-dimensional arrays.^{18,20,32,196,211,212}

The successful preparation of square-grid networks through the interface directed assembly of an amphiphilic pentacyanoferrate complex with octahedral Ni^{2+} , Co^{2+} , and Mn^{2+} ions as described in the previous chapters demonstrates the utility of an air-water interface as a structure directing entity in the formation of low dimensional inorganic solids. This same technique, when used in conjunction with complexes having various blocking ligands, may allow for the assembly of other networks with different structural motifs. With this goal in mind, two novel amphiphilic complexes possessing different symmetries were reacted at the air-water interface (Figure 8-1). The first complex discussed is an amphiphilic Fe(III) terpyridine complex that acts as a T-shaped building block. As shown in Scheme 8-1, the symmetry of the complex is well suited for the assembly of a linear chain polymer if reacted at the air-water interface with a linear bridging unit such as $[\text{Ag}(\text{CN})_2]^-$ dissolved in the subphase. The feasibility of the approach has been demonstrated by Woodward et al who have recently reported the crystal structure of a $\text{Ni}(\text{terpyridine})\text{Ni}(\text{CN})_4$ linear chain polymer.²⁴⁷

The other system reported herein involves the reaction of an amphiphilic cyclic-amine nickel(II) complex *Ni(cyclam)* with nickel tetracyanide and chromium(III) hexacyanide at the air-water interface. Similar reactions in solution with non-amphiphilic nickel cyclam complexes have resulted in linear chains^{32,248} with $\text{Ni}(\text{CN})_4^{2-}$ and two-dimensional “honeycomb” hexagonal networks with $\text{Cr}(\text{CN})_6^{3-}$ (Figure 8-2).^{41-43,211}

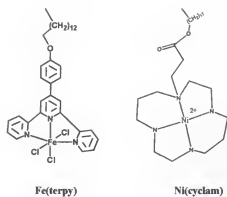


Figure 8-1. Structures of the amphiphilic complexes Fe(terpy) and Ni(cyclam) .

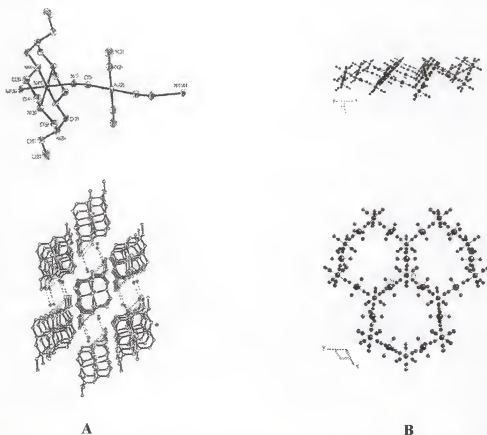
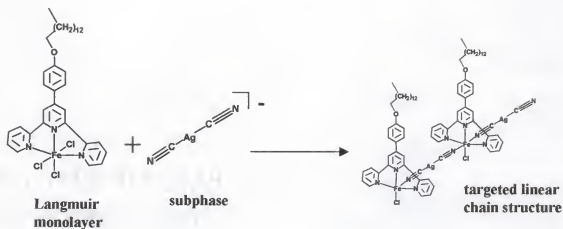


Figure 8-2. Reported structures for the product of reactions with Ni(cyclam) complexes. **A)** linear chain incorporating the Ni(CN)_4^{2-} complex, (from reference 213) **B)** two dimensional honeycomb network incorporating Cr(CN)_6^{3-} (from reference 247).



Scheme 8-1. Strategy for the formation of a linear chain polymer at the air-water interface.

Experimental

Instrumentation. The LB films were prepared by using a KSV Instruments 5000 trough modified to operate with double barriers. The surface pressure was measured with a filter paper Wilhelmy plate suspended from a KSV microbalance. Subphase solutions were prepared from 17.8–18.1 M Ω cm water delivered with a Barnstead Epure system. Magnetization measurements were performed on a Quantum Design MPMS SQUID magnetometer. All NMR spectra were obtained on a Varian VXR-300 spectrometer. The characteristic solvent peaks were used as reference values. Elemental analyses were performed by the University of Florida Spectroscopic Services laboratory. Melting points were obtained on a Thomas-Hoover Capillary melting point apparatus and are uncorrected. The FT-IR spectra as KBr pellets (solids) or on silicon ATR crystals (films) were recorded on a Mattson Instruments (Madison, WI) Research Series-1 FTIR spectrometer with a deuterated triglycine sulfate (DTGS) detector. Grazing incidence x-ray diffraction experiments were performed at the Materials Research Collaborative

Access Team (MRCAT) beamline (sector 10), Argonne National Laboratory, Argonne, IL. The experimental setup has been described previously.^{146,205} For the Langmuir monolayer diffraction experiments (multilayer LB films), a $\lambda = 1.254 \text{ \AA}$ x-ray beam of dimensions $200 \text{ }\mu\text{m}$ (height) \times $2000 \text{ }\mu\text{m}$ (width) was made incident on the water surface (glass surface) at an angle of 1.8 mrad .

Film preparation. The multilayer LB films, 30 bilayers per side, were prepared on glass microscope slides made hydrophobic by a monolayer of OTS. One equivalent of octadecanol was mixed with the *Fe(terpy)* complex to aid in the transfer of the film over the silver cyanide subphase. The films were transferred at a surface pressure of 30 mN/m at room temperature.

Synthesis. All starting materials were purchased from Aldrich (Milwaukee, WI) and used as received except for the 4-hydroxybenzaldehyde which was recrystallized from water prior to use. The amphiphilic nickel perchlorate complex containing the ligand [1-(propanoic acid, stearyl ester)-1,4,8,11-tetraazacyclotetradecane] (*Ni(cyclam)*) was supplied by Dr. Christophe Mingotaud (Centre de Recherche Paul Pascal, PESSAC, France). The following procedure is adapted from the method reported by Constable for the synthesis of 4'-phenyl-2,2'-6',2''-terpyridine.²⁴⁹ The method of Constable involves the condensation reaction of benzaldehyde with two equivalents of 2-acetylpyridine under basic conditions to form a diketone intermediate, which can be further reacted with excess ammonium acetate to afford the final 4-phenylterpyridine. To form the alkylated 4-phenylterpyridine, the benzaldehyde is replaced in the synthesis with 4-tetradecyloxybenzaldehyde.

4-tetradecyloxybenzaldehyde. The 4-tetradecyloxybenzaldehyde was prepared from a solution containing 8.4 g (30 mmol) 1-bromotetradecane and 3.66 g (30 mmol) 4-hydroxybenzaldehyde in dimethoxyethane under reflux over 4.5 g (excess) potassium carbonate for 12 hrs. The solvent was removed under reduced pressure and 200 mL water added to remaining mixture. The product was removed by extraction with 150 mL diethyl ether. After drying over anhydrous magnesium sulfate, the ether solution was added to 150 mL acetonitrile and concentrated under a stream of nitrogen. The precipitate was filtered and used without further purification [(yield 7.4 g crude) (^1H NMR(CDCl_3), ppm: 9.88 (s) 1H, 7.82 (d) 2H, 7.00 (d) 2H, 4.03 (t) 2H, 1.81 (m) 2H, 1.46-1.26 (m) 24H, 0.88 (t) 3H].

4'-(4-tetradecyloxyphenyl)-2,2'-6',2''-terpyridine. To 70 mL of an ethanolic solution containing 2.24 g (40 mmol) KOH and 5.4 g 4-tetradecyloxybenzaldehyde at 35°C was added drop wise 4.6 g (38 mmol) 2-acetylpyridine in 10 mL ethanol. The solution turned deep red after several minutes and the solution was left to stir for 24 hrs. The white precipitate that formed was filtered and washed with ethanol until the washing were colorless. The solid was purified by recrystallization from 100 mL 3:1 EtOH:THF and dried under vacuum. (yield 5.4 g) The product at this stage is a diketone intermediate²⁴⁹ (FT-IR 1695 cm^{-1}), which is converted to the terpyridine by refluxing 8 hrs in air in an 80:20 EtOH:THF solution containing 8 g (excess) ammonium acetate. The dark green solution, when cooled in the freezer, precipitates the crude product terpyridine. Recrystallization for EtOH/THF yields the pure yellow product[(yield 2.75 g mp 94-96°C, calc.(obs.) for $\text{C}_{35}\text{H}_{43}\text{N}_3\text{O}$: %C 80.57 (80.42) %H 8.31 (8.54) %N 8.05 (8.04); ^1H NMR(CDCl_3), ppm: 8.68 (m) 6H, 7.81 (m) 4H, 7.30 (m) 2H, 7.00 (m) 2H,

3.98 (t) 2H, 1.81 (m) 2H, 1.46-1.26 (m) 24H, 0.88 (t) 3H]. The product is best stored in the dark since discoloration occurs with prolonged exposure to light.

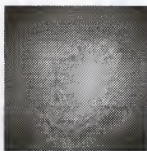
(4'-(4-tetradecyloxyphenyl)-2,2'-6',2''-terpyridine)iron(III)trichloride
(*Fe(terpy)*). The complex was prepared by addition of a 10 mL THF solution containing 650 mg (1mmol) to a 10 mL THF solution containing 850 mg (5 mmol) anhydrous FeCl_3 . The solution was stirred for 2-3 min and added to 100 mL of cold methanol containing excess tetraethylammonium chloride. The product precipitated as a yellow solid that was then filtered, washed with cold methanol and dried under vacuum [yield 450 mg, calc (obs) for $\text{C}_{35}\text{H}_{43}\text{N}_3\text{OFeCl}_3$: %C 61.47 (61.66) %H 6.34 (6.31) %N 6.14 (6.01)].

Results and Discussion

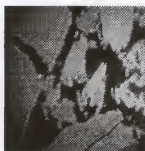
Brewster Angle Microscopy

Brewster angle microscopy (BAM) is an experimental technique that can give a macroscopic picture of an amphiphile's behavior on the water surface. The technique exploits the change in index of refraction that occurs at the interface of a thin film and the water surface by monitoring the reflected intensity of a laser source incident on the water surface at the critical angle (Brewster angle). Regions of a Langmuir monolayer will have variations in reflectivity where there are variations in film density, i.e. where there are variations in the index of refraction. Areas in the monolayer where the film density is low will reflect little light and appear black whereas areas of film with a higher density will appear bright.

The BAM images taken of the *Fe(terpy)* film taken at zero surface pressure over a pure water subphase and a 0.5 mM $\text{Ag}(\text{CN})_2^-$ subphase are shown in Figure 8-3. The image over pure water is brighter than expected for an amphiphile in an uncompressed



$\pi = 0$
pure water



$\pi = 0$
0.5 mM

Figure 8-3. BAM images taken for *Fe(terpy)* monolayers over pure water (left) and over a 0.5 mM KAg(CN)_2 subphase.

state and indicates that the complex is most likely aggregated at low pressure. The apparent aggregation of the complex could result through π - π interactions between the terpyridine ligands of adjacent complexes. The image obtained for the same complex over a Ag(CN)_2^- subphase shows the film in a highly compressed, rigid state. The small jagged domains are noticeably different than the more homogeneous image seen on pure water and are a clear indication that the amphiphile has condensed into a solid film.

A BAM image taken of the *Ni(cyclam)* complex at zero surface pressure over a 1 mM NaNO_3 subphase is shown in Figure 8-4. The film spreads well and is very dynamic at low pressure, showing a liquid phase in the monolayer. The behavior of the monolayer is quite different when spread over a subphase containing either Ni(CN)_4^- or Cr(CN)_6^{3-} ions. As shown in Figure 8-4, both films over metal cyanide solutions consist of highly condensed domains with rather sharp well-defined boundaries. This behavior is consistent with a condensation reaction between the *Ni(cyclam)* amphiphile and the aqueous Ni(CN)_4^- and Cr(CN)_6^{3-} ions.

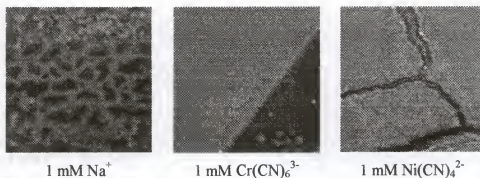


Figure 8-4. BAM images taken for *Ni(cyclam)* monolayers over (left) 1 mM Na^+ , (center) 1 mM Cr(CN)_6^{3-} , and (right) 1 mM Ni(CN)_4^{2-} subphases.

Infrared Spectroscopy

The BAM images for both the *Fe(terpy)* and *Ni(cyclam)* systems indicate a reaction of the amphiphiles with the aqueous metal cyanide complexes. To obtain further evidence for cyanide bridge formation in the materials, the films were transferred to silicon ATR crystals for infrared spectroscopy. The FT-IR spectrum for the *Fe(terpy)* film after reaction with Ag(CN)_2^- is compared to the FT-IR spectrum taken of KAg(CN)_2 as a KBr pellet in Figure 8-5. The presence of the C-N stretching band at 2164 cm^{-1} in the film is evidence that the Ag(CN)_2^- species has been incorporated into the film. Furthermore, the shift of the C-N stretching band by $\sim 30\text{ cm}^{-1}$ to higher frequency relative to the KAg(CN)_2 is indicative that the CN ligands have assumed a bridging mode.

The FT-IR spectrum obtained for the *Ni(cyclam)* film transferred from a Ni(CN)_4^{2-} subphase is compared to the spectrum obtained for $\text{K}_2\text{Ni(CN)}_4$ as a KBr pellet in Figure 8-6. The absorbance due to the C-N stretching mode is observed in the film and indicates that the Ni(CN)_4^{2-} species has been incorporated into the monolayer. The band is well resolved into two separate peaks; one occurs at the same frequency, 2124 cm^{-1} , as

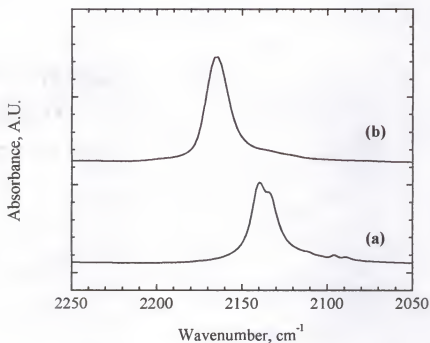


Figure 8-5. Infrared absorbance spectra of the C-N stretching region for (a) $\text{KAg}(\text{CN})_2$ as a KBr pellet and (b) a monolayer film of $\text{Fe}(\text{terpy})$ transferred from a $\text{KAg}(\text{CN})_2$ subphase. The shift to higher wavenumber in the film is indicative of cyanide bridging.

the C-N stretching mode for the $\text{K}_2\text{Ni}(\text{CN})_4$ solid; and one that is shifted by 40 cm^{-1} to 2164 cm^{-1} . The shift to higher frequency is supportive of bridging cyanides. The near equal intensity of the two absorbance bands supports the target linear chain structure where two of the nickel cyanides are bridged and two are terminal. A similar splitting of the C-N stretching band has been reported in a nickel cyanide linear chain material.²⁴⁸

The FT-IR spectrum for a thin film sample of the $\text{Ni}(\text{cyclam})$ complex transferred after reaction with a $\text{Cr}(\text{CN})_6^{3-}$ subphase is related to the FT-IR spectrum of $\text{K}_3\text{Cr}(\text{CN})_6$ as a KBr pellet in Figure 8-7. The C-N absorbance bands at 2130 and 2160 cm^{-1} confirm the incorporation of chromium cyanide into the film. The absorbance at 2130 cm^{-1} matches with the 2130 cm^{-1} peak observed in the starting material and indicates the

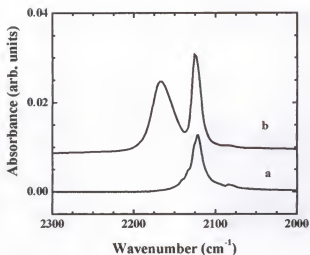


Figure 8-6. Infrared absorbance spectra of the C-N stretching region for (a) $\text{K}_2\text{Ni}(\text{CN})_4$ as a KBr pellet and (b) a monolayer film of *Ni(cyclam)* transferred off a $\text{K}_2\text{Ni}(\text{CN})_4$ subphase. The shift to higher wavenumber in the film is indicative of cyanide bridging.

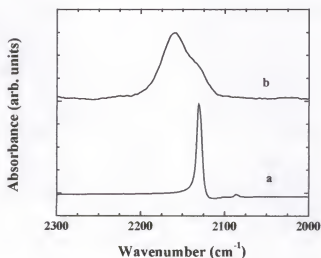


Figure 8-7. Infrared absorbance spectra of the C-N stretching region for (a) $\text{K}_3\text{Cr}(\text{CN})_6$ as a KBr pellet and (b) a monolayer film of *Ni(cyclam)* transferred off a $\text{K}_3\text{Cr}(\text{CN})_6$ subphase. The shift to higher wavenumber in the film is indicative of cyanide bridging.

presence of terminal cyanides in the film. The peak at 2160 cm^{-1} is shifted relative to the starting material and indicates the presence of cyanide bridges in the film. The presence of both bridged and non-bridged cyanides in the film is consistent with what would be expected for a honeycomb network in which three facial cyanides are terminal and the three opposing facial cyanides are bridges. Similar C-N stretching frequencies were reported for other two-dimensional honeycomb networks built on chromium hexacyanide and analogous nickel cyclam complexes.^{211,213}

Grazing Incidence X-ray Diffraction

The BAM images and FT-IR spectra for both the *Fe(terpy)* and *Ni(cyclam)* systems are suggestive of the formation of cyanide-bridged networks at the air-water interface. Final confirmation of the structures being formed was sought through GIXD. The *Fe(terpy)* material was investigated *in situ* as a Langmuir monolayer while still on the water surface. The GIXD pattern obtained on the *Fe(terpy)* monolayer over pure water at the onset of surface pressure is shown in Figure 8-8. The pattern consists of a single broad peak at a d spacing of 4.18 \AA indicating a loose organization of the alkyl chains.⁷⁹ The presence of some degree of order in the film at low pressure is indicative of incomplete spreading of the amphiphile. This aggregation was also evident in the BAM image taken at low pressure in Figure 8-3. The structure of the film at the same pressure is clearly different when $\text{Ag}(\text{CN})_2^-$ ions are present in the subphase. The peak at 4.18 \AA due to the alkyl chain packing has vanished and a series of three sharp peaks are observed at d spacings of 3.75 \AA , 3.04 \AA , and 2.37 \AA . The pattern is consistent with the formation of a crystalline phase at the air-water interface. Analysis of the width of the peak at 3.04 \AA by the Scherrer method¹⁴⁷ yields a crystal coherence length of $\sim 375\text{ \AA}$.

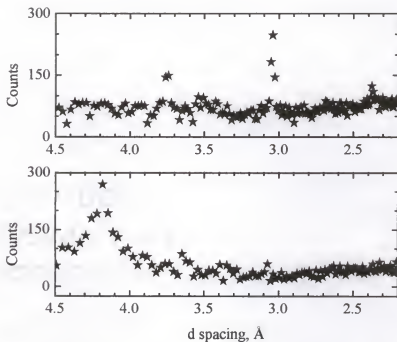


Figure 8-7. The GIXD pattern obtained off the water surface for the *Fe(terpy)* monolayer (bottom) over pure water at the onset of surface pressure and (top) over 1 mM KAg(CN)_2 at the onset of surface pressure.

Similar diffraction patterns are obtained on 30 bilayer films of the *Fe(terpy)* complex transferred at 30 mN/m over pure water and Ag(CN)_2^- subphases (Figure 8-8). The multilayer film transferred over pure water shows two peaks at 4.08 Å and 3.50 Å. The d spacings are typical of alkyl chain packing and the presence of two peaks in alkyl systems is usually indicative a nearest-neighbor tilt that leads to a centered rectangular cell.⁷⁹ The size mismatch between the terpyridine head group and the alkyl chain would force a highly tilted aggregation of the hydrocarbon tails. The multilayer film transferred over Ag(CN)_2^- shows the same set of peaks as observed in the analogous Langmuir monolayer diffraction. A wide scan range is available for transferred films allowing for the detection of a fourth diffraction peak at 1.87 Å. As with the monolayer film, the

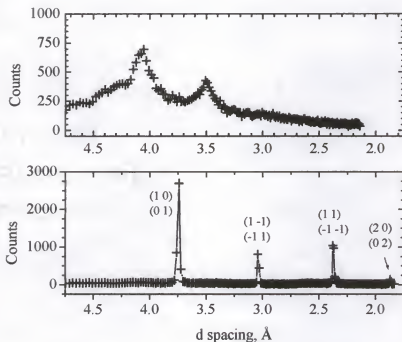


Figure 8-8. GIXD patterns obtained on 30 bilayer films of the *Fe(terpy)* complex transferred at 30 mN/m over (top) pure water and (bottom) a 1 mM $\text{KAg}(\text{CN})_2$ subphase. The peaks in the bottom diffraction pattern are indexed to the trigonal unit cell reported for AgCN as described in the text.

absence of the diffraction peaks corresponding to the alkyl chain organization is indicative of an interaction between the *Fe(terpy)* complex and the silver cyanide ions. The presence of octadecanol in the multilayer film may also be responsible for the interruption of the alkyl chain packing; however, the presence of the alcohol did not affect the diffraction of the monolayer sample in a control study. Analysis of the peak widths for the *Fe(terpy)* film reacted with $\text{Ag}(\text{CN})_2^-$ yield an average coherence length of ~ 450 Å and verify the presence of well-ordered networks in the multilayer films, vide infra.

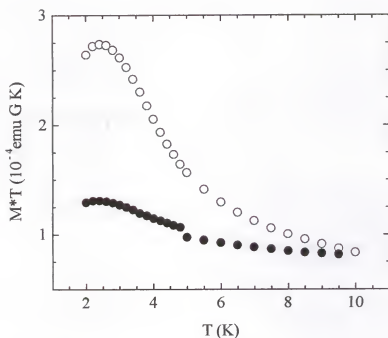


Figure 8-9. The magnetization as a function of temperature for the *Ni(cyclam)* film reacted with $\text{Cr}(\text{CN})_6^{3-}$. The data are shown for two orientation of the sample with respect to the applied 20 G field. Open circles are with the plane of the sample surface perpendicular to the applied field, solid circles are for the parallel orientation.

The *Ni(cyclam)* system was also subjected to GIXD studies. Diffraction scans were performed on both Langmuir monolayers over $\text{Ni}(\text{CN})_4^{2-}$ and $\text{Cr}(\text{CN})_6^{3-}$ subphases and also on 10 bilayer films prepared over $\text{Ni}(\text{CN})_4^{2-}$ and $\text{Cr}(\text{CN})_6^{3-}$ subphases. There was no evidence of diffraction in any of the systems over the $5^\circ < 2\theta < 30^\circ$ (14.4 Å to 2.4 Å) range studied, vide infra.

Magnetism

The lack of structural information obtained from the GIXD experiments on the *Ni(cyclam)* - $\text{Cr}(\text{CN})_6$ film prompted a search for other evidence indicating the presence of an extended network in the film. The presence of two paramagnetic metal centers in the *Ni(cyclam)* film prepared with $\text{Cr}(\text{CN})_6^{3-}$ allows for possible magnetic exchange

interactions between neighboring metal sites. The magnetization as a function of temperature for the *Ni(cyclam)* film reacted with $\text{Cr}(\text{CN})_6^{3-}$ is shown in Figure 8-9 in the form of a $M \cdot T$ plot. The film was 68 bilayers per side and measured 5 cm^2 . The data are shown for two orientations of the film with respect to the applied field. The magnetic response is anisotropic with a stronger magnetic response observed when the sample is aligned with the plane of the sample surface perpendicular to the applied field. The upturn in both plots below 6 K is a signature of ferromagnetic exchange interactions in the material. The plots show a cusp at a temperature of 2.5 K suggesting a transition to a long-range ordered state below $T_c \sim 2 \text{ K}$.

Structures of the Networks

Fe(terpy). The data presented above for the films prepared from *Fe(terpy)* and $\text{Ag}(\text{CN})_2^-$ provide clear evidence for the presence of an extended inorganic network in the films. The GIXD data do not agree with the target network described in Scheme 8-1. The d-spacings for the reflections indicate a much smaller unit cell than would be expected for an *Fe(terpy)*-NC-Ag-CN-*Fe(terpy)*-... arrangement with an Fe-Fe separation on the order of 11 Å. In addition, the terpyridine ligand is $\sim 10 \text{ Å}$ across. Thus, the unit cell expected for such an arrangement would be at least 100 Å^2 . The long coherence lengths indicated by the narrow peak widths are suggestive of inorganic crystallites being formed under the monolayer. The most likely structure to form under the monolayer would be polymeric AgCN. The crystal structure of AgCN has recently been reported by Bowmaker.²⁵⁰ The reported structure, as shown in Figure 8-10, consists of isolated linear $(\text{Ag-CN})_n$ repeating units. The unit cell can be assigned to a trigonal space group with $a = 3.88 \text{ Å}$ and $\alpha = 101.11^\circ$. Using these cell parameters, one can

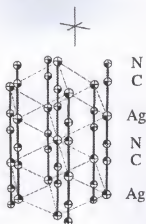


Figure 8-10. The structure of AgCN, taken from reference 250.

calculate the in-plane scattering expected for a series of (hk) reflections. The results are compared to the observed reflections for the *Fe(terpy)*-AgCN film in Table 1. The two sets of data agree very well and suggest that the diffraction observed in the film is due to the formation of AgCN within the film. Further evidence is provided by the FT-IR spectrum of the film shown in Figure 8-5. The absorbance at 2164 cm^{-1} is identical to that reported for AgCN.²⁵⁰ One thing that remains uncertain is what function the *Fe(terpy)* compound serves in the formation of the AgCN. The structure of the monolayer is altered in the presence of the $\text{Ag}(\text{CN})_2^-$ complex as evidenced by the disappearance of the alkyl chain diffraction when the film is over a silver cyanide subphase. The iron complex may promote the formation of the AgCN polymer by consumption of photo-labilized CN^- ligands. The resulting cyanide-deficient silver complex could then polymerize with other cyanide-deficient silver complexes. The monolayer could also provide a high-energy surface for the subsequent crystallization of the AgCN. The crystallization of inorganic solids beneath Langmuir monolayers has

Table 8-1. Calculated lattice d-spacing for trigonal AgCN, $a = 3.88 \text{ \AA}$ $\alpha = 101.11^\circ$ (from data in reference 249) compared to the lattice d-spacing observed in the *Fe(terpy)*-AgCN film (Figure 8-8).

(h k)	Calc d-spacing (Å)	Obs d-spacing (Å)
(1 0) (0 1)	3.81	3.74
(1 -1) (-1 1)	3.00	3.04
(1 1) (-1 -1)	2.47	2.38
(2 0) (0 2)	1.90	1.85

been reported for a number of systems and it is quite possible a similar process is occurring beneath the *Fe(terpy)* monolayer.

Ni(cyclam). The lack of diffraction data for this system makes an unambiguous structural assignment impossible. However, the BAM images and infrared absorbance spectra for the two metal cyanide films are highly suggestive to the formation of extended networks in these films. The presence of both bridged and non-bridged cyanides is in agreement with the reported cyanide stretching band in analogous solid state materials. For the $\{Ni(cyclam)-Ni(CN)_4\}$ linear chain film, the infrared data are the only available probes into the structure of these films, since the presence of diamagnetic square planar tetracyanonickelate species would discriminate against long-range magnetic order. The $\{Ni(cyclam)-Cr(CN)_6\}$ honeycomb networks are magnetic. The magnetic properties of several $\{Ni(cyclam)-Cr(CN)_6\}$ honeycomb networks are available for comparison.^{42,211,213} The magnetic behavior in these materials is varied, but all show the presence of ferromagnetic exchange within the two-dimensional sheets. The materials reported by Kou²¹¹ and by Marvillier²¹³ show metamagnetic behavior due to the presence

of inter-planar antiferromagnetic coupling below $T_N \sim 12$ K. The material described by Ferlay⁴² showed the presence of ferromagnetic coupling, but no transition to an ordered state above 2 K. The film we have prepared is not isostructural in the strictest sense with the analogous solids since the film consists of bilayers effectively isolated by the hydrocarbon inter-bilayer region. This structural difference effectively lowers the dimensionality of the material and may disrupt any long-range antiferromagnetic interactions. As isolated two-dimensional networks, the ordering temperature is expected to be low. Further magnetic measurements near the apparent transition at 2 K with AC magnetometry would help discern if the cusp in the M^*T data is due to long range magnetic ordering. The presence of such order would be clear evidence of a structurally coherent network; however, the structure of the network would still be open to question without the necessary diffraction data. The absence of diffraction in these materials is not certain since the rather large unit cells would place the primary diffraction peaks at low angles in the GIXD scan. Unfortunately, the low angle region has a very high background due to scattering in the incident beam. Repeating the diffraction experiments at as low energy as possible would aid in moving the larger d-space peaks to higher angles and thereby reduce the background contribution. In closing, it is also worth noting that the only structures reported to date for the product of a reaction between *Ni(cyclam)* complexes and chromium(III)hexacyanide have been the two-dimensional honeycomb networks, suggesting that this is the preferred product of the reaction.

Conclusions

The reaction of two low symmetry amphiphilic transition metal complexes with aqueous metal cyanides has been performed at the air water interface. One system involved the reaction of a Langmuir monolayer of an amphiphilic "T-shaped"

$\text{Fe(III)(mono-terpyridine)trichloride}$ complex with aqueous linear dicyanoargentate ions. Characterization of the resulting film by FT-IR and GIXD showed that product of the reaction was not the expected *Fe(terpy)-NC-Ag* linear chain polymer, but instead polymeric AgCN crystallites which formed under the surface of the monolayer. The other system studied involved the reaction of an amphiphilic nickel(cyclam) complex contained as a Langmuir monolayer aqueous square planar tetracyanonickelate and octahedral chromium(III)hexacyanide ions. Characterization of the resulting *Ni(cyclam)Ni(CN)₄* film by BAM and FT-IR gave evidence for the formation of a cyanide-bridged linear chain polymer; however, direct structural confirmation with the material was hampered by the lack of significant diffraction from GIXD studies. The lack of sufficient x-ray diffraction for the *Ni(cyclam)Cr(CN)₆* film prevented a detailed structure assignment for the material; however the FT-IR spectrum and magnetic behaviors observed were consistent with the target two-dimensional honeycomb network structure.

LIST OF REFERENCES

- (1) Lehn, J. M.; Atwood, J. L.; Davies, J. E. D.; McNicol, D. D.; Vogtle, V., Eds. *Comprehensive Supramolecular Chemistry*; Pergamon Press: Oxford, U. K., 1996.
- (2) Philp, D.; Stoddart, J. F. *Angew. Chem. Int. Edit.* **1996**, *35*, 1155-1196.
- (3) Greig, L. M.; Philp, D. *Chem. Soc. Rev.* **2001**, *30*, 287-302.
- (4) Fredericks, J. R.; Hamilton, A. D. In *Supramolecular Control of Structure and Reactivity*; Hamilton, A. D., Ed.; John Wiley and Sons: New York, 1996, p 1.
- (5) Baxter, P. N. W. In *Comprehensive Supramolecular Chemistry*; Sauvage, J. P., Hosseini, M. W., Eds.; Pergamon Press: Oxford, U. K., 1996; Vol. 9, p 165.
- (6) Fujita, M. In *Comprehensive Supramolecular Chemistry*; Sauvage, J. P., Hosseini, M. W., Eds.; Pergamon Press: Oxford, U. K., 1996; Vol. 9, p 253.
- (7) Funeriu, D. P.; Lehn, J. M.; Baum, G.; Fenske, D. *Chem. Eur. J.* **1997**, *3*, 99-104.
- (8) Vance, A. L.; Alcock, N. W.; Busch, D. H.; Heppert, J. A. *Inorg. Chem.* **1997**, *36*, 5132-5134.
- (9) Yaghi, O. M.; Li, H. L.; Groy, T. L. *Inorg. Chem.* **1997**, *36*, 4292-4293.
- (10) Yaghi, O. M.; Li, H. L.; Davis, C.; Richardson, D.; Groy, T. L. *Acc. Chem. Res.* **1998**, *31*, 474-484.
- (11) Lopez, S.; Kahraman, M.; Harmata, M.; Keller, S. W. *Inorg. Chem.* **1997**, *36*, 6138-6140.
- (12) Lu, J.; Paliwala, T.; Lim, S. C.; Yu, C.; Niu, T. Y.; Jacobson, A. J. *Inorg. Chem.* **1997**, *36*, 923-929.
- (13) Dunbar, K. R.; Heintz, R. A. *Prog. Inorg. Chem.* **1997**, *45*, 283-391.
- (14) Stang, P. J.; Olenyuk, B. *Acc. Chem. Res.* **1997**, *30*, 502-518.
- (15) Stang, P. J. *Chem. Eur. J.* **1998**, *4*, 19-27.
- (16) Clemente-Juan, J. M.; Coronado, E. *Coord. Chem. Rev.* **1999**, *195*, 361-394.
- (17) Sessoli, R.; Tsai, H. L.; Schake, A. R.; Wang, S. Y.; Vincent, J. B.; Folting, K.; Gatteschi, D.; Christou, G.; Hendrickson, D. N. *J. Am. Chem. Soc.* **1993**, *115*, 1804-1816.
- (18) Shores, M. P.; Sokol, J. J.; Long, J. R. *J. Am. Chem. Soc.* **2002**, *124*, 2279-2292.
- (19) Berseth, P. A.; Sokol, J. J.; Shores, M. P.; Heinrich, J. L.; Long, J. R. *J. Am. Chem. Soc.* **2000**, *122*, 9655-9662.
- (20) Heinrich, J. L.; Sokol, J. J.; Hee, A. G.; Long, J. R. *J. Solid State Chem.* **2001**, *159*, 293-301.
- (21) Larionova, J.; Gross, M.; Pilkington, M.; Andres, H.; Stoeckli-Evans, H.; Gudel, H. U.; Decurtins, S. *Angew. Chem.-Int. Edit.* **2000**, *39*, 1605-1609.
- (22) Rogez, G.; Parsons, S.; Paulsen, C.; Villar, V.; Mallah, T. *Inorg. Chem.* **2001**, *40*, 3836-3837.
- (23) Parker, R. J.; Spiccia, L.; Berry, K. J.; Fallon, G. D.; Moubaraki, B.; Murray, K. S. *Chem. Commun.* **2001**, 333-334.

- (24) Scuiller, A.; Mallah, T.; Verdaguer, M.; Nivorozhkin, A.; Tholence, J. L.; Veillet, P. *New J. Chem.* **1996**, 20, 1-3.
- (25) Mallah, T.; Auberger, C.; Verdaguer, M.; Veillet, P. *Chem. Commun.* **1995**, 61-62.
- (26) Oshio, H.; Tamada, O.; Onodera, H.; Ito, T.; Ikoma, T.; Tero-Kubota, S. *Inorg. Chem.* **1999**, 38, 5686-5689.
- (27) Oshio, H.; Onodera, H.; Tamada, O.; Mizutani, H.; Hikichi, T.; Ito, T. *Chem. Eur. J.* **2000**, 6, 2523-2530.
- (28) Fujita, M.; Ogura, K. *Coord. Chem. Rev.* **1996**, 148, 249-264.
- (29) Fujita, M.; Yu, S. Y.; Kusukawa, T.; Funaki, H.; Ogura, K.; Yamaguchi, K. *Angew. Chem. Int.* **1998**, 37, 2082-2085.
- (30) Kou, H. Z.; Liao, D. Z.; Jiang, Z. H.; Yan, S. P.; Wu, Q. J.; Gao, S.; Wang, G. L. *Inorg. Chem. Commun.* **2000**, 3, 151-154.
- (31) Ohba, M.; Usuki, N.; Fukita, N.; Okawa, H. *Inorg. Chem.* **1998**, 37, 3349-3354.
- (32) Cernak, J.; Orendac, M.; Potocnak, I.; Chomic, J.; Orendacova, A.; Skorsepa, J.; Feher, A. *Coord. Chem. Rev.* **2002**, 224, 51-66.
- (33) Ohba, M.; Fukita, N.; Okawa, H. *J. Chem. Soc. Dalton Trans.* **1997**, 1733-1737.
- (34) Ohba, M.; Maruono, N.; Okawa, H.; Enoki, T.; Latour, J. M. *J. Am. Chem. Soc.* **1994**, 116, 11566-11567.
- (35) Zhan, S. Z.; Guo, D.; Zhang, X. Y.; Du, C. X.; Zhu, Y.; Yang, R. N. *Inorg. Chim. Acta* **2000**, 298, 57-62.
- (36) Clearfield, A. In *Prog. Inorg. Chem.* **1998**, 47, 371-510.
- (37) Ohba, M.; Okawa, H.; Ito, T.; Ohto, A. *Chem. Commun.* **1995**, 1545-1546.
- (38) Ohba, M.; Okawa, H.; Fukita, N.; Hashimoto, Y. *J. Am. Chem. Soc.* **1997**, 119, 1011-1019.
- (39) Kou, H. Z.; Tang, J. K.; Liao, D. Z.; Gao, S.; Cheng, P.; Jiang, Z. H.; Yan, S. P.; Wang, G. L.; Chansou, B.; Tuchagues, J. P. *Inorg. Chem.* **2001**, 40, 4839-4844.
- (40) Kou, H. Z.; Bu, W. M.; Liao, D. Z.; Jiang, Z. H.; Yan, S. P.; Fan, Y. G.; Wang, G. L. *J. Chem. Soc. Dalton Trans.* **1998**, 4161-4164.
- (41) Colacio, E.; Dominguez-Vera, J. M.; Ghazi, M.; Kivekas, R.; Lloret, F.; Moreno, J. M.; Stoeckli-Evans, H. *Chem. Commun.* **1999**, 987-988.
- (42) Ferlay, S.; Mallah, T.; Vaissermann, J.; Bartolome, F.; Veillet, P.; Verdaguer, M. *Chem. Commun.* **1996**, 2481-2482.
- (43) Kou, H. Z.; Gao, S.; Bu, W. M.; Liao, D. Z.; Ma, B. Q.; Jiang, Z. H.; Yan, S. P.; Fan, Y. G.; Wang, G. L. *J. Chem. Soc. Dalton Trans.* **1999**, 2477-2480.
- (44) Laget, V.; Hornick, C.; Rabu, P.; Drillon, M.; Ziessel, R. *Coord. Chem. Rev.* **1998**, 180, 1533-1553.
- (45) Batten, S. R.; Robson, R. *Angew. Chem. Int. Edit.* **1998**, 37, 1461-1494.
- (46) Blake, A. J.; Champness, N. R.; Hubberstey, P.; Li, W. S.; Withersby, M. A.; Schroder, M. *Coord. Chem. Rev.* **1999**, 183, 117-138.
- (47) Swiegers, G. F.; Malefetse, T. J. *Chem. Rev.* **2000**, 100, 3483-3537.
- (48) Xia, Y. N.; Whitesides, G. M. *Angew. Chem. Int. Edit.* **1998**, 37, 551-575.
- (49) Kahn, O. *Molecular Magnetism*; VCH: New York, 1993.
- (50) Coronado, E.; Galan-Mascaros, J. R.; Gomez-Garcia, C. J.; Laukhin, V. *Nature* **2000**, 408, 447-449.
- (51) Ferlay, S.; Mallah, T.; Ouahes, R.; Veillet, P.; Verdaguer, M. *Nature* **1995**, 378, 701-703.

- (52) Mallah, T.; Thiebaut, S.; Verdaguer, M.; Veillet, P. *Science* **1993**, *262*, 1554-1557.
- (53) Entley, W. R.; Girolami, G. S. *Science* **1995**, *268*, 397-400.
- (54) Sato, O.; Iyoda, T.; Fujishima, A.; Hashimoto, K. *Science* **1996**, *271*, 49-51.
- (55) Sato, O.; Iyoda, T.; Fujishima, A.; Hashimoto, K. *Science* **1996**, *272*, 704-705.
- (56) Mizuno, M.; Ohkoshi, S.; Hashimoto, K. *Adv. Mater.* **2000**, *12*, 1955-+.
- (57) Shipway, A. N.; Willner, I. *Acc. Chem. Res.* **2001**, *34*, 421-432.
- (58) Armand, F.; Albouy, P. A.; Da Cruz, F.; Normand, M.; Huc, V.; Goron, E. *Langmuir* **2001**, *17*, 3431-3437.
- (59) Bowden, N.; Terfort, A.; Carbeck, J.; Whitesides, G. M. *Science* **1997**, *276*, 233-235.
- (60) Bowden, N.; Choi, I. S.; Grzybowski, B. A.; Whitesides, G. M. *J. Am. Chem. Soc.* **1999**, *121*, 5373-5391.
- (61) Bowden, N.; Arias, F.; Deng, T.; Whitesides, G. M. *Langmuir* **2001**, *17*, 1757-1765.
- (62) Weissbuch, I.; Baxter, P. N. W.; Cohen, S.; Cohen, H.; Kjaer, K.; Howes, P. B.; Als-Nielsen, J.; Hanan, G. S.; Schubert, U. S.; Lehn, J. M.; Leiserowitz, L.; Lahav, M. *J. Am. Chem. Soc.* **1998**, *120*, 4850-4860.
- (63) Weissbuch, I.; Baxter, P. N. W.; Kuzmenko, I.; Cohen, H.; Cohen, S.; Kjaer, K.; Howes, P. B.; Als-Nielsen, J.; Lehn, J. M.; Leiserowitz, L.; Lahav, M. *Chem. Eur. J.* **2000**, *6*, 725-734.
- (64) Mingotaud, C.; Lafuente, C.; Amiel, J.; Delhaes, P. *Langmuir* **1999**, *15*, 289-292.
- (65) Huo, Q.; Russell, K. C.; Leblanc, R. M. *Langmuir* **1998**, *14*, 2174-2186.
- (66) Ulman, A. *An Introduction to Ultrathin Organic Films: From Langmuir-Blodgett to Self-Assembly*; Academic Press: Boston, 1991.
- (67) Roberts, C. G. *Langmuir-Blodgett Films*; Plenum Press: New York, 1990.
- (68) Langmuir, I. *J. Am. Chem. Soc.* **1917**, *39*, 1848-1906.
- (69) Jones, L. H. *Inorg. Chem.* **1963**, *2*, 777-&.
- (70) Bigozzi, C. A.; Argazzi, R.; Schoonover, J. R.; Gordon, K. C.; Dyer, R. B.; Scandola, F. *Inorg. Chem.* **1992**, *31*, 5260-5267.
- (71) Alvarez, S.; Lopez, C.; Bermejo, M. J. *Transit. Met. Chem.* **1984**, *9*, 123-126.
- (72) Shriver, D. F. *J. Am. Chem. Soc.* **1963**, *85*, 1405-&.
- (73) Dows, D. A.; Haim, A.; Wilmarth, W. K. *J. Inorg. Nucl. Chem.* **1961**, *21*, 33-37.
- (74) Duke, P. J. *Synchrotron Radiation: Production and Properties*; Oxford University Press: New York, 2000.
- (75) Advanced Photon Source, <http://aps.anl.gov>, accessed September 13, 2002.
- (76) Materials Research Collaborative Access Team, <http://ixs.csrii.iit.edu/mrcat/>, accessed September 13, 2002.
- (77) Advanced Photon Source, <http://www.imca.aps.anl.gov/mx/>, accessed September 13, 2002.
- (78) Als-Nielsen, J.; Jacquemain, D.; Kjaer, K.; Leveiller, F.; Lahav, M.; Leiserowitz, L. *Phys. Rep.* **1994**, *246*, 252-313.
- (79) Kaganer, V. M.; Mohwald, H.; Dutta, P. *Rev. Mod. Phys.* **1999**, *71*, 779-819.
- (80) Kuzmenko, I.; Rapaport, H.; Kjaer, K.; Als-Nielsen, J.; Weissbuch, I.; Lahav, M.; Leiserowitz, L. *Chem. Rev.* **2001**, *101*, 1659-1696.
- (81) International XAFS Society, <http://ixs.iit.edu/>, accessed September 13, 2002.

- (82) Teo, B. K. *EXAFS: Basic Principles and Data Analysis*; Springer-Verlag: New York, 1986.
- (83) Sayers, D. E.; Stern, E. A.; Lytle, F. W. *Phys. Rev. Lett.* **1971**, *27*, 1204-&.
- (84) Ressler, T. J. *Synchrotr. Radiat.* **1998**, *5*, 118-122.
- (85) Zabinsky, S. I.; Rehr, J. J.; Ankudinov, A.; Albers, R. C.; Eller, M. J. *Phys. Rev. B* **1995**, *52*, 2995-3009.
- (86) Ankudinov, A.; "Ph. D. Thesis"; University of Washington, 1996.
- (87) Clearfield, A.; Smith, G. D. *Inorg. Chem.* **1969**, *8*, 431-&.
- (88) Clearfield, A. *Chem. Rev.* **1988**, *88*, 125-148.
- (89) Alberti, G.; Costantino, U.; Allulli, S.; Tomassini, N. *J. Inorg. Nucl. Chem.* **1978**, *40*, 1113-1117.
- (90) Cao, G.; Lee, H.; Lynch, V. M.; Mallouk, T. E. *Solid State Ion.* **1988**, *26*, 63-69.
- (91) Cao, G.; Lee, H.; Lynch, V. M.; Mallouk, T. E. *Inorg. Chem.* **1988**, *27*, 2781-2785.
- (92) Cunningham, D.; Hennelly, P. J. D. *Inorg. Chim. Acta* **1979**, *37*, 95-102.
- (93) Ortizavila, Y.; Rudolf, P. R.; Clearfield, A. *Inorg. Chem.* **1989**, *28*, 2137-2141.
- (94) Caldwell, W. B.; Campbell, D. J.; Chen, K. M.; Herr, B. R.; Mirkin, C. A.; Malik, A.; Durbin, M. K.; Dutta, P.; Huang, K. G. *J. Am. Chem. Soc.* **1995**, *117*, 6071-6082.
- (95) Katz, H. E.; Scheller, G.; Putvinski, T. M.; Schilling, M. L.; Wilson, W. L.; Chidsey, C. E. D. *Science* **1991**, *254*, 1485-1487.
- (96) Katz, H. E.; Schilling, M. L.; Chidsey, C. E. D.; Putvinski, T. M.; Hutton, R. S. *Chem. Mat.* **1991**, *3*, 699-703.
- (97) Katz, H. E.; Wilson, W. L.; Scheller, G. *J. Am. Chem. Soc.* **1994**, *116*, 6636-6640.
- (98) Dines, M. B.; Digiacomo, P. M. *Inorg. Chem.* **1981**, *20*, 92-97.
- (99) Poojary, D. M.; Vermeulen, L. A.; Vicenzi, E.; Clearfield, A.; Thompson, M. E. *Chem. Mat.* **1994**, *6*, 1845-1849.
- (100) Visser, D.; Carling, S. G.; Day, P.; Deportes, J. J. *Appl. Phys.* **1991**, *69*, 6016-6018.
- (101) Carling, S. G.; Day, P.; Visser, D.; Kremer, R. K. *J. Solid State Chem.* **1993**, *106*, 111-119.
- (102) Carling, S. G.; Day, P.; Visser, D. *Inorg. Chem.* **1995**, *34*, 3917-3927.
- (103) Carling, S. G.; Day, P.; Visser, D. *J. Phys. Condes. Matter* **1995**, *7*, L109-L113.
- (104) Rabu, P.; Janvier, P.; Bujoli, B. *J. Mater. Chem.* **1999**, *9*, 1323-1326.
- (105) Lebideau, J.; Payen, C.; Bujoli, B.; Palvadeau, P.; Rouxel, J. *J. Magn. Magn. Mater.* **1995**, *140*, 1719-1720.
- (106) Bujoli, B.; Pena, O.; Palvadeau, P.; Lebideau, J.; Payen, C.; Rouxel, J. *Chem. Mat.* **1993**, *5*, 583-587.
- (107) Gerbier, P.; Guerin, C.; Le Bideau, J.; Valle, K. *Chem. Mat.* **2000**, *12*, 264-267.
- (108) Fanucci, G. E.; Krzystek, J.; Meisel, M. W.; Brunel, L. C.; Talham, D. R. *J. Am. Chem. Soc.* **1998**, *120*, 5469-5479.
- (109) Fanucci, G. E.; Petruska, M. A.; Meisel, M. W.; Talham, D. R. *J. Solid State Chem.* **1999**, *145*, 443-451.
- (110) Byrd, H.; Pike, J. K.; Talham, D. R. *Chem. Mat.* **1993**, *5*, 709-715.
- (111) Byrd, H.; Pike, J. K.; Talham, D. R. *J. Am. Chem. Soc.* **1994**, *116*, 7903-7904.
- (112) Byrd, H.; Pike, J. K.; Talham, D. R. *Synth. Met.* **1995**, *71*, 1977-1980.

- (113) Fanucci, G. E.; Seip, C. T.; Petruska, M. A.; Nixon, C. M.; Ravaine, S.; Talham, D. R. *Thin Solid Films* **1998**, *329*, 331-335.
- (114) Fanucci, G. E.; Talham, D. R. *Langmuir* **1999**, *15*, 3289-3295.
- (115) Petruska, M. A.; Fanucci, G. E.; Talham, D. R. *Chem. Mat.* **1998**, *10*, 177-189.
- (116) Petruska, M. A.; Fanucci, G. E.; Talham, D. R. *Thin Solid Films* **1998**, *329*, 131-135.
- (117) Petruska, M. A.; Talham, D. R. *Chem. Mat.* **1998**, *10*, 3672-3682.
- (118) Petruska, M. A.; Talham, D. R. *Langmuir* **2000**, *16*, 5123-5129.
- (119) Petruska, M. A.; Watson, B. C.; Meisel, M. W.; Talham, D. R. *Chem. Mat.* **2002**, *14*, 2011-2019.
- (120) de Jongh, L. J. In *Magnetic Properties of Layered Transition Metal Compounds*; de Jongh, L. J., Ed.; Kluwer Academic Publishers: Dordrecht, 1990, pp 1-51.
- (121) Rubenacker, G. V.; Raffaele, D. P.; Drumheller, J. E.; Emerson, K. *Phys. Rev. B* **1988**, *37*, 3563-3568.
- (122) Zenmyo, K.; Kubo, H. *J. Phys. Soc. Jpn.* **1995**, *64*, 1320-1325.
- (123) DeFotis, G. C.; Just, E. M.; Pugh, V. J.; Coffey, G. A.; Hogg, B. D.; Fitzhenry, S. L.; Marmorino, J. L.; Krovich, D. J.; Chamberlain, R. V. *J. Magn. Magn. Mater.* **1999**, *202*, 27-46.
- (124) DeFotis, G. C.; Coker, G. S.; Jones, J. W.; Branch, C. S.; King, H. A.; Bergman, J. S.; Lee, S.; Goodey, J. R. *Phys. Rev. B* **1998**, *58*, 12178-12192.
- (125) Defotis, G. C.; Mantus, D. S.; McGhee, E. M.; Echols, K. R.; Wiese, R. S. *Phys. Rev. B* **1988**, *38*, 11486-11499.
- (126) Mydosh, J. A. *Spin Glasses*; Taylor and Francis: Washington, DC, 1993.
- (127) Nguyen, H. C.; Goodenough, J. B. *Phys. Rev. B* **1995**, *52*, 8776-8787.
- (128) Nuttall, C. J.; Day, P. *Chem. Mat.* **1998**, *10*, 3050-3057.
- (129) Fanucci, G. E.; Culp, J. T.; Watson, B. C.; Backov, R.; Ohnuki, H.; Talham, D. R.; Meisel, M. W. *Physica B* **2000**, *284*, 1499-1500.
- (130) Signore, P. J. C.; "Ph. D. Thesis"; University of Florida, 1994.
- (131) Ward, B. H.; Granroth, G. E.; Walden, J. B.; Abboud, K. A.; Meisel, M. W.; Rasmussen, P. G.; Talham, D. R. *J. Mater. Chem.* **1998**, *8*, 1373-1378.
- (132) Seip, C. T.; Byrd, H.; Talham, D. R. *Inorg. Chem.* **1996**, *35*, 3479-3483.
- (133) Lines, M. E. *J. Phys. Chem. Solids* **1970**, *31*, 101.
- (134) Sykes, M. F.; Fisher, M. E. *Physica* **1962**, *28*, 919.
- (135) Navarro, R. In *Magnetic Properties of Layered Transition Metal Compounds*; de Jongh, L. J., Ed.; Kluwer Academic Publishers: Dordrecht, 1990.
- (136) Fishman, S.; Aharony, A. *Phys. Rev. B* **1978**, *18*, 3507-3520.
- (137) Katsumata, K.; Kobayashi, M.; Sato, T.; Miyako, Y. *Phys. Rev. B* **1979**, *19*, 2700-2703.
- (138) Katsumata, K.; Shapiro, S. M.; Matsuda, M.; Shirane, G.; Tuchendler, J. *Phys. Rev. B* **1992**, *46*, 14906-14908.
- (139) Wong, P.; Horn, P. M.; Birgeneau, R. J.; Shirane, G. *Phys. Rev. B* **1983**, *27*, 428-447.
- (140) Coronado, E.; Galan-Mascaros, J. R.; Gomez-Garcia, C. J.; Martinez-Agudo, J. M. *Adv. Mater.* **1999**, *11*, 558-561.
- (141) Defotis, G. C.; Pohl, C.; Pugh, S. A.; Sinn, E. *J. Chem. Phys.* **1984**, *80*, 2079-2086.

- (142) Richardson, R. C.; Smith, E. N. *Experimental Techniques in Condensed Matter Physics at Low Temperatures*; Addison-Wesley Pub. Co.: Redwood City, CA, 1988.
- (143) Nguyen, H. C.; Goodenough, J. B. *Phys. Rev. B* **1995**, *52*, 324-334.
- (144) Byrd, H.; Whipps, S.; Pike, J. K.; Ma, J. F.; Nagler, S. E.; Talham, D. R. *J. Am. Chem. Soc.* **1994**, *116*, 295-301.
- (145) Seip, C. T.; Granroth, G. E.; Meisel, M. W.; Talham, D. R. *J. Am. Chem. Soc.* **1997**, *119*, 7084-7094.
- (146) Carino, S. R.; Tostmann, H.; Underhill, R. S.; Logan, J.; Weerasekera, G.; Culp, J.; Davidson, M.; Duran, R. S. *J. Am. Chem. Soc.* **2001**, *123*, 767-768.
- (147) Guinier, A. *X-ray Diffraction*; Freeman: San Francisco, 1968.
- (148) Hammond, D. B.; Rayment, T.; Dunne, D.; Hodge, P.; Ali-Adib, Z.; Dent, A. *Langmuir* **1998**, *14*, 5896-5899.
- (149) Cao, G.; Lynch, V. M.; Swinnea, J. S.; Mallouk, T. E. *Inorg. Chem.* **1990**, *29*, 2112-2117.
- (150) Wang, R. C.; Zhang, Y. P.; Hu, H. L.; Frausto, R. R.; Clearfield, A. *Chem. Mat.* **1992**, *4*, 864-871.
- (151) Ozin, G. A. *Adv. Mater.* **1992**, *4*, 612-649.
- (152) Morales, A. M.; Lieber, C. M. *Science* **1998**, *279*, 208-211.
- (153) Harrison, R. M.; Brotin, T.; Noll, B. C.; Michl, J. *Organometallics* **1997**, *16*, 3401-3412.
- (154) Magnera, T. F.; Pecka, J.; Vacek, J.; Michl, J. In *Nanostructured Materials*; American Chemical Society: Washington, DC, 1997, p 231.
- (155) Magnera, T. F.; Peslherbe, L. M.; Korblova, E.; Michl, J. *J. Organomet. Chem.* **1997**, *548*, 83-89.
- (156) Pospisil, L.; Heyrovsky, M.; Pecka, J.; Michl, J. *Langmuir* **1997**, *13*, 6294-6301.
- (157) Jacquemain, D.; Wolf, S. G.; Leveiller, F.; Deutsch, M.; Kjaer, K.; Alsniesen, J.; Lahav, M.; Leiserowitz, L. *Angew. Chem. Int. Edit.* **1992**, *31*, 130-152.
- (158) Leveiller, F.; Bohm, C.; Jacquemain, D.; Mohwald, H.; Leiserowitz, L.; Kjaer, K.; Alsniesen, J. *Langmuir* **1994**, *10*, 819-829.
- (159) Weissbuch, I.; Guo, S.; Edgar, R.; Cohen, S.; Howes, P.; Kjaer, K.; Als-Nielsen, J.; Lahav, M.; Leiserowitz, L. *Adv. Mater.* **1998**, *10*, 117-121.
- (160) Hensel, V.; Godt, A.; Popovitz-Biro, R.; Cohen, H.; Jensen, T. R.; Kjaer, K.; Weissbuch, I.; Lifshitz, E.; Lahav, M. *Chem. Eur. J.* **2002**, *8*, 1413-1423.
- (161) Landau, E. M.; Levanon, M.; Leiserowitz, L.; Lahav, M.; Sagiv, J. *Nature* **1985**, *318*, 353-356.
- (162) Frostman, L. M.; Ward, M. D. *Langmuir* **1997**, *13*, 330-337.
- (163) Whipps, S.; Khan, S. R.; O'Palko, F. J.; Backov, R.; Talham, D. R. *J. Cryst. Growth* **1998**, *192*, 243-249.
- (164) Hanan, G. S.; Volkmer, D.; Schubert, U. S.; Lehn, J. M.; Baum, G.; Fenske, D. *Angew. Chem. Int. Edit.* **1997**, *36*, 1842-1844.
- (165) Baxter, P. N. W.; Lehn, J. M.; Fischer, J.; Youinou, M. T. *Angew. Chem. Int. Edit.* **1994**, *33*, 2284-2287.
- (166) Baxter, P. N. W.; Lehn, J. M.; Kneisel, B. O.; Fenske, D. *Angew. Chem. Int. Edit.* **1997**, *36*, 1978-1981.
- (167) Michl, J.; Magnera, T. F. *Proc. Natl. Acad. Sci. U. S. A.* **2002**, *99*, 4788-4792.

- (168) Varaksa, N.; Pospisil, L.; Magnera, T. F.; Michl, J. *Proc. Natl. Acad. Sci. U. S. A.* **2002**, *99*, 5012-5017.
- (169) Gadet, V.; Mallah, T.; Castro, I.; Verdaguer, M.; Veillet, P. *J. Am. Chem. Soc.* **1992**, *114*, 9213-9214.
- (170) Re, N.; Gallo, E.; Floriani, C.; Miyasaka, H.; Matsumoto, N. *Inorg. Chem.* **1996**, *35*, 6004-6008.
- (171) Miyasaka, H.; Matsumoto, N.; Okawa, H.; Re, N.; Gallo, E.; Floriani, C. *J. Am. Chem. Soc.* **1996**, *118*, 981-994.
- (172) Zhong, Z. J.; Seino, H.; Mizobe, Y.; Hidai, M.; Fujishima, A.; Ohkoshi, S.; Hashimoto, K. *J. Am. Chem. Soc.* **2000**, *122*, 2952-2953.
- (173) Hatlevik, O.; Buschmann, W. E.; Zhang, J.; Manson, J. L.; Miller, J. S. *Adv. Mater.* **1999**, *11*, 914-918.
- (174) Holmes, S. M.; Girolami, G. S. *J. Am. Chem. Soc.* **1999**, *121*, 5593-5594.
- (175) Posiomek, E. J. *J. Org. Chem.* **1963**, *28*, 590-591.
- (176) Ruiz, A.; Rocca, P.; Marsais, F.; Godard, A.; Queguiner, G. *Tetrahedron Lett.* **1997**, *38*, 6205-6208.
- (177) Armand, F.; Sakuragi, H.; Tokumaru, K. *New J. Chem.* **1993**, *17*, 351-356.
- (178) Kern, W. *J. Electrochem. Soc.* **1990**, *137*, 1887-1892.
- (179) Maoz, R.; Sagiv, J. *J. Colloid Interface Sci.* **1984**, *100*, 465-496.
- (180) Netzer, L.; Sagiv, J. *J. Am. Chem. Soc.* **1983**, *105*, 674-676.
- (181) Hrepic, N. V.; Malin, J. M. *Inorg. Chem.* **1979**, *18*, 409-413.
- (182) Armand, F.; Sakuragi, H.; Tokumaru, K. *J. Chem. Soc. Faraday Trans.* **1993**, *89*, 1021-1024.
- (183) Seah, M. P.; Dench, W. A. *Surf. Interface Anal.* **1979**, *1*, 1.
- (184) Laibinis, P. E.; Bain, C. D.; Whitesides, G. M. *J. Phys. Chem.* **1991**, *95*, 7017-7021.
- (185) Brundle, C. R.; Hopster, H.; Swalen, J. D. *J. Chem. Phys.* **1979**, *70*, 5190-5196.
- (186) Giorgetti, M.; Berrettoni, M.; Filipponi, A.; Kulesza, P. J.; Marassi, R. *Chem. Phys. Lett.* **1997**, *275*, 108-112.
- (187) Zhang, H. H.; Filipponi, A.; DiCicco, A.; Scott, M. J.; Holm, R. H.; Hedman, B.; Hodgson, K. O. *J. Am. Chem. Soc.* **1997**, *119*, 2470-2478.
- (188) Yokoyama, T.; Ohta, T.; Sato, O.; Hashimoto, K. *Phys. Rev. B* **1998**, *58*, 8257-8266.
- (189) Armand, F.; Okada, S.; Yase, K.; Matsuda, H.; Nakanishi, H.; Sakuragi, H.; Tokumaru, K. *Jpn. J. Appl. Phys.* **1993**, *32*, 1186-1190.
- (190) Mingotaud, A. F.; Mingotaud, C.; Patterson, L. K. *Handbook of Monolayers* 1st ed.; Academic Press: London, 1993; Vol. 1.
- (191) Ludi, A.; Güdel, H. U. *Struct. Bonding* **1973**, *14*, 1.
- (192) Gadet, V.; Bujoli-Doeuff, M.; Force, L.; Verdaguer, M.; Makhi, E.; Deroy, A.; Besse, J. P.; Chappert, C.; Veillet, P.; Renard, J. P.; Beauvillain, P. In *Molecular Magnetic Materials*; Series E ed.; Gatteschi, D., Kahn, O., Miller, J. S., Palacio, F., Eds.; Kluwer: Dordrecht, 1991; Vol. 198, p 281.
- (193) Juszczczyk, S.; Johansson, C.; Hanson, M.; Ratuszna, A.; Malecki, G. *J. Phys.-Condes. Matter* **1994**, *6*, 5697-5706.
- (194) Fukita, N.; Ohba, M.; Okawa, H. *Mol. Cryst. Liquid Cryst.* **2000**, *342*, 217-224.

- (195) Verdaguer, M.; Bleuzen, A.; Marvaud, V.; Vaissermann, J.; Seuleiman, M.; Desplanches, C.; Scullier, A.; Train, C.; Garde, R.; Gelly, G.; Lomenech, C.; Rosenman, I.; Veillet, P.; Cartier, C.; Villain, F. *Coord. Chem. Rev.* **1999**, *192*, 1023-1047.
- (196) Ohba, M.; Okawa, H. *Coord. Chem. Rev.* **2000**, *198*, 313-328.
- (197) Kahn, O.; Larionova, J.; Ouahab, L. *Chem. Commun.* **1999**, 945-952.
- (198) Koga, A.; Kawakami, N. *J. Phys. Soc. Jpn.* **2000**, *69*, 1834-1836.
- (199) Takushima, Y.; Koga, A.; Kawakami, N. *Phys. Rev. B* **2000**, *61*, 15189-15195.
- (200) Lehn, J. M. *Angew. Chem. Int. Edit.* **1990**, *29*, 1304-1319.
- (201) Olenyuk, B.; Whiteford, J. A.; Fechtenkotter, A.; Stang, P. J. *Nature* **1999**, *398*, 796-799.
- (202) Dinolfo, P. H.; Hupp, J. T. *Chem. Mat.* **2001**, *13*, 3113-3125.
- (203) Ziener, U.; Lehn, J. M.; Mourran, A.; Moller, M. *Chem. Eur. J.* **2002**, *8*, 951-957.
- (204) Semenov, A.; Spatz, J. P.; Moller, M.; Lehn, J. M.; Sell, B.; Schubert, D.; Weidl, C. H.; Schubert, U. S. *Angew. Chem. Int. Edit.* **1999**, *38*, 2547-2550.
- (205) Culp, J. T.; Park, J. H.; Stratakis, D.; Meisel, M. W.; Talham, D. R. *J. Am. Chem. Soc.* **2002**, *124*, 10083-10090.
- (206) Bertran, J. F.; Pascual, J. B.; Hernandez, M.; Rodriguez, R. *Reactivity of Solids* **1988**, *5*, 95-100.
- (207) Sato, O.; Einaga, Y.; Fujishima, A.; Hashimoto, K. *Inorg. Chem.* **1999**, *38*, 4405-4412.
- (208) Carlin, R. L. *Magnetochemistry*; Springer: Berlin, 1986.
- (209) Buser, H. J.; Schwarzenbach, D.; Petter, W.; Ludi, A. *Inorg. Chem.* **1977**, *16*, 2704-2710.
- (210) Kou, H. Z.; Bu, W. M.; Gao, S.; Liao, D. Z.; Jiang, Z. H.; Yan, S. P.; Fan, Y. G.; Wang, G. L. *J. Chem. Soc. Dalton Trans.* **2000**, 2996-3000.
- (211) Kou, H. Z.; Gao, S.; Bai, O.; Wang, Z. M. *Inorg. Chem.* **2001**, *40*, 6287-6294.
- (212) Kou, H. Z.; Gao, S.; Ma, B. Q.; Liao, D. Z. *Chem. Commun.* **2000**, 1309-1310.
- (213) Marvilliers, A.; Parsons, S.; Riviere, E.; Audiere, J. P.; Kurmoo, M.; Mallah, T. *Eur. J. Inorg. Chem.* **2001**, 1287-1293.
- (214) Re, N.; Crescenzi, R.; Floriani, C.; Miyasaka, H.; Matsumoto, N. *Inorg. Chem.* **1998**, *37*, 2717-2722.
- (215) Dujardin, E.; Ferlay, S.; Phan, X.; Desplanches, C.; Moulin, C. C. D.; Saintcavit, P.; Baudelet, F.; Dartyge, E.; Veillet, P.; Verdaguer, M. *J. Am. Chem. Soc.* **1998**, *120*, 11347-11352.
- (216) Buschmann, W. E.; Ensling, J.; Gutlich, P.; Miller, J. S. *Chem. Eur. J.* **1999**, *5*, 3019-3028.
- (217) Buschmann, W. E.; Miller, J. S. *Inorg. Chem.* **2000**, *39*, 2411-2421.
- (218) Mathieu, R.; Jonsson, P.; Nam, D. N. H.; Nordblad, P. *Phys. Rev. B* **2001**, *6309*, art. no.-092401.
- (219) Dormann, J. L.; Fiorani, D.; Tronc, E. *Adv. Chem. Phys.* **1997**, *98*, 283-494.
- (220) Mortimer, R. J. *Chem. Soc. Rev.* **1997**, *26*, 147-156.
- (221) Itaya, K.; Uchida, I.; Neff, V. D. *Acc. Chem. Res.* **1986**, *19*, 162-168.
- (222) Carpenter, M. K.; Conell, R. S. *J. Electrochem. Soc.* **1990**, *137*, 2464-2467.
- (223) Duek, E. A. R.; Depaoli, M. A.; Mastragostino, M. *Adv. Mater.* **1992**, *4*, 287-291.
- (224) Pyrasch, M.; Tieke, B. *Langmuir* **2001**, *17*, 7706-7709.

- (225) Xu, J. J.; Fang, H. Q.; Chen, H. Y. *J. Electroanal. Chem.* **1997**, *426*, 139-143.
- (226) Bharathi, S.; Yegnaraman, V.; Rao, G. P. *Langmuir* **1995**, *11*, 666-668.
- (227) Itaya, K.; Ataka, T.; Toshima, S. *J. Am. Chem. Soc.* **1982**, *104*, 4767-4772.
- (228) Ferlay, S.; Mallah, T.; Ouahes, R.; Veillet, P.; Verdaguer, M. *Inorg. Chem.* **1999**, *38*, 229-234.
- (229) Champion, G.; Escax, V.; Moulin, C. C. D.; Bleuzen, A.; Villain, F. O.; Baudelet, F.; Dartyge, E.; Verdaguer, N. *J. Am. Chem. Soc.* **2001**, *123*, 12544-12546.
- (230) Escax, V.; Bleuzen, A.; Moulin, C. C. D.; Villain, F.; Goujon, A.; Varret, F.; Verdaguer, M. *J. Am. Chem. Soc.* **2001**, *123*, 12536-12543.
- (231) Shimamoto, N.; Ohkoshi, S.; Sato, O.; Hashimoto, K. *Inorg. Chem.* **2002**, *41*, 678-684.
- (232) Guo, Y. Z.; Guadalupe, A. R.; Resto, O.; Fonseca, L. F.; Weisz, S. Z. *Chem. Mat.* **1999**, *11*, 135-140.
- (233) Lafuente, C.; Mingotaud, C.; Delhaes, P. *Chem. Phys. Lett.* **1999**, *302*, 523-527.
- (234) Buschmann, W. E.; Paulson, S. C.; Wynn, C. M.; Girtu, M. A.; Epstein, A. J.; White, H. S.; Miller, J. S. *Chem. Mat.* **1998**, *10*, 1386-1395.
- (235) Neff, V. D. *J. Electrochem. Soc.* **1978**, *125*, 886-887.
- (236) Lundgren, C. A.; Murray, R. W. *Inorg. Chem.* **1988**, *27*, 933-939.
- (237) Kulesza, P. J.; Doblhofer, K. *J. Electroanal. Chem.* **1989**, *274*, 95-105.
- (238) Kulesza, P. J.; Malik, M. A.; Miecznikowski, K.; Wolkiewicz, A.; Zamponi, S.; Berrettoni, M.; Marassi, R. *J. Electrochem. Soc.* **1996**, *143*, L10-L12.
- (239) Gao, Z. Q. *J. Electroanal. Chem.* **1994**, *370*, 95-102.
- (240) Herren, F.; Fischer, P.; Ludi, A.; Halg, W. *Inorg. Chem.* **1980**, *19*, 956-959.
- (241) Abrahams, B. F.; Hoskins, B. F.; Lam, Y. H.; Robson, R.; Separovic, F.; Woodberry, P. J. *Solid State Chem.* **2001**, *156*, 51-56.
- (242) Kim, J.; Whang, D.; Lee, J. I.; Kim, K. *Chem. Commun.* **1993**, 1400-1402.
- (243) Kitazawa, T.; Kikuyama, T.; Ugajin, H.; Takahashi, M.; Takeda, M. *J. Coord. Chem.* **1996**, *37*, 17-22.
- (244) Kitazawa, T.; Gomi, Y.; Takahashi, M.; Takeda, M.; Enomoto, M.; Miyazaki, A.; Enoki, T. *J. Mater. Chem.* **1996**, *6*, 119-121.
- (245) Ham, W. K.; Weakley, T. J. R.; Page, C. J. *J. Solid State Chem.* **1993**, *107*, 101-107.
- (246) Rayner, J. H.; Powell, H. M. *J. Chem. Soc.* **1952**, 319-328.
- (247) Woodward, J. D.; Backov, R.; Abboud, K. A.; Talham, D. R. *Acta Crystallogr. Sect. C* **2001**, *57*, 1027-1029.
- (248) Kou, H. Z.; Si, S. F.; Gao, S.; Liao, D. Z.; Jiang, Z. H.; Yan, S. P.; Fan, Y. G.; Wang, G. L. *Eur. J. Inorg. Chem.* **2002**, 699-702.
- (249) Constable, E. C.; Lewis, J.; Liptrot, M. C.; Raithby, P. R. *Inorg. Chim. Acta* **1990**, *178*, 47-54.
- (250) Bowmaker, G. A.; Kennedy, B. J.; Reid, J. C. *Inorg. Chem.* **1998**, *37*, 3968-3974.

BIOGRAPHICAL SKETCH

Jeffrey Thomas Culp graduated in 1988 from Rocky Grove High School, Franklin, PA. After graduation, he enlisted in the Navy as an aviation electronics technician. Jeff served four years with tactical electronics warfare squadron VAQ 140 stationed at NAS Whidbey Island, WA. His squadron deployed aboard the aircraft carrier USS Eisenhower where he worked as a flight deck avionics troubleshooter. His naval service took him many places including the Caribbean Sea, the Arctic Ocean, the Mediterranean Sea, the Suez Canal, the Red Sea, the Persian Gulf, and numerous countries along the way. His squadron was one of many called to duty during the Gulf War's Operation Desert Shield and Operation Desert Storm. Jeff was promoted to Petty Officer Second Class shortly before his honorable discharge in the summer of 1992.

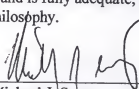
Jeff started his undergraduate studies at Clarion University of Pennsylvania in the spring of 1993 as a chemistry major. He was awarded the CRC Freshman Chemistry Achievement Award after his freshman year. After graduation with a bachelor's degree in 1997, Jeff entered graduate school at the University of Florida where he was awarded a Grinter Fellowship as an entering graduate student. He conducted research in thin film materials under the guidance of Professor Daniel R. Talham and received his Ph.D. in chemistry in the fall of 2002. He has presented his research at national meetings and has published many of his results in peer-reviewed journals.

I certify that I have read this study and that in my opinion it conforms to acceptable standards of scholarly presentation and is fully adequate, in scope and quality, as a dissertation for the degree of Doctor of Philosophy.



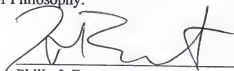
Daniel R. Talham, Chair
Professor of Chemistry

I certify that I have read this study and that in my opinion it conforms to acceptable standards of scholarly presentation and is fully adequate, in scope and quality, as a dissertation for the degree of Doctor of Philosophy.



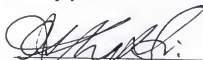
Michael J. Scott
Associate Professor of Chemistry

I certify that I have read this study and that in my opinion it conforms to acceptable standards of scholarly presentation and is fully adequate, in scope and quality, as a dissertation for the degree of Doctor of Philosophy.



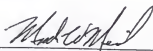
Philip J. Brucat
Associate Professor of Chemistry

I certify that I have read this study and that in my opinion it conforms to acceptable standards of scholarly presentation and is fully adequate, in scope and quality, as a dissertation for the degree of Doctor of Philosophy.



Khalil A. Abboud
Scientist of Chemistry

I certify that I have read this study and that in my opinion it conforms to acceptable standards of scholarly presentation and is fully adequate, in scope and quality, as a dissertation for the degree of Doctor of Philosophy.



Mark W. Meisel
Professor of Physics

LD

1780

20 02

,C968

UNIVERSITY OF FLORIDA



3 1262 08555 3443